Design of
Signal Integrity Enhancement Circuits

A Dissertation
Presented to
The Academic Faculty

by

Kil-Hoon Lee

In Partial Fulfillment
of the Requirements for the Degree
Doctor of Philosophy in the
School of Electrical and Computer Engineering

Georgia Institute of Technology
December 2010

Design of
Signal Integrity Enhancement Circuits

Approved by:

Dr. Emmanouil M. Tentzeris, Advisor
School of Electrical and Computer Engineering
Georgia Institute of Technology

Dr. Shyh-Chiang Shen
School of Electrical and Computer Engineering
Georgia Institute of Technology

Dr. Jongman Kim
School of Electrical and Computer Engineering
Georgia Institute of Technology

Dr. Chang-Ho Lee
School of Electrical and Computer Engineering
Georgia Institute of Technology

Dr. Jeonghu Han
Samsung Electro-Mechanics America, Inc.

Date Approved: November 9, 2010

To my family

ACKNOWLEDGEMENTS

I would like to first thank Professor Emmanouil M. Tentzeris for serving as my advisor. His support and encouragement during my difficult times will always be remembered and appreciated. I would like to also thank all of my Ph. D defense committee members, Professor Shyh-Chiang Shen, Professor Jongman Kim, Professor Chang-Ho Lee, and Dr. Jeonghu Han, for their time and valuable feedback.

I also would like to acknowledge all the members of the Microwave Applications Group. First of all, I express my gratitude to our boss, Professor Joy Laskar, for his mentorship, encouragement, and guidance in many aspects of my life over the past four years. I will always be grateful to him for providing me with the opportunity to work in his group. Next, I would like to thank Dr. Edward Gebara for his guidance, support, and patience as our team leader. This work has also benefited from invaluable discussions with Dr. Kyutae Lim, Dr. Franklin Bien, Dr. Hyoung-Soo Kim, Dr. Tae-Joong Song, Hyungwook Kim, Sanghyun Woo, and Debesh Bhatta. In addition, all the members of the Samsung Design Center and past and present MAG members deserve special thanks. I would like to acknowledge Mrs. Angelika Gebara as well for her support as a MAG administrative staff.

My deepest gratitude is reserved for my parents who gave me the opportunity and encouragement to achieve my educational goals. Lastly, I would like to thank my wife, Jihyang Kim; there are no words that can describe the amount of support, patience, and love that she has given me during the four years of my study.

TABLE OF CONTENTS

LIST OF TABLES

LIST OF FIGURES

LIST OF SYMBOLS AND ABBREVIATIONS

BER	Bit-Error-Rate
CD	Chromatic Dispersion
CMOS	Complementary Metal-Oxide Semiconductor
CW	Continuous Wave
DC	Direct Current
DCF	Dispersion Compensating Fiber
DCR	Direct Conversion Receiver
DFE	Decision-Feedback Equalizer
DMD	Differential Modal Delay
DPCH	Dedicated Physical Channel
DPSK	Differential Phase-Shift Keying
DWDM	Dense-Wavelength-Division-Multiplexing
EDC	Electronic Dispersion Compensator
FDD	Frequency-Division Duplexing
FFE	Feed-Forward Equalizer
FIR	Finite Impulse Response
HPF	High-Pass Filter
IC	Integrated Circuit
IDT	Inter-Digitized Transducer
IMD2	Second-Order Inter-Modulation Distortion
ISI	Inter-Symbol Interference
IQ	In-phase and Quadrature-phase
LAN	Local Area Network
LMS	Least-Mean Square
LNA	Low-Noise Amplifier

LO	Local Oscillator
MAN	Metropolitan Area Network
MDS	Minimum Detectable Signal
MLSE	Maximum-Likelihood-Sequence Estimation
MMF	Multi-Mode Fiber
MMSE	Minimum Mean-Square Error
MZ	Mach-Zehnder
NF	Noise Figure
NRZ	Non-Return to Zero
OSNR	Optical Signal-to-Noise Ratio
PA	Power Amplifier
PCB	Printed Circuit Board
PMD	Polarization-Mode Dispersion
PPF	Poly-Phase Filter
PRBS	Pseudo-Random Bit Sequence
PSTN	Public Switch Telephone Network
PVT	Process, Voltage, Temperature
RF	Radio Frequency
RX	Receiver
SAW	Surface Acoustic Wave
SMD	Surface Mount Device
SMF	Single-Mode Fiber
SNR	Signal-to-Noise Ratio
TDD	Time-Division Duplexing
TX	Transmitter

TXLC	Transmitter Leakage Canceller
VGA	Variable Gain Amplifier
VNA	Vector Network Analyzer
WCDMA	Wideband Code Division Multiple Access
WLAN	Wireless Local Area Network
XMD	Cross-Modulation Distortion
ZF	Zero-Forcing

SUMMARY

Today's network infrastructures rely on the interconnection and interoperation of both wired and wireless communication systems. Moreover, for an accurate processing of the signal and extraction of information, it is important that signal integrity is maintained at a level where the receiver-end can detect the desired signal amidst the surrounding noise. Therefore, this dissertation is aimed at examining signal integrity degradation factors and realizing signal integrity enhancement circuits for both wired and wireless communication systems.

For wired communication systems, an optical coherent system employing an electrical equalization circuit is studied as a way of extending the transmission distance limited by optical fiber dispersion mechanisms. System simulation of the optical coherent receiver combined with the feed-forward equalizers is performed to determine the design specification of the equalizer circuit. The equalization circuit is designed and implemented in a 0.18 μm complementary metal-oxide semiconductor (CMOS) process and demonstrates the capability to extend the transmission reach of long-haul optical systems over single-mode fiber to 600 km.

Additionally, for wireless applications, signal integrity issues found in a full-duplex wireless communication network are examined. Full-duplex wireless systems are subject to interference from their own transmitter leakage signals; thus, a transmitter leakage cancellation circuit is designed and implemented in a 0.18 μm CMOS technology. The proposed cancellation circuit is integrated with a low-noise amplifier and demonstrates over 20 dB of transmitter leakage signal suppression.

CHAPTER

1

Introduction

1.1 Modern Communication Systems

Communication is an essential human need and a fundamental social necessity; this demand, along with an advancement of solid-state electronics, has fueled the explosive growth of various communication systems over the past several decades. As illustrated in Figure 1.1, today's typical network structures consist of both wired and wireless communication systems that are interconnected together. For applications demanding high data rate and long delivery, optical fibers are widely employed due to their high-bandwidth and low-loss characteristics. Long-haul and metro-core networks, which extend beyond 80-km for data transmission in giga-bit-per-second (Gbps) and tera-bit-per-second (Tbps) regimes, both use optical fibers as their transmission medium. On the

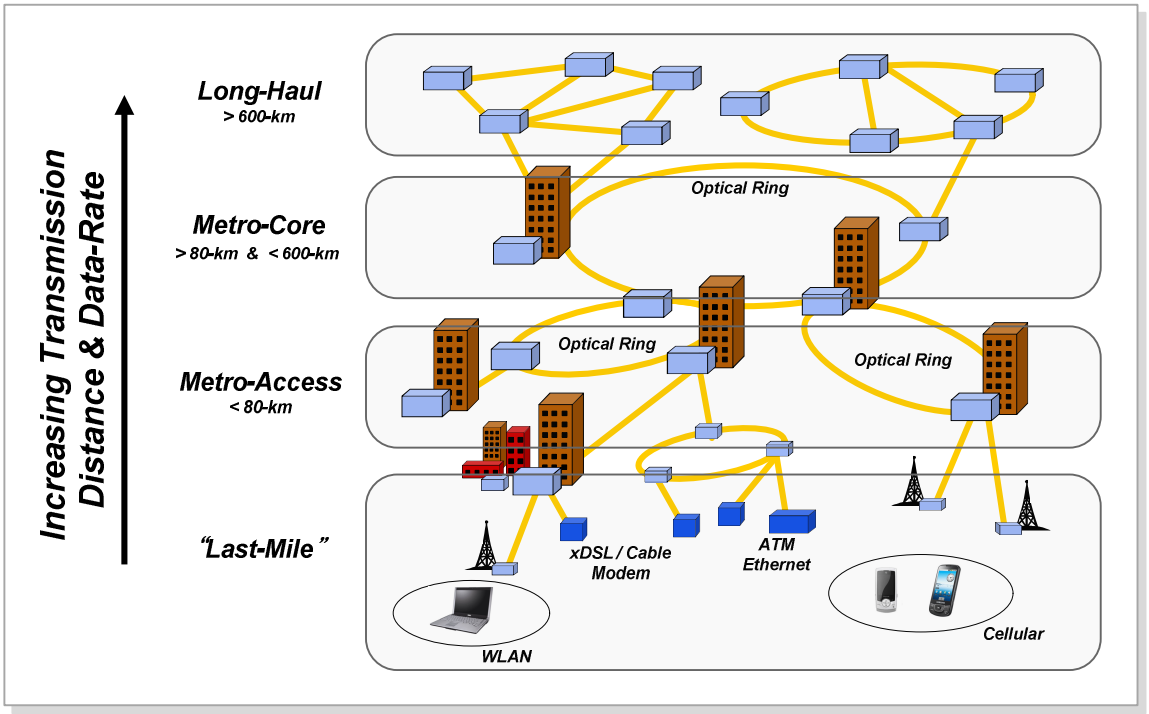

Figure 1.1. Hierarchical diagram of today's typical network system.

other hand, for more moderate data rate and shorter reach applications, wireless communication devices, such as cellular phones and wireless local-area networks (WLANs), have gained tremendous popularity over the past decades as they can ultimately provide mobility to end-users. These mobile communicating devices connect wirelessly to a base station that links to a public switched telephone network (PSTN) via optical fiber to be capable of delivering significant amount of data at rapid speed. This brief description of the connection between mobile phones and PSTN is just one example that illustrates how modern network systems rely on the interconnection and interoperation of both wired and wireless communication systems.

1.2 Signal Integrity in Communication Systems

Preserving signal integrity is an important requirement in communication systems whose essence is to transmit and receive an information-carrying signal over a medium such as copper, optical fiber, or free space. For an accurate processing of the signal and extraction of information at the receiver-end, it is important that signal integrity, or signal quality, is maintained at a level where the receiver can detect the desired signal amidst the surrounding noise. As illustrated in Figure 1.2, degradation of signal integrity, however, is inevitable as the signal travels through the medium at high data rates and over long distances; and the factors that contribute to this degradation are different for various types of transmission channel used.

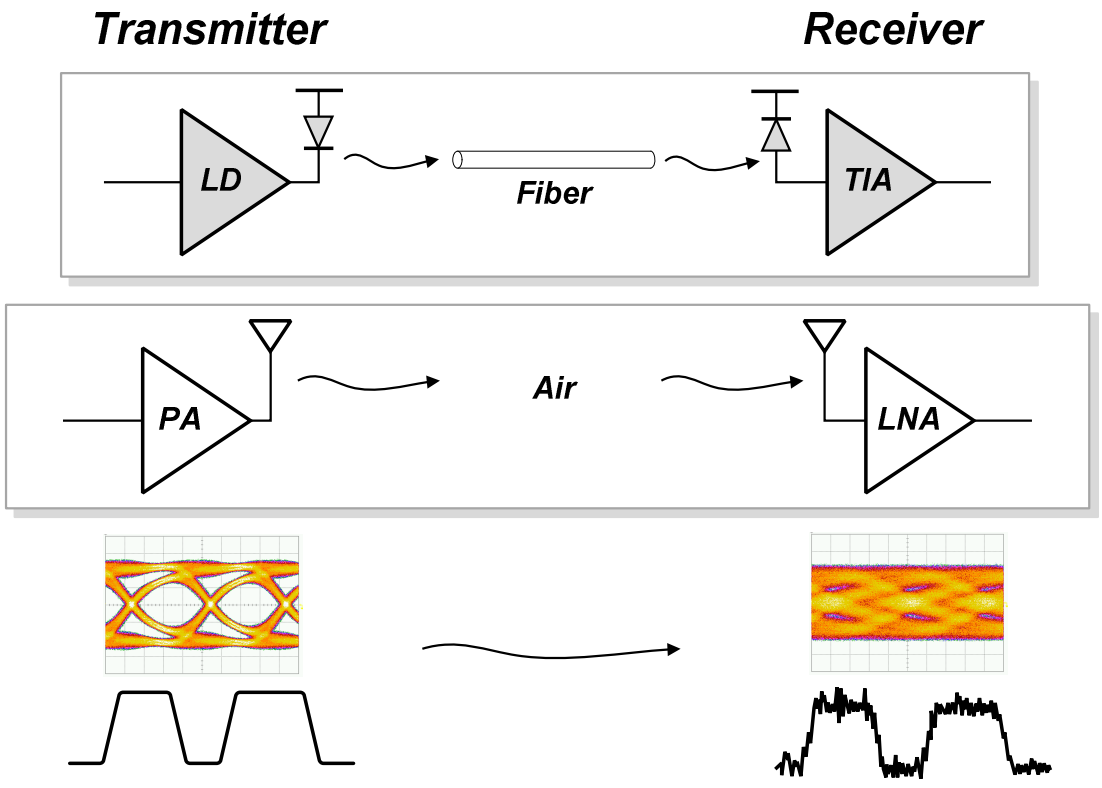

Figure 1.2. Degradation of signal integrity in communication systems.

In wired communications employing optical fiber as the transmission medium, signal integrity experiences significant degradation as the transmission speed increases to the multi-Gbps regime. The major contributing factor in signal integrity degradation is the dispersion mechanisms occurring in optical fibers with the increasing speed and distance. Dispersion in fibers causes broadening of the signal pulses traveling through the fiber; a phenomenon which can directly degrade the performance of the optical receiver systems.

In today's heavily-crowded wireless environment, the importance of maintaining high level of signal integrity is greater than ever before; and only the radio devices with high receiver sensitivity can perform well. Signal integrity can be threatened by the mutual interference from the coexistence of different wireless devices in the same or neighboring frequency spectrum. Furthermore, there can be self-interference within the wireless transceivers (i.e. signal leakage from the transmitter to the receiver) that can lead to various performance-degrading distortion mechanisms.

1.3 Organization of the Dissertation

The previous sections of this chapter briefly described how today's typical network structures rely on the interconnection and interoperation of both wired and wireless communication systems. Moreover, the importance of maintaining signal integrity and various factors that lead to signal integrity degradation in both optical and wireless systems are introduced as well.

In Chapter 2, a brief historical background and evolution of optical communication systems are highlighted. Different types of fiber dispersion mechanisms and their

degrading effects on the optical system are described in detail. Then, various technical solutions to compensate for fiber dispersion are introduced. These methods include use of all-optical techniques, dispersion-tolerant modulation schemes, and electronic dispersion compensators.

Chapter 3 details an optical coherent detection system employing feed-forward equalizers (FFEs) to compensate for fiber dispersion in long-haul optical networks. The proposed optical system employs optical duobinary encoding in the transmitter and FFEs in the receiver. System simulation of the optical receiver combined with the FFEs is performed to determine the design specification (e.g., number of taps, tap-spacing, bandwidth) of the FFE and to demonstrate the improved performance of the overall optical link. The required FFE is designed and implemented in a 0.18-μm complementary metal-oxide semiconductor (CMOS) technology, and detailed description of the different building blocks of the FFE is presented. Lastly, the measurement results of the FFE and the overall system performance are presented.

After addressing the signal integrity issues in optical communications in the previous chapters, Chapter 4 examines the signal integrity problems found in the RF wireless systems. To be more specific, the chapter concentrates on a full-duplex wireless system which is widely employed in today's wireless environment. Full-duplex systems suffer interference from their own transmitter leakage signal, and this impairment degrades the receiver sensitivity and needs to be compensated for. Two transmitter leakage signal induced distortion mechanisms which include second-order intermodulation distortion and cross-modulation distortion are described in more details.

Chapter 5 then proposes a transmitter leakage canceller circuit that is simple in implementation and has low noise figure contribution. The proposed leakage canceller is a feed-forward canceller which samples a reference signal from the transmitter output and injects the amplitude-adjusted and phase-rotated signal to the receiver chain. The canceller circuit is integrated with a low-noise amplifier and implemented in a 0.18-μm CMOS technology. Moreover, the measurement results of the circuit's leakage cancellation performance are presented at the end of this chapter. Lastly, Chapter 6 concludes with summary and remaining future work of this research.

CHAPTER

2

Signal Integrity in Optical Systems

2.1 Optical Communication Systems

In wired communication systems, data is transferred over a physical medium of linkage such as a copper wire or an optical fiber; and especially in the last few decades, there has been a widespread usage of an optical fiber as a transport medium for high-speed data. This rapid-growing deployment of optical networks stemmed from the two desirable characteristics of fibers: large bandwidth and low loss. A bandwidth in the terahertz regime is obtained with the fiber because the frequency of light is many orders of magnitude higher than that of the electrical signals. The optical fiber's increased bandwidth provides higher data capacity, making it an ideal medium for today's high-speed data transmission system. Moreover, the advancement of dense wavelength

division multiplexing (DWDM) technology, which allows transmission of multiple optical signals over a single fiber using different light wavelengths, has also contributed to the explosive growth of optical communications by further increasing the capacity of optical networks [1].

The low loss of fibers also led to the wide deployment of optical communication for the transport of high-speed data. Since the demonstration of silica fibers having a loss of less than 20-dB/km in 1970, the advancement in semiconductor industry has led to the significant reduction in impurities and variation in the uniformity of fibers; thus, the loss of fibers improved to 4-dB/km in 1975 and 0.2-dB/km in 1990. As shown in Figure 2.1,

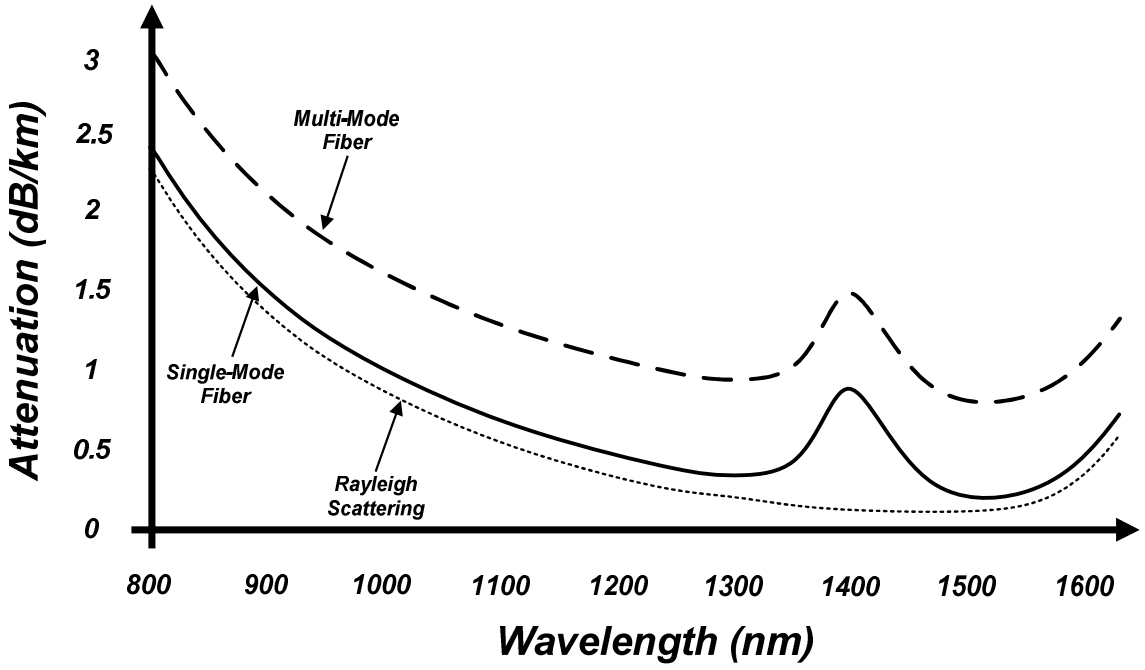

Figure 2.1. Typical fiber attenuation across the light wavelength.

the fiber attenuation varies considerably with the light wavelength. The early optical systems operated in the band around 800 to 900-nm. In the mid 1980s, the development of lasers and photo-detectors operating around 1300-nm band enabled a shift to this wavelength which has an attenuation of only about 0.4-dB/km. In the late 1990s, the widespread operation in the band between 1510-nm and 1600-nm started because the fiber attenuation is lowest (around 0.26-dB/km) in this band.

Various data transmission standards have been developed for different optical applications over the past years. To meet the increasing demands for today's bandwidth-extensive multimedia content delivery, these standards are being upgraded to higher data throughput as shown in Figure 2.2. As an example, the data rate in the IEEE 802.3 standard for wired Ethernet started from 10-Mbps and has been constantly increased to

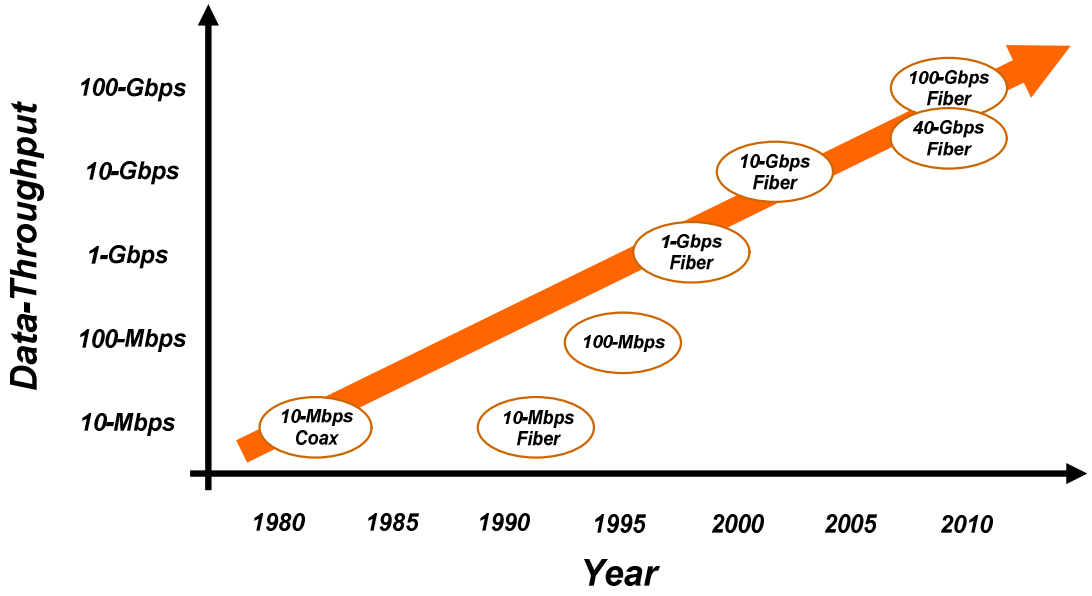

Figure 2.2. Growth in data throughput of the IEEE 802.3 standard.

100-Mbps (IEEE 802.3u in 1995), 1-Gbps (IEEE 802.3z in 1998), and 10-Gbps (IEEE 802.3ae in 2003). In 2010, the IEEE 802.3ba supporting data rates greater than 10-Gbps has been approved: the 40-Gbps throughput for local server applications and the 100-Gbps throughput for the Internet backbone [2].

As the transmission speed increases to the multi-Gbps range, optical fibers begin to display limitations because much of the installed infrastructure in optical transmission systems was initially aimed at handling much slower throughputs in the Mbps regime. Therefore, the installed fibers experience significant signal integrity degradation that is induced by optical dispersion mechanisms. Dispersion in fibers leads to broadening of signal pulses and results in inter-symbol interference (ISI), a phenomenon in which the spreading of successive signal pulses smears the pulses into one another, making the peaks of the pulses indistinguishable [1], as shown in Figure 2.3.

With the increasing data rate and transmission distance, the effect of ISI on signal integrity rises and thus closes the “eye” of the received signal as observed from both Figure 2.4 (a) and (b). These eye-diagrams are obtained by overlapping the time domain

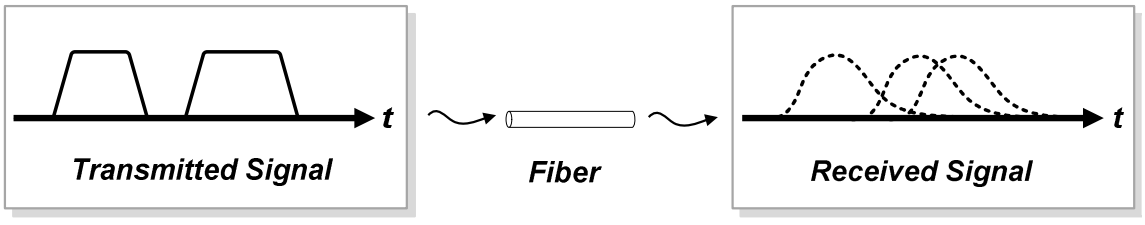

Figure 2.3. Pulse broadening due to fiber dispersion.

signal for a certain number of symbols in order to provide at-a-glance evaluation of system performance. When the impairments to the signal increase, the eye opening starts to decrease; thus, the completely closed eye diagrams in Figure 2.4 (a) and (b) indicate that significant degradation in signal integrity has occurred at 10-Gbps data rate and 300-m of transmission distance, respectively.

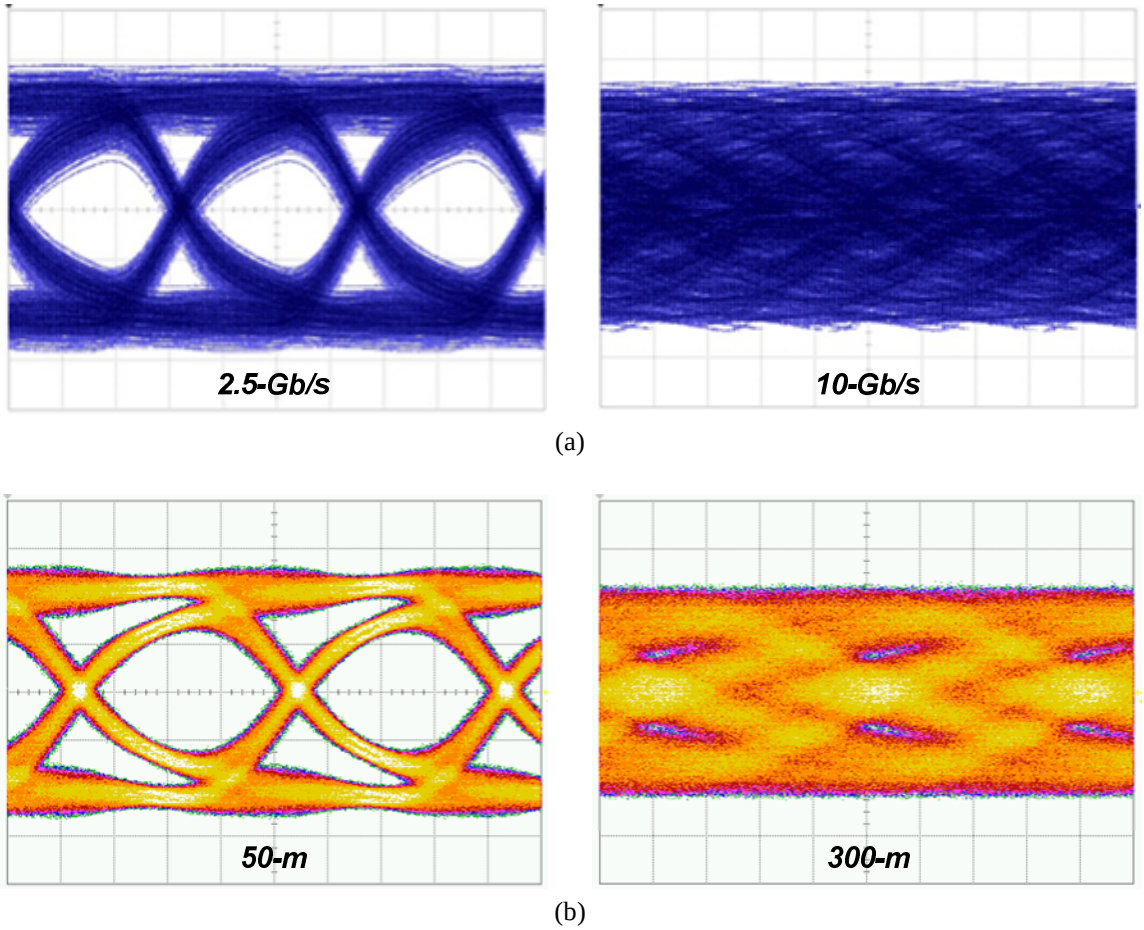

Figure 2.4. Effect of (a) increasing data rate and (b) channel length on ISI.

2.2 Optical Fibers and Dispersion Mechanisms

The two types of fiber that are widely employed in optical communication systems are multi-mode fiber (MMF) and single-mode fiber (SMF). MMF has a large core diameter, which causes light to travel down the fiber in different or multi-modes. Although the large core size allows the efficient collection of light from an inexpensive light source, the generation of multi-modes of light lay is an undesirable phenomenon in communication systems because the different modes travel at different speeds and arrive at the receiver at different times. Therefore, MMF is mainly used in short-reach applications that have modest data rates and require inexpensive connections. SMF, on the other hand, has a smaller core diameter than MMF and can allow light to be transmitted in a single mode. Because the single-mode transmission permits a faster and longer transfer of data, SMF is widely used in long-haul optical networks [3]. The two different transmission properties of light in SMF and MMF are illustrated in Figure .

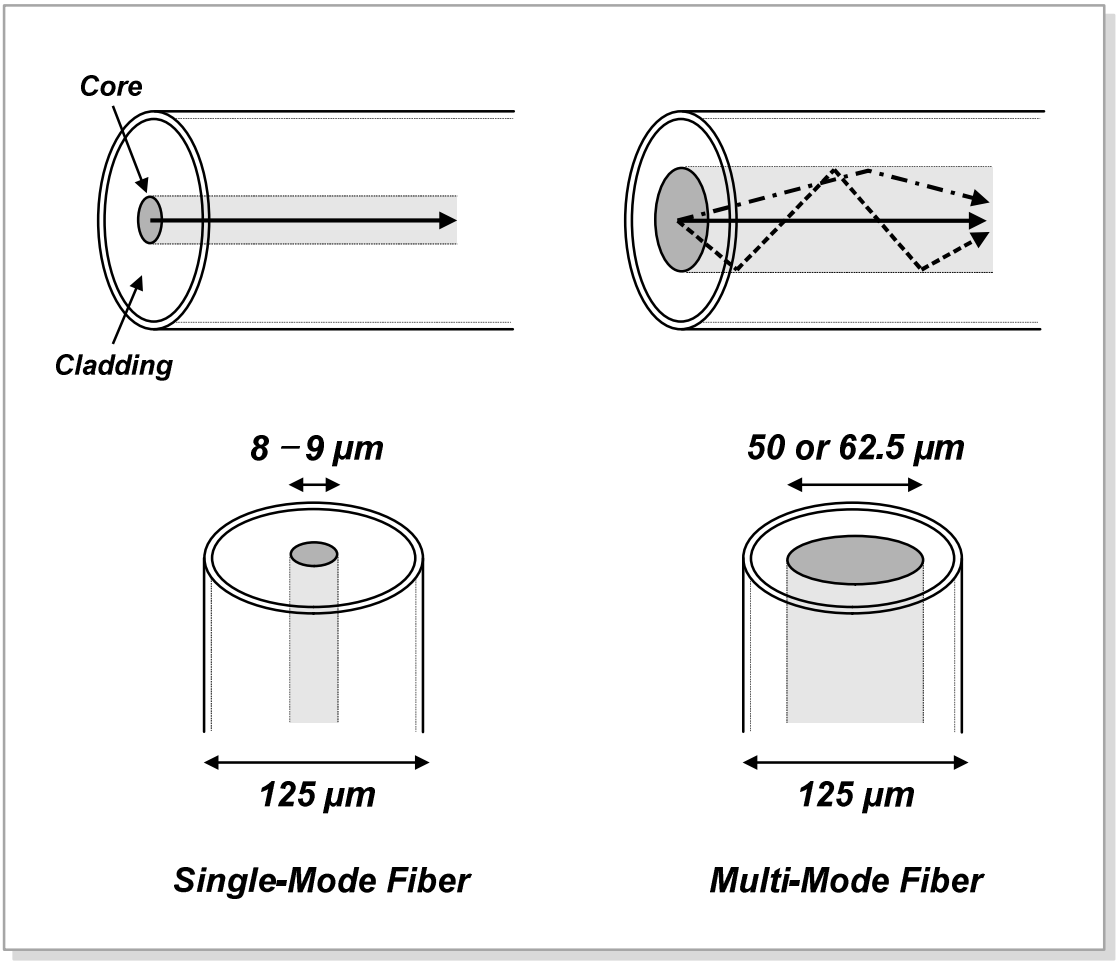

Figure 2.5. Transmission of light over SMF and MMF, and their physical dimensions.

There are three main types of dispersion in optical fibers, and these dispersion mechanisms vary depending on the type of fiber used. The first type of optical dispersion is differential modal delay (DMD), which is the main source of ISI in MMF. As previously mentioned, the different modes of light travel across the fiber in different paths. Lower-order modes travel down the center of the core and have the lowest transit time, whereas higher-order modes propagate near the cladding of the fiber, reaching the far end more slowly. This phenomenon is called DMD and is illustrated in Figure 2.6.

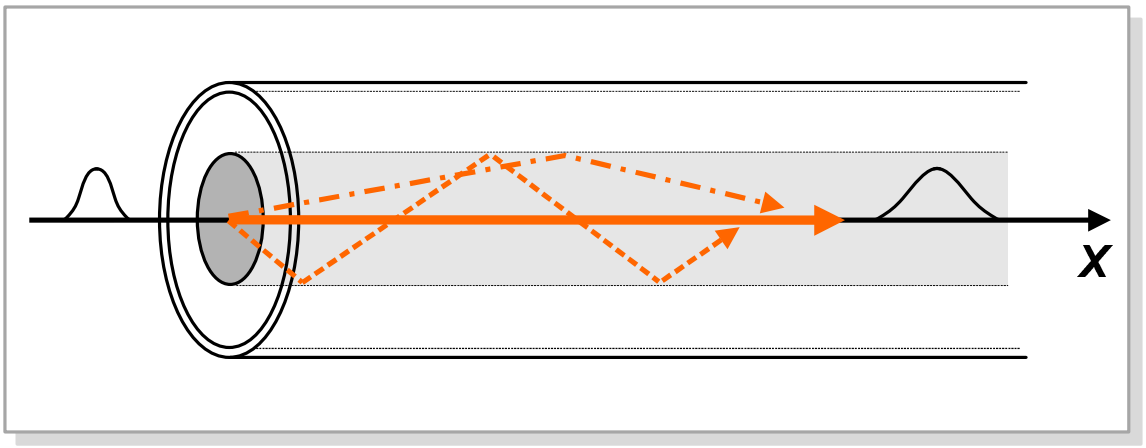

Figure 2.6. Differential modal delay.

Therefore, the usage of MMF is mainly limited to short reach applications, such as enterprise LANs that span less than 1-km at 100-Mbps data rate. A measure of pulse broadening due to DMD is the time delay between the two modes of light traveling the shortest and longest paths in MMF. This time delay can be estimated as

$$\Delta T_{DMD} = \frac{L}{c}\frac{n_1^2}{n_2}\Delta, \tag{2.1}$$

where L is the fiber length, c is the speed of light, n_1 is the core refractive index, n_2 is the cladding refractive index, and Δ is the fractional index change at the core-cladding interface which equals $(n_1 - n_2)/n_1$.

In SMF, DMD is eliminated because SMF only supports one transverse mode. Light traveling in SMF, however, still experiences different types of dispersion mechanisms, and they are polarization-mode dispersion (PMD) and chromatic dispersion (CD). PMD results from a variation in the refractive index experienced by the light traveling in the two polarization modes of SMF, and this phenomenon is called birefringence. The

difference in the refractive index is caused by the fiber cross-section's slight asymmetry (having an elliptical rather than a circular shape) that is inevitable during the manufacturing process of fibers. As shown in Figure 2.7, PMD causes the optical pulses

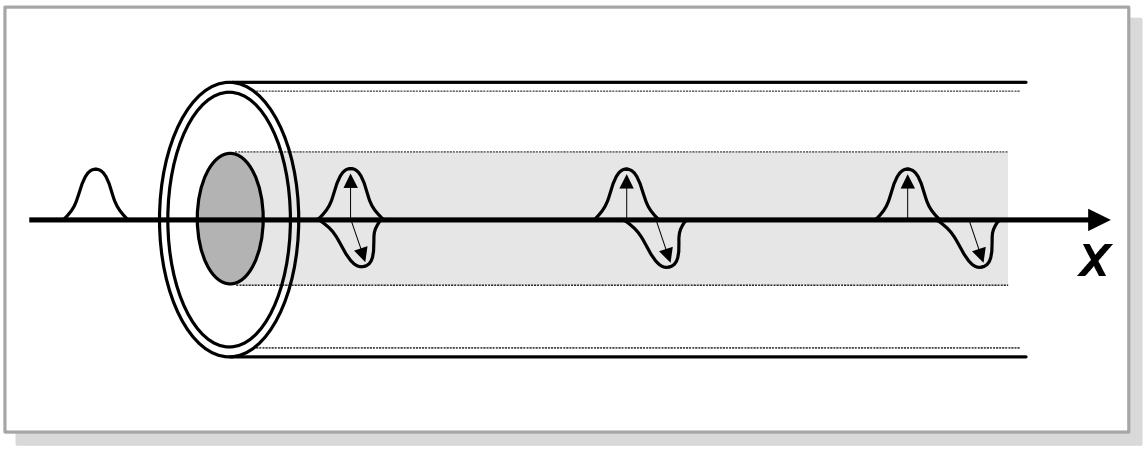

Figure 2.7. Polarization-mode dispersion.

in different polarization modes to travel across SMF at different speeds, resulting in ISI at the output. The delay between the fast and slow polarization modes, or the bifurcation time, is given by

$$\Delta T_{PMD} = L\left[\frac{\Delta n}{c} - \frac{\omega}{c}\cdot\frac{\delta(\Delta n)}{\delta\omega}\right], \tag{2.2}$$

where ω is the light frequency and $\Delta\underline{n}$ is the difference between propagation velocities of the slow and fast polarization modes.

Another type of dispersion mechanism in SMF, CD, is a dispersion mechanism caused by a variation in the propagation velocity of light with wavelength. Since all light

sources emit light in a band of certain spectral width (0.2-nm to 5-nm width), different wavelengths of the band do not reach the fiber output simultaneously, leading to pulse spreading. Figure 2.8 illustrates the effect of CD on different spectral components of an

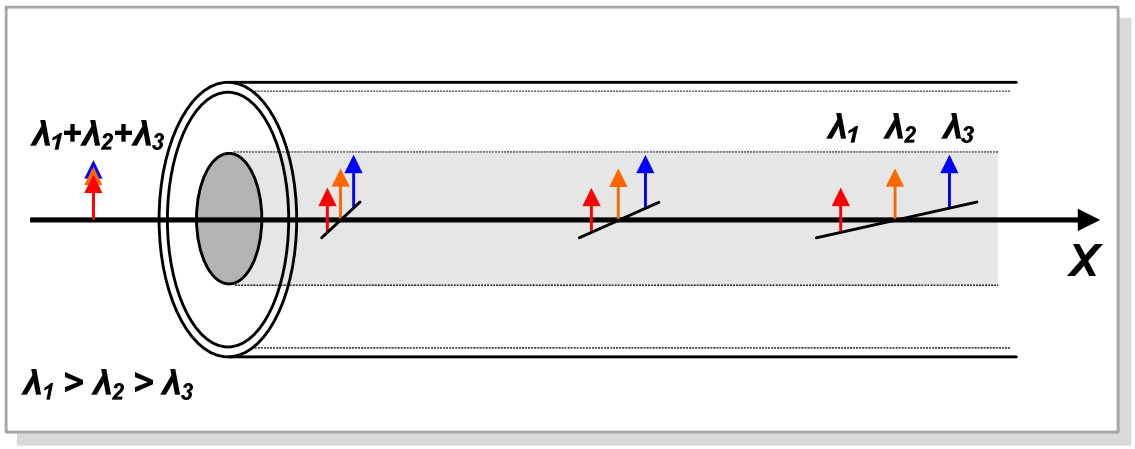

Figure 2.8. Chromatic dispersion.

optical pulse. The CD-induced pulse broadening can be estimated by

$$\Delta T_{CD} = DL\Delta\lambda, \tag{2.3}$$

where $\Delta\lambda$ is the range of wavelengths contained in the optical source and D is called the dispersion parameter that is expressed in units of ps/nm/km. The dispersion parameter describes the pulse spreading in picoseconds per kilometer of fiber for 1-nm of change in the wavelength. As shown in Figure 2.9, the chromatic dispersion parameter varies with the wavelength and equals zero around 1300-nm. Most of the modern optical networks, however, operate in the 1550-nm band because this band provides the lowest fiber

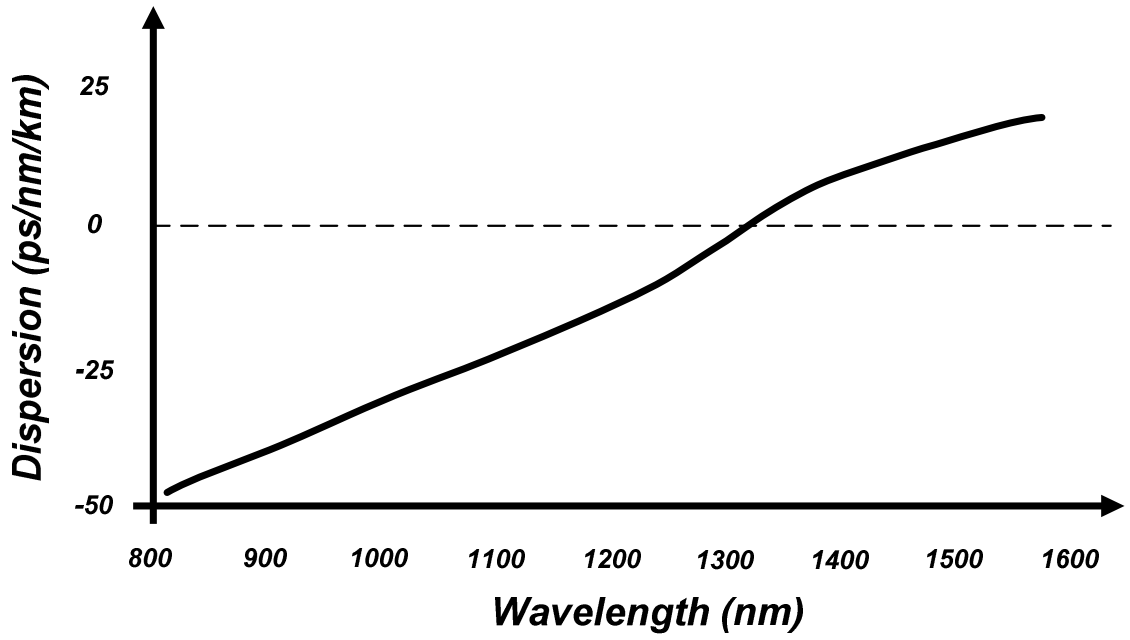

Figure 2.9. Chromatic dispersion parameter across wavelength.

attenuation and largest bandwidth for DWDM systems; and at 1550-nm, chromatic dispersion is quite large (around 17-ps/nm/km), and therefore, requires some kind of compensation.

2.3 Dispersion Compensation Techniques

The preceding section described how DMD, PMD, and CD can result in ISI and degrade the performance of optical communication systems that employ MMF and SMF as the transport medium. For data transmission in the multi-Gb/s range, these dispersion mechanisms significantly limit the reach of the networks. Newer and more advanced optical fibers have been developed that can support the higher throughput data

transmission. These fibers include dispersion shifted fibers and dispersion flattened fibers that have manipulated core profile such that a dispersion of only 4-ps/nm/km is obtained in the vicinity of 1550-nm [4]. However, the cost involved in replacing the existing fiber network with the novel kind is prohibitive. Thus, the network providers and operators prefer seamless and cost-effective transition that reuses the existing network infrastructures as much as possible. Some kinds of compensation methods for ISI, therefore, are required to maintain signal integrity over the installed transmission media and enable migration to higher data rates.

Various dispersion compensation techniques have been investigated and implemented up to now, and these techniques are divided into three main categories: all-optical techniques, advanced modulation formats, and electronic dispersion compensation methods. The first method is based on all-optical techniques, such as adding dispersion compensating fibers [4] or adaptively tuned birefringence [6] in SMF. Commercially available dispersion compensating fibers have the total dispersion over 100-ps/nm/km in the opposite direction to CD in standard SMFs; thus, when the dispersion compensating fibers are placed in series with the standard SMFs, CD-induced ISI can be compensated. Similar approach can be made to compensate for PMD by inserting adaptively tuned birefringence that is in the opposite direction to that of the existing link. Use of a multi-segment photo-detector [7] and offset launching to MMF to reduce the number of excited modes [8] were also studied as compensation methods for ISI in MMF. All of the aforementioned-techniques in the optical domain have good compensation performance but they are still very costly and bulky.

The second method is to employ dispersion-tolerant advanced modulation formats, such as an optical duobinary coding [9] or a differential phase-shift keying (DPSK) signal [10]. The optical duobinary modulation format results in two-level intensity modulated optical duobinary signals in which the "1" level can have a phase of either 0 or π. The π-phase flips occurring in the middle of each "0" level cause destructive interference with the finite energies left within the bit-period of "1" levels. This phenomenon in the duobinary coding confines the energy of "1" in its bit-slot as shown in Figure 2.10.

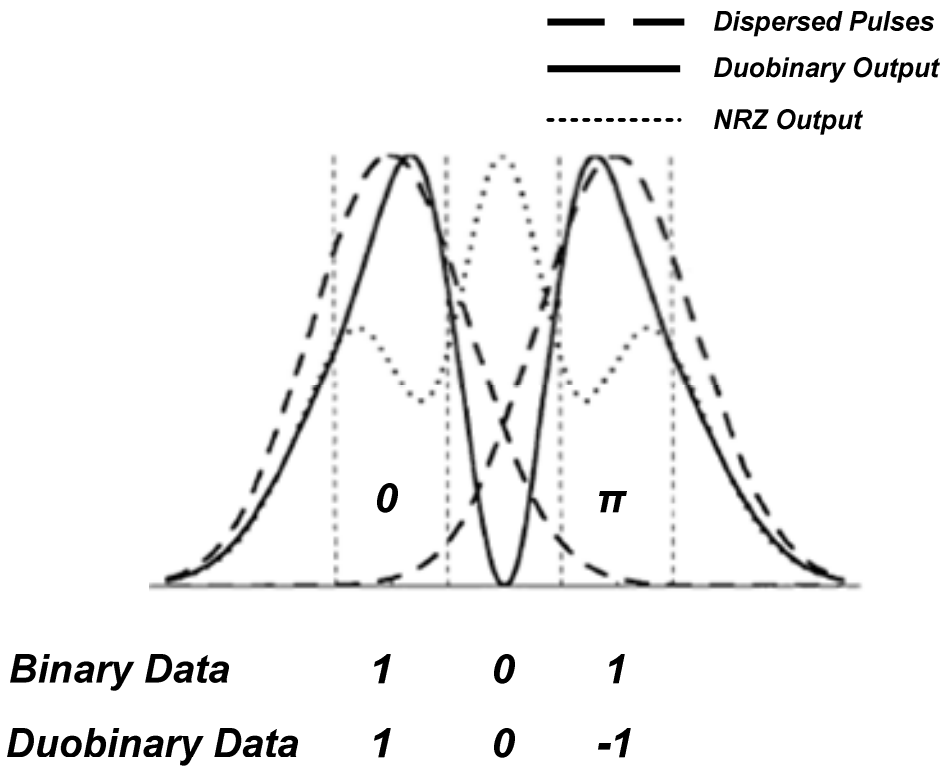

Figure 2.10. Destructive interference in 0-level of optical duobinary coding.

The third approach is to use electronic dispersion compensation (EDC) [11], which can provide a compact and cost-effective solution. EDC is performed using an equalizer, which is a circuit that can alter the frequency response characteristics of a system to compensate for channel-induced ISI. Equalization is conducted on the received signal after it has been converted from light to electricity by a photodiode in the receiver. Two of the most common equalization techniques employ FFE and decision-feedback equalizer (DFE).

A FFE is a linear equalizer based on a finite impulse response (FIR) filter whose block diagram is shown in Figure 2.11.

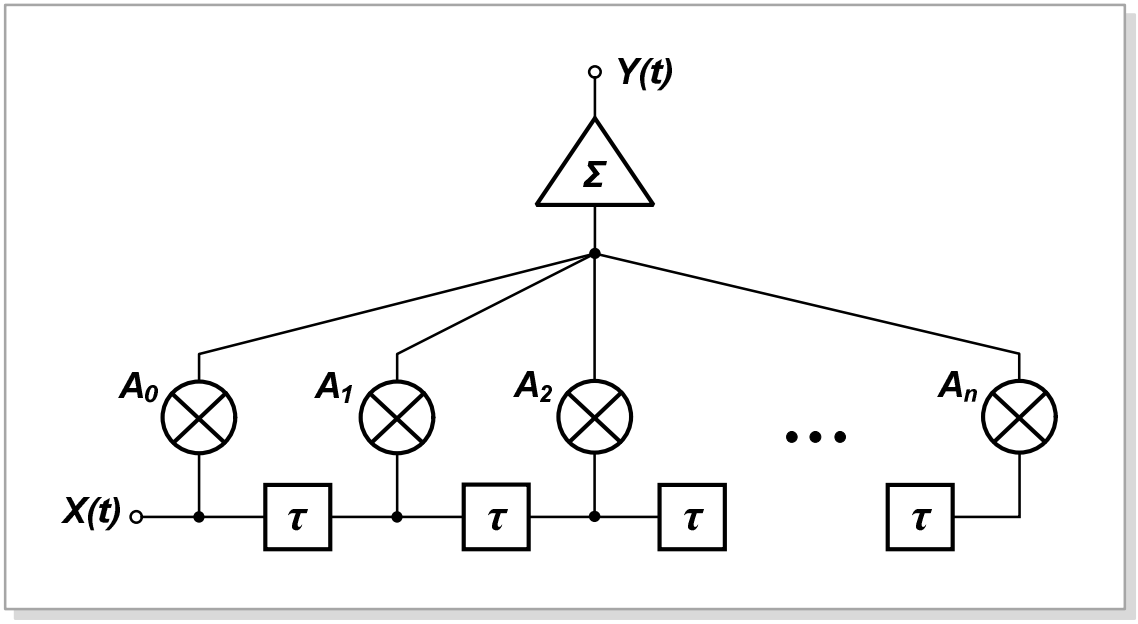

Figure 2.11. Block diagram of the FIR filter-based FFE.

The transfer function of the FIR filter-based FFE is expressed as

$$Y(t) = \sum_{i=0}^{n} A_i \cdot X(t - i\tau), \tag{2.4}$$

where n + 1 is the number of taps, τ is the delay between taps, and A_i is the adjustable tap coefficient. The FFE splits the input signal, $X(t)$, into (n + 1) branches using tapped delay lines and then combines the output as $Y(t)$ in (2.4).

A FFE attempts to compensate for fiber dispersion by exhibiting a transfer function that is an inverse of that of the channel as follows:

$$H_{EQ}(f) \equiv \frac{1}{C(f)} = \frac{1}{|C(f)|} e^{-j\theta_c(f)}. \tag{2.5}$$

In (2.5), $H_{EQ}(f)$ is a transfer function of the FFE, $C(f)$ is the channel response of fiber. This form of equalization is called zero-forcing (ZF) equalization, as it attempts to cancel all the ISI present in a symbol stream [12]. ZF equalization can also amplify the additive noise in the channel because of its inverse characteristics with respect to the channel. Thus, in a noisy channel where ZF equalization is not effective, an equalization using the minimum-mean-square-error (MMSE) algorithm can be employed. By adjusting the tap coefficients of the FFE based on the MMSE algorithm, both the ISI and additive noise power in the channel is minimized [12].

FFEs can be placed at two different locations in the optical networks: at the transmitter and at the receiver. The FFE implemented at the transmitter is called a pre-emphasis FFE. In such configuration, the FFE pre-distorts the transmitted data in a way that the data is free of ISI after it is received at the far end. The pre-emphasis FFE can only be employed for a channel whose response is known a-priori, and this type of FFE cannot perform an adaptive operation. A post-emphasis FFE, which is placed at the receiver, is capable of being adaptive, as it can monitor the output of the fiber and update the tap coefficients dynamically.

Decision-feedback equalization is another type of equalization technique that is commonly used to mitigate the dispersion-induced ISI in optical communication systems. In contrast to the FFE, the DFE is capable of compensating for non-linear channel impairments because the DFE employs a decision block to provide feedback from the output [13]. The DFE is typically employed in conjunction with the FFE as shown in Figure 2.12.

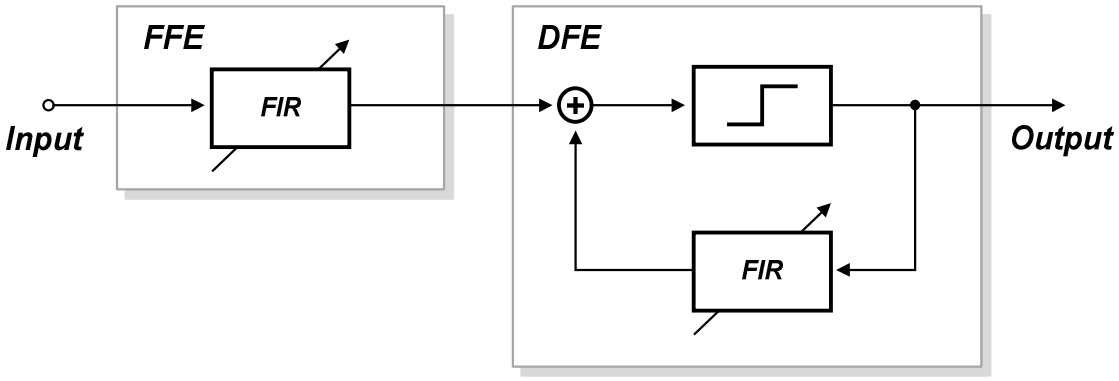

Figure 2.12. Block diagram of a conventional DFE.

CHAPTER

3

Optical Coherent Detection System with Feed-Forward Equalizers

3.1 System Description

An increase in multimedia content delivery demands a capacity upgrade in all parts of an optical network as the one shown in Figure 3.1. The target application of this work is the “metro-core” region which uses SMF as the transmission medium for data delivery from 80 to 600-km. In order to increase the throughput to 10-Gb/s in the metro-core area, the existing network requires either optical signal regeneration or dispersion compensation because the installed SMF can only deliver in the span of 80-km at such data rate [14]. Therefore, the optical coherent system utilizing FFEs is studied to extend the reach of the metro-core network up to 600-km for the 10-Gb/s data transmission. In particular, the optical system in this research aims at achieving compensation for CD in

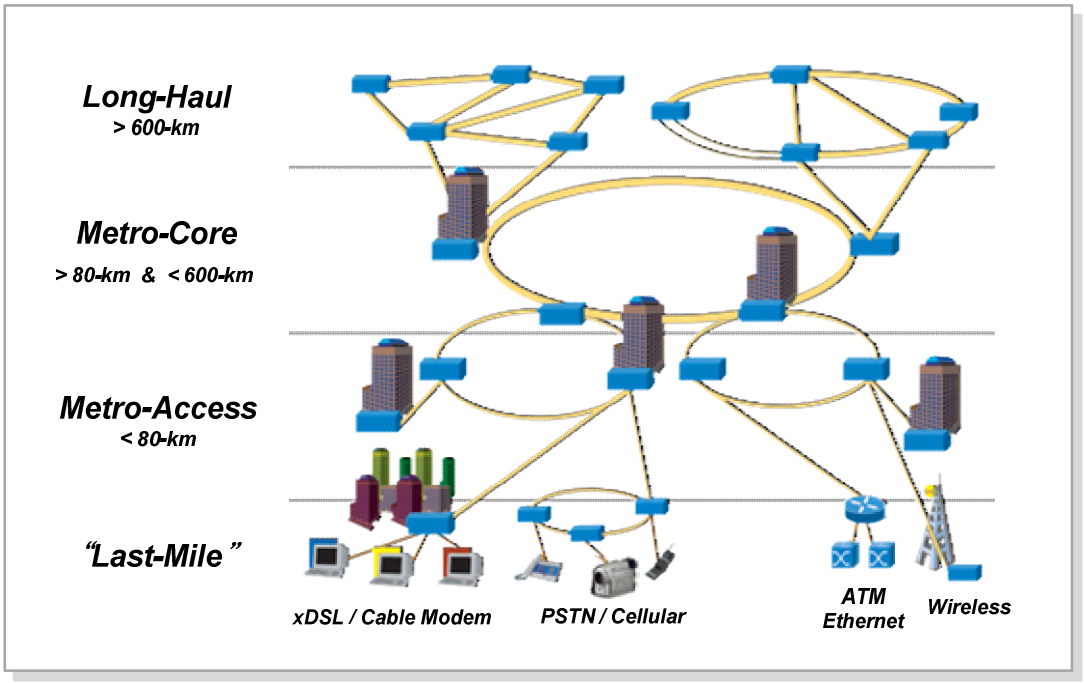

Figure 3.1. Hierarchical architecture of typical optical network.

the SMF because the effect of CD is more severe than that of PMD in such link extending from 80 to 600-km.

3.1.1 Optical Duobinary Transmitter

The transmitter of the optical system uses a dispersion-tolerant optical duobinary coding. In the optical duobinary modulation format, the pre-coded 10-Gb/s nonreturn-to-zero (NRZ) binary signals are filtered by a 5^{th}-order Bessel filter having a cut-off frequency of 2.8-GHz to generate three-level duobinary signals. This generation method of duobinary signals shows more tolerance against CD than the one-bit delay method [15]. The filtered sequence drives a Mach-Zehnder (MZ) amplitude modulator between the two voltages of maximum extinction, which results in two-level intensity modulated

optical duobinary signals in which the "1" level can have a phase of either 0 or π [15]. The π-phase flips occurring in the middle of each "0" level cause destructive interference with the finite energies left within the bit-period of "1" levels. As a result, this phenomenon in the duobinary coding confines the energy of "1" in its bit-slot and allows for a much longer transmission distance, compared to NRZ binary signals without any phase shift [16]. The optical duobinary transmitter is shown in Figure 3.2.

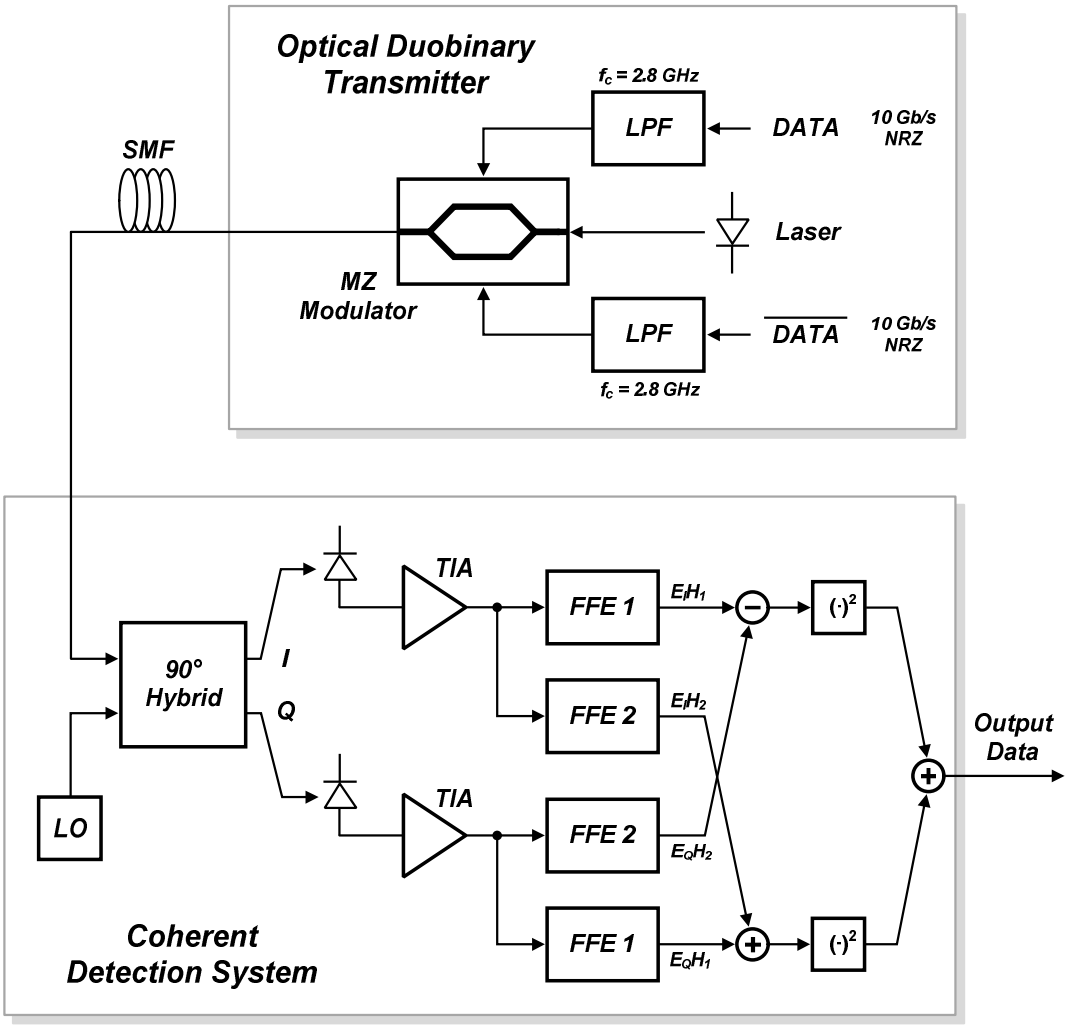

Figure 3.2. Optical duobinary transmitter and coherent detection system with FFEs.

3.1.2 Coherent Detection System

Coherent detection systems concurrently detect the optical signal amplitude, phase, and polarization. The optical coherent detection system, shown in Figure 3.2, is a homodyne receiver that has a higher signal-to-noise ratio and is more practically feasible at high-data rates than its heterodyne counterpart [17]. The major drawback of homodyne detection, its sensitivity to laser phase noise, can be overcome by employing a phase-diversity technique. In this method, photo-detectors generate signals that represent the two quadrature components. When these signals are squared and then summed, a signal that is independent of the laser phase noise is produced [18]. Thus, phase-locking between the transmitter and the local oscillator (LO) laser is less critical in this scheme. Furthermore, coherent detection makes the use of linear electrical equalization possible because the electrical current generated by a photodiode has a linear relationship to the optical field of the input signal [19].

FFEs employed in coherent detection must have a transfer function that is inverse of that of the fiber channel with CD. This fiber impairment is modeled as

$$H_{SMF}(f) = e^{-j\alpha f^2} \tag{3.1}$$

and

$$\alpha = \frac{\pi D L \lambda^2}{c} \tag{3.2}$$

where L is the fiber length, λ is the operating wavelength, D is the fiber dispersion parameter, and c is the speed of light. Thus, the FFEs need to exhibit a transfer function that is

$$H_{FFE}(f) \equiv H_{SMF}^{-1}(f) = e^{j\alpha f^2}, \tag{3.3}$$

which can be expanded into

$$e^{j\alpha f^2} = cos(\alpha f^2) + jsin(\alpha f^2) = H_1(f) + jH_2(f). \tag{3.4}$$

Based on (3.4), FFEs with two different transfer functions (e.g., $FFE_1 = H_1(f) = cos(\alpha f^2)$ and $FFE_2 = H_2(f) = sin(\alpha f^2)$) are required to compensate for CD. In order to determine the placement of FFEs in the receiver, the CD-induced optical field of $E_I + jE_Q$ is multiplied by (3.4), which results in

$$E_{OUT} = \left(E_I \cdot H_1 - E_Q \cdot H_2\right) + j\left(E_I \cdot H_2 + E_Q \cdot H_1\right). \tag{3.5}$$

From (3.5), it can be seen that the in-phase branch is the difference between $E_I H_1$ and $E_Q H_2$, and the quadrature branch is the sum of $E_I H_2$ and $E_Q H_1$. Therefore, the FFEs with two different transfer functions (e.g., FFE_1 and FFE_2) need to be placed in a cross-coupled fashion as shown in Figure 3.2 [20].

3.1.3 System Simulation

The design specification (e.g., number of taps, tap-spacing, bandwidth) of the FFE is determined based on the system simulation result. The required optical signal-to-noise ratio (OSNR) to achieve a bit-error rate (BER) of 10^{-6} as a function of transmission distance is obtained for different FFE configurations. As shown in Figure 3.3 (a), the tap-spacing of 60, 80, 100, and 120-ps are used in the FFE for simulation, and the 100-ps relative delay demonstrated the best performance from 0 to 600-km.

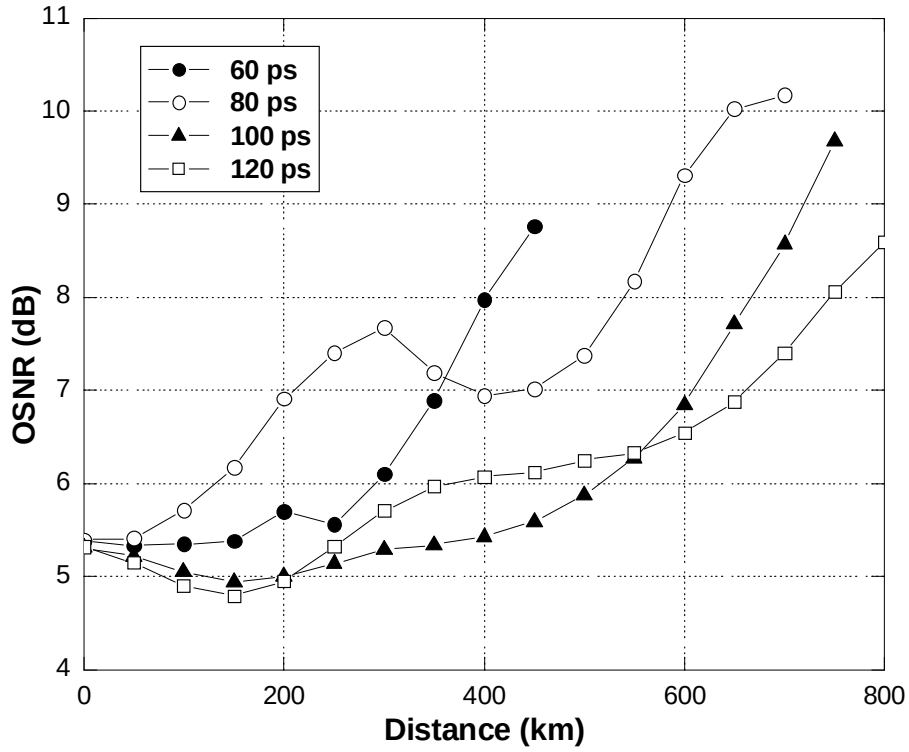

(a)

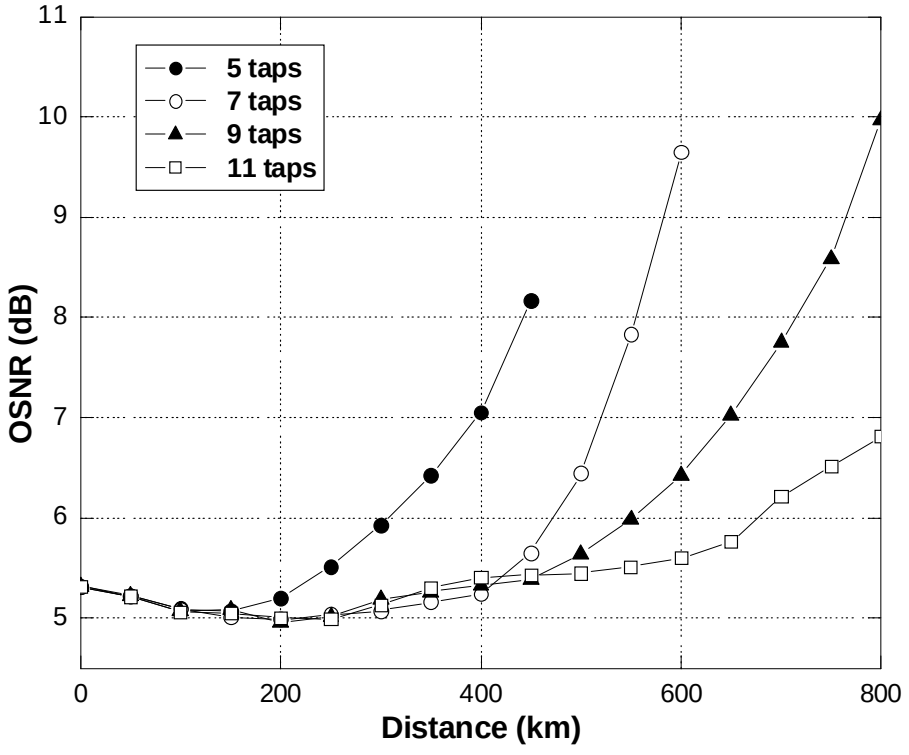

(b)

Figure 3.3. OSNR versus transmission distance for different (a) tap-spacing and (b) number of taps.

Figure 3.3 (b) is used to determine the number of taps to be implemented in the FFE. Although FFEs with both nine and eleven taps reached 600-km with small degradation in OSNR, the 9-tap FFE is chosen because it allows for a simpler implementation than the 11-tap FFE.

The FFE with nine taps and 100-ps spacing is employed to realize a transfer characteristic that is inverse of that of fiber impairment as discussed in the previous section. Plots shown in Figure 3.4 are obtained by adjusting the tap coefficients of FFE_1 and FFE_2 to match $H_1(f) = cos(\alpha f^2)$ and $H_2(f) = sin(\alpha f^2)$, respectively. It can be observed that the frequency response of FFE_1 and FFE_2 exhibit comparable behavior as the theoretical response.

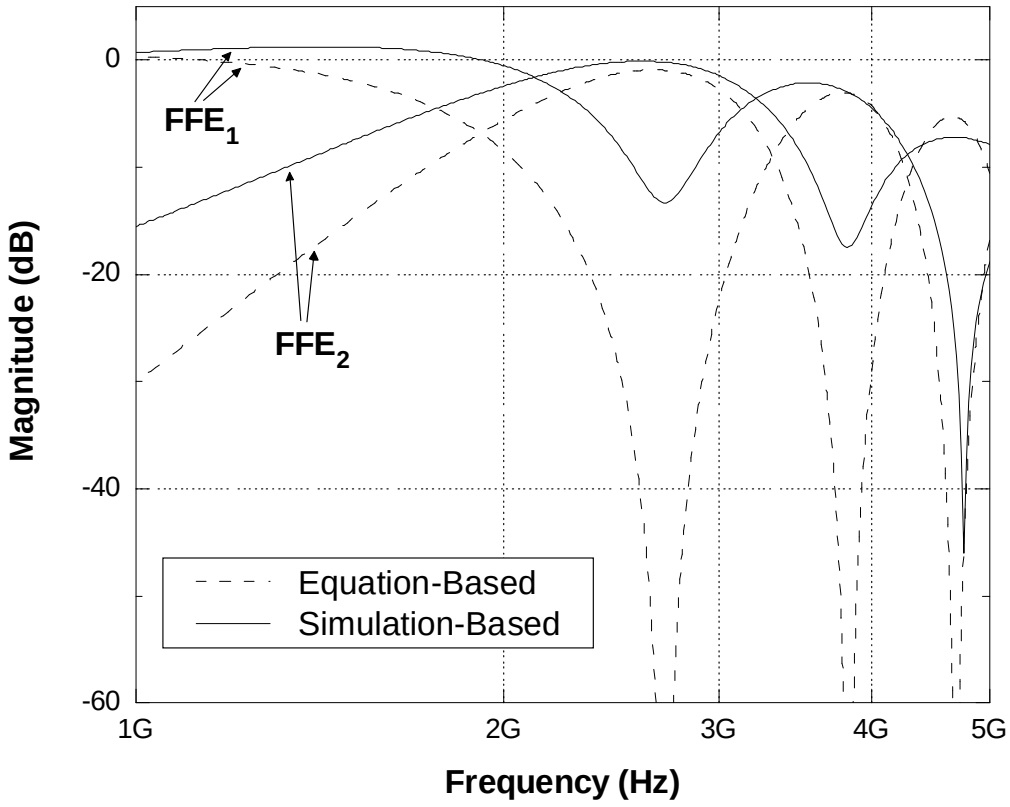

Figure 3.4. Transfer characteristics of two different FFEs used in the optical coherent system.

3.2 Circuit Implementation

3.2.1 Feed-Forward Equalizer

As shown in Figure 3.5, the FFE employed in the coherent optical system is implemented with:

(1) an active delay circuit to provide the tap-spacing of 100-ps,

(2) a variable gain amplifier (VGA) to apply the tap coefficient, and

(3) a resistive load to sum nine branches of the signal in current domain.

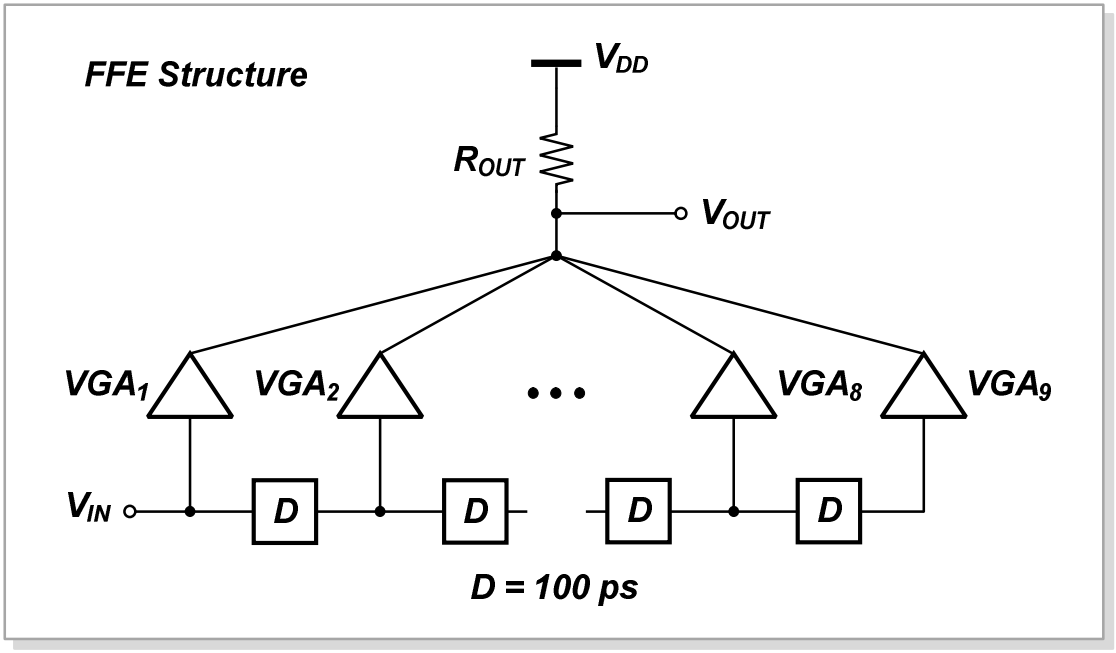

Figure 3.5. Implementation of the FIR filter-based FFE.

System simulation determined that each active delay cell requires a delay of 100-ps, gain of 0-dB, and 3-dB bandwidth of 2.8-GHz. Since the 10-Gb/s data stream is low-pass filtered with a 2.8-GHz filter for duobinary transmission, the bandwidth requirement is

relaxed. An active delay cell is one of the techniques used for delay-line implementation in the FFE. The other approach is to use a passive delay-line that is based on an inductor-capacitor (LC) ladder as shown in Figure 3.6 (a) [21]. A differential implementation can also be designed as shown in Figure 3.6 (b).

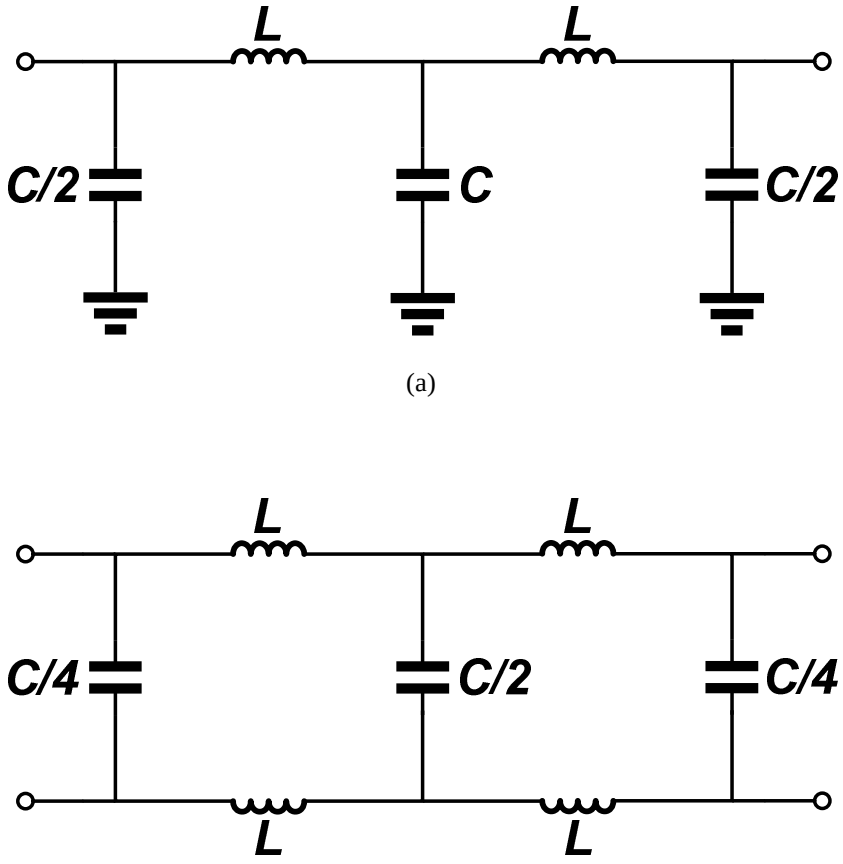

Figure 3.6. 2-stage passive delay line based on a LC ladder structure: (a) single-ended and (b) differential implementation.

The characteristic impedance, Z_o, of this delay structure is

$$Z_o = \sqrt{\frac{L}{C}}, \tag{3.6}$$

and the time delay of each unit delay cell is

$$T_{delay} = \sqrt{L \cdot C}. \tag{3.7}$$

Moreover, the input impedance of the LC ladder is expressed as

$$Z_{in} = \frac{j\omega L}{2}\left(1 \pm \sqrt{1 - \frac{4}{\omega^2 LC}}\right), \tag{3.8}$$

and based on (3.8), the cut-off frequency is derived as

$$\omega_{cutoff} = \frac{2}{\sqrt{L \cdot C}}. \tag{3.9}$$

Thus, by appropriately choosing the inductor and capacitor values, a passive delay line structure with the required characteristic impedance, time delay, and bandwidth can be implemented.

This passive implementation, however, suffers from drawbacks including a large chip area leading to high parasitic loading on signal paths, series loss of the LC ladder, and reflections from terminal impedance mismatch. A differential implementation of the LC ladder, moreover, can require as many as four inductors in a single delay cell to achieve the required bandwidth and tap-spacing of the FFE used in this work [22]. The

active delay-line approach can overcome the previously-mentioned problems at the cost of increased power consumption.

For the delay-line implementation in this study, a bandwidth extension technique is required because multiple single-unit delay cells need to be cascaded to provide the required delay of 100-ps. One technique is to employ an active inductor as the load of each delay cell as shown in Figure 3.7 [21]. Transistors M_3 and M_4 with a resistor in

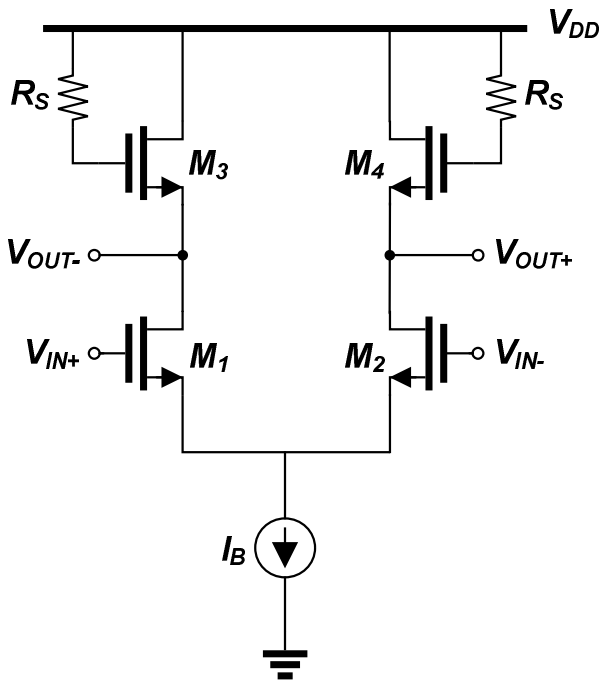

Figure 3.7. Schematic of active inductance peaking delay circuit.

series with their gate act as the active inductors. The impedance looking into the source of M_3 and M_4 is expressed as

$$Z_{out} = \frac{R_S C_{GS} s + 1}{g_m + C_{GS} s}, \tag{3.10}$$

where g_m and C_{GS} is that of M_3 and M_4. Proper choice of values yielding $R_S \gg 1/g_m$ increases $|Z_{out}|$ with frequency, which introduces a zero at $1/R_S C_{GS}$ and consequently, an enhancement in the bandwidth. The delay in this circuit is approximately the time constant of $1/g_m C_L$, where C_L is mainly the C_{GS} of M_3 and M_4 and the following stage. This method, however, consumes very large voltage headroom, which can limit the output signal swing and drive the tail current-source of the following stage into the triode region. Therefore, a capacitive-degenerated differential pair, as shown in Figure 3.8, is used as an active delay cell in this work.

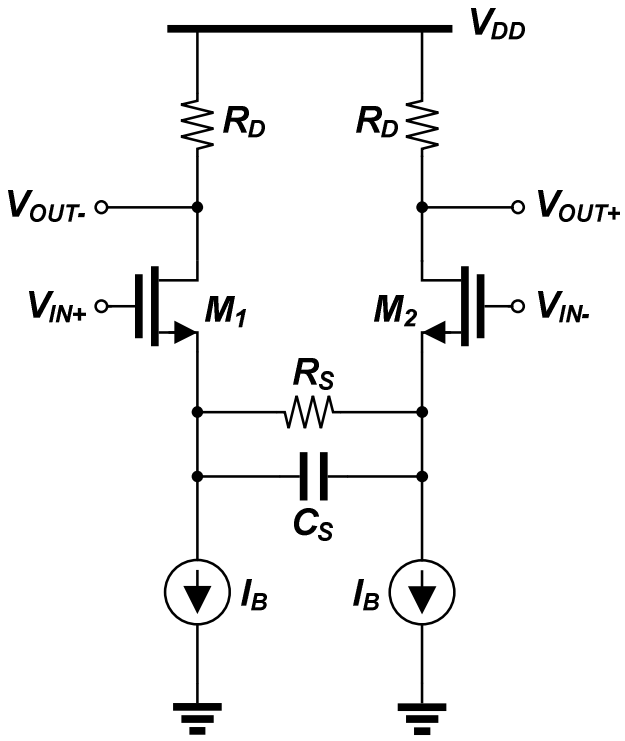

Figure 3.8. Schematic of capacitor-degenerated active delay circuit.

This technique increases the effective transconductance of a differential pair at high frequencies because of the zero introduced by R_S and C_S. The bandwidth extension by a factor of $(1 + g_{m1}R_s/2)$ is achieved when this zero cancels the pole at the output node. The delay in this circuit is due to the time constant of R_DC_L, where C_L is mainly the gate capacitor of the following stage. To meet the required 100-ps relative delay, six such circuits are cascaded to form a single active delay unit.

Another building block required is a VGA to apply tap coefficients. The VGAs employed in the FFE are based on a modified Gilbert cell structure with a folded PMOS current-steering block as shown in Figure 3.9. Since the open-drain outputs of all nine VGAs are connected to a common resistive load, decreasing the voltage headroom consumption of VGAs is necessary and is achieved by employing a folded current-steering block constructed with $M_5 - M_{11}$. The gain of the VGA can be changed from -1 to +1 by controlling V_{CONT} with respect to V_{REF}, and the linearity between the gain and V_{CONT} is enhanced by placing a degeneration-resistor, R_S, in the source terminal of M_5 and M_6.

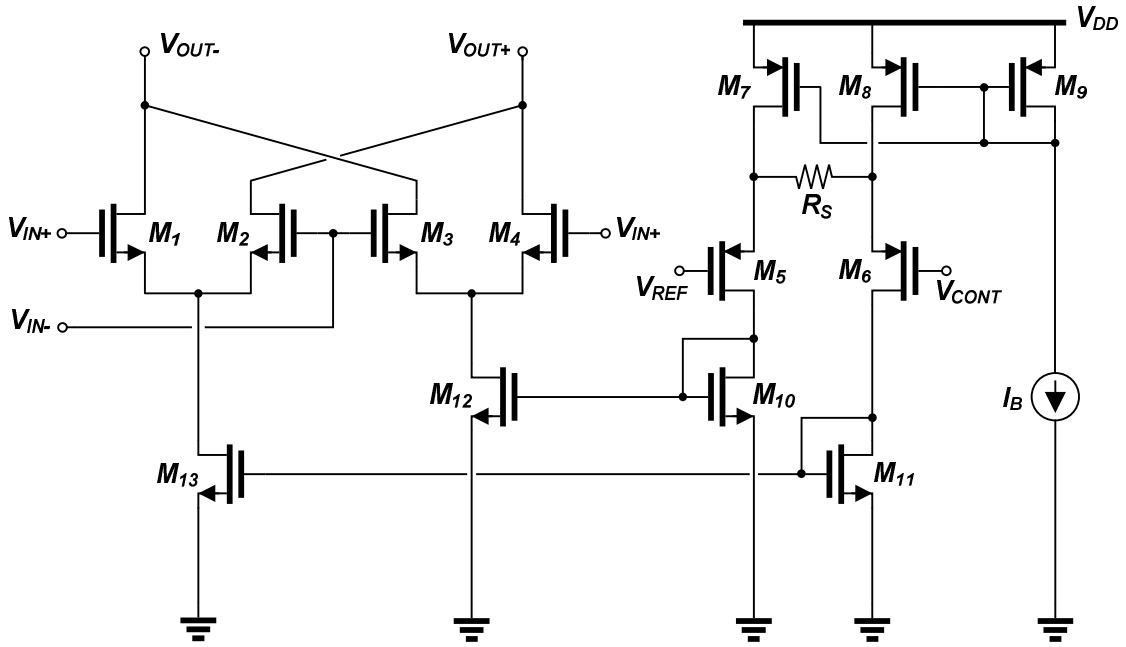

Figure 3.9. Schematic of VGA with folded current-steering block.

3.2.2 Squarer

In the coherent detection system, the in-phase and quadrature signals after the FFEs need to be summed or subtracted before being squared. The circuit shown in Figure 3.10 can perform both the sum-squaring and difference-squaring operations.

To switch between the two operations, the polarity of one input needs to be inverted and the two input ports need to be exchanged. Due to the inherent square law of the MOS transistor operating in the saturation region, the output current flowing across R_{OUT} is

$$I_{OUT} \approx \frac{1}{4} K_n \left(\frac{W}{L}\right)_{3,4} (V_{IN1} \pm V_{IN2})^2, \tag{3.11}$$

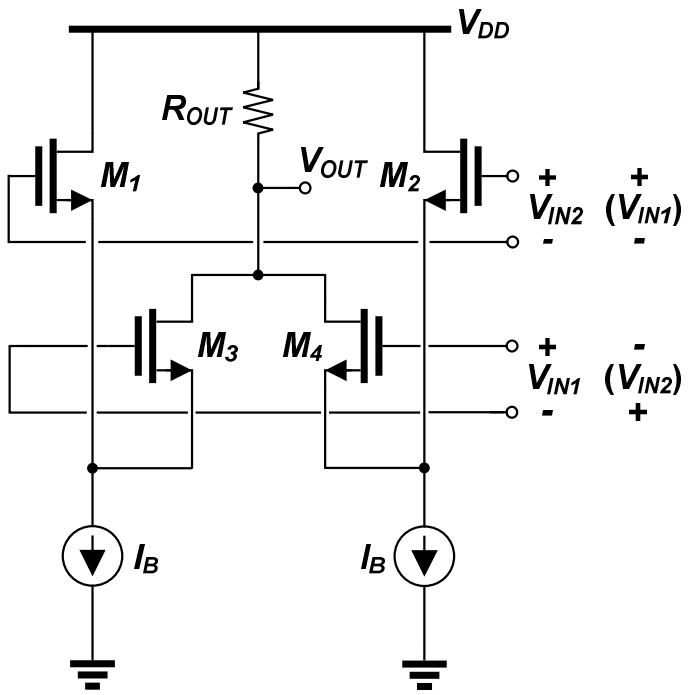

Figure 3.10. Schematic of sum-squarer (voltage polarity in parenthesis is for difference-squarer).

for the sum-squaring circuit and the difference-squaring circuit, respectively [23]. The squaring circuit is followed by an output buffer stage employing series and shunt inductive-peaking techniques to provide enough gain-bandwidth and driving capability. In Figure 3.11, simulated transient signals at the squarer and buffer outputs are compared to an ideal squaring operation when the input to the circuit is a 5-Gbps pseudo-random binary sequence (PRBS) signal.

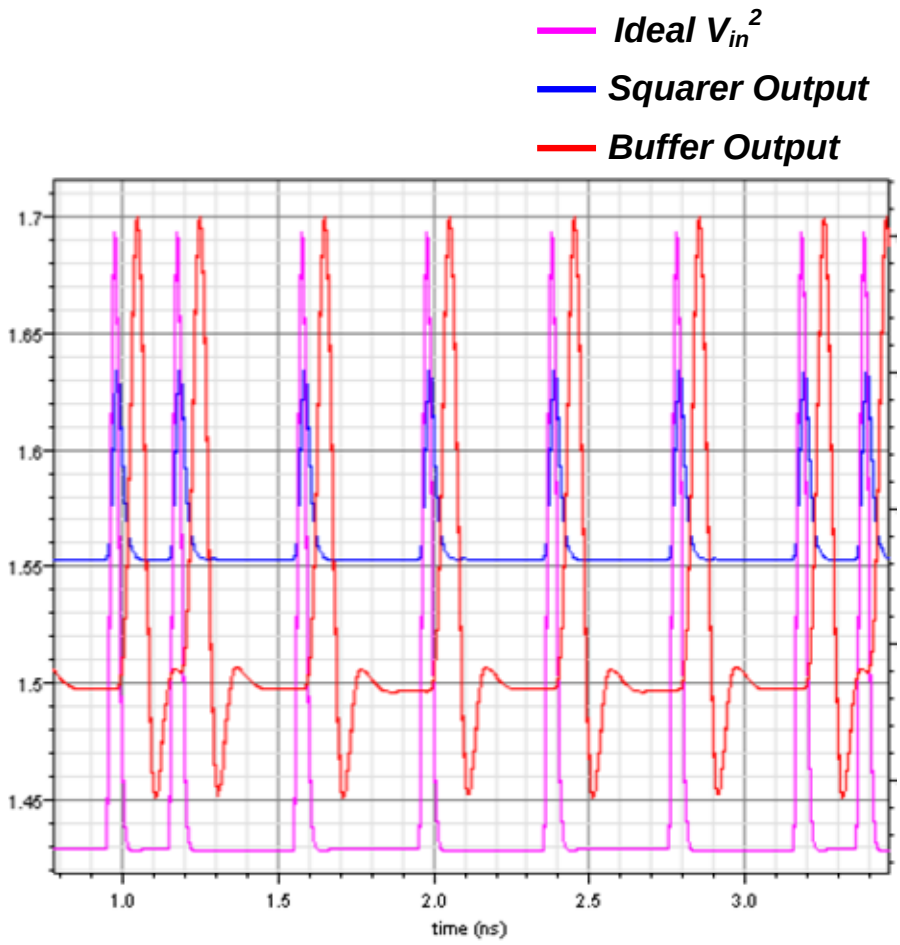

Figure 3.11. Simulated transient response of the squarer compared to an ideal squaring operation.

3.2.3 Tunable Delay

As discussed in previous sections, active delay cells are realized in smaller footprints than the passive counterpart at the cost of higher power dissipation. Moreover, the RC delay (e.g., resistor and gate-capacitance of a transistor) of the active approach is prone to process, voltage, temperature (PVT) variations, whereas the passive LC delay-lines have

practically no sensitivity to the supply voltage and low sensitivity to process and temperature variations. To examine the variation in the 100 ps active delay block, Monte-Carlo simulation with variation over process and temperature (e.g., -40°C, 27°C, 85°C) is performed. As shown in Figure 3.12, the unit delay has a mean value of 100.4 ps,

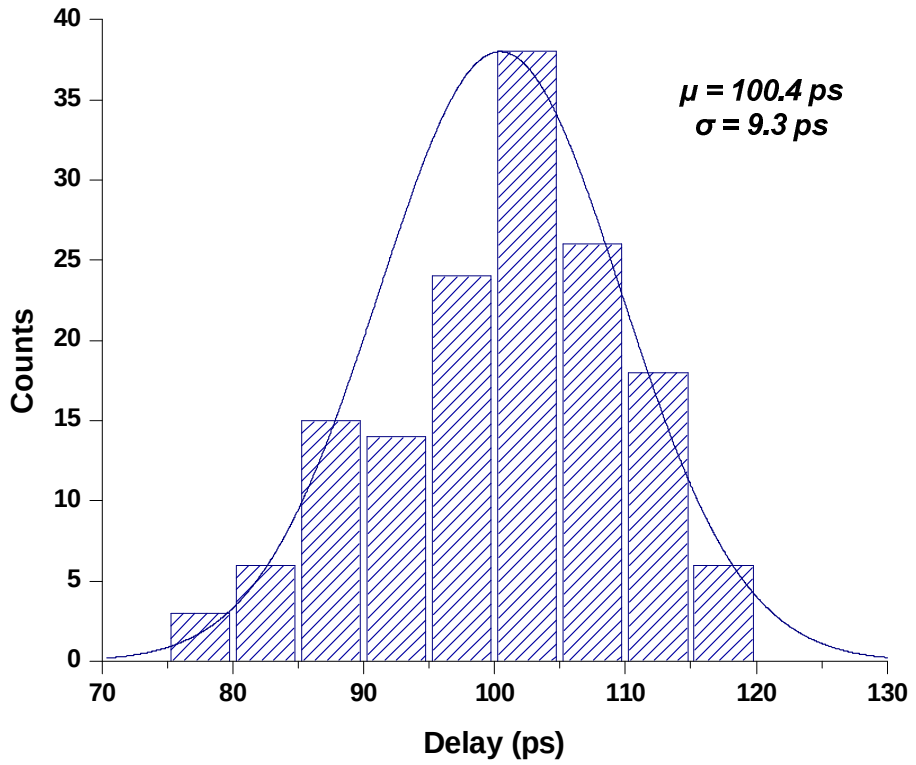

Figure 3.12. Histogram of delay variation over process and temperature of 100-ps active delay cell.

standard deviation of 9.3 ps, minimum value of 76.6 ps, and maximum value of 120.2 ps. This large amount of delay variation can result in sub-optimal compensation of CD as presented earlier in Figure 3.3 (a). A delay-tuning capability, therefore, is required in the active implementation to compensate for the delay variation as large as ±25 ps.

A tunable delay circuit is designed to compensate for delay variations in the active approach. As illustrated by the functional block diagram of the tunable delay-line in Figure 3.13 (a), the signal path is divided into fast and slow paths. The input signal can be

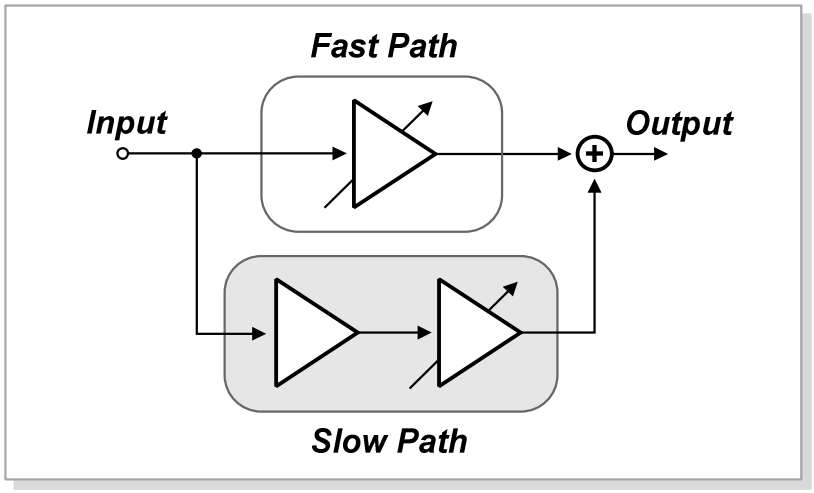

(a)

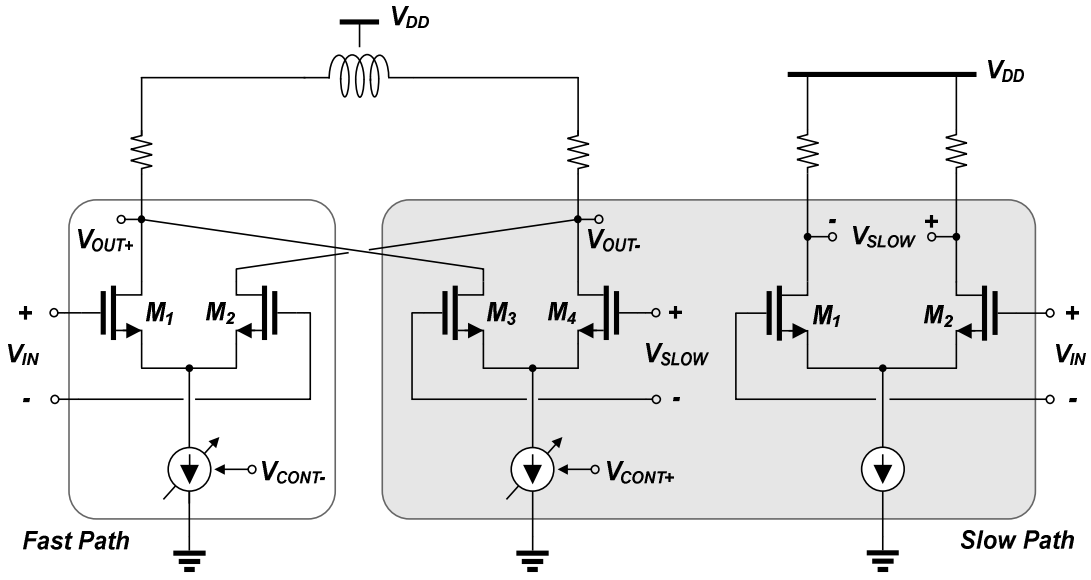

(b)

Figure 3.13. (a) Functional block diagram and (b) schematic of the tunable delay cell.

controlled to travel between the two paths and summed at the output. By adjusting the gain of each path, the total delay at the output can be tuned [24]. In Figure 3.13 (b), the transistor-level implementation of the tunable delay-line is presented. Gain-adjustment of the two paths is performed with the same current-steering block used in the VGA. The delay of this circuit can also change by ±20% due to PVT variations, so delay-tuning between 80 to 120 ps is required. As shown in Figure 3.14 (a) and (b), the required tuning range is achieved by the tunable delay circuit.

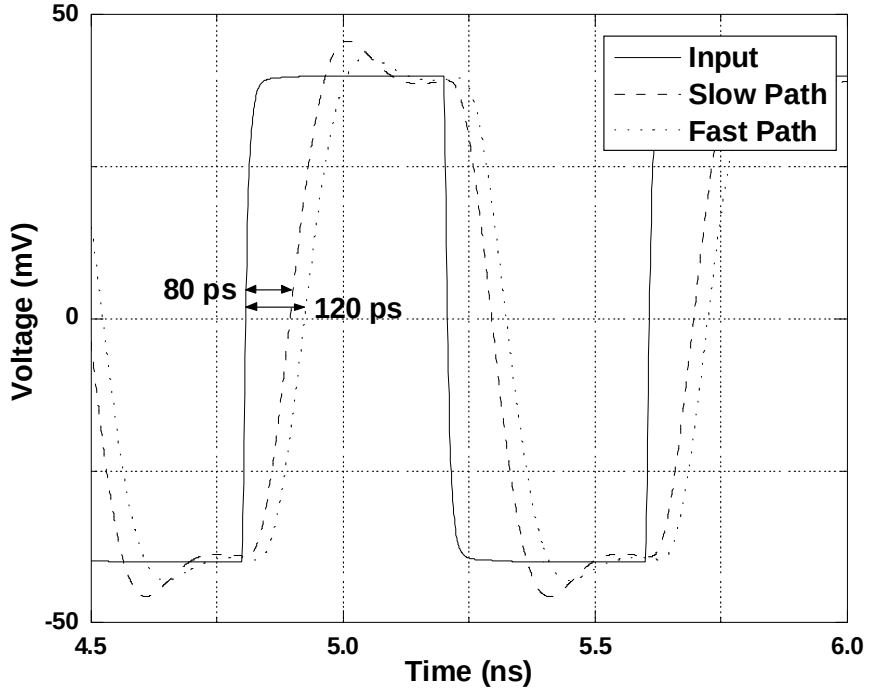

(a)

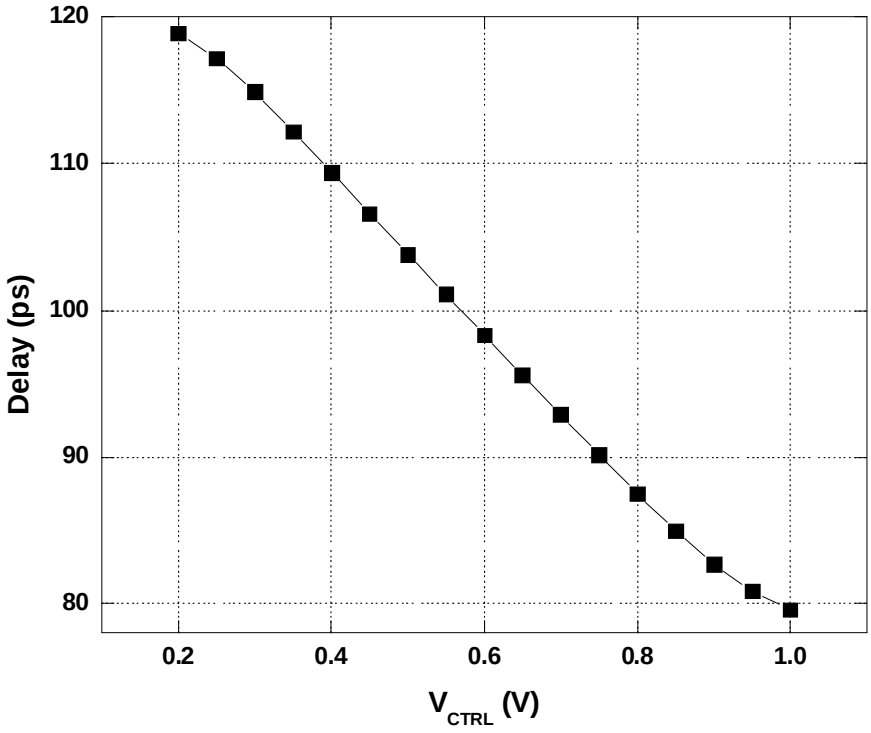

(b)

Figure 3.14. (a) Transient response for the two extreme delay settings, and (b) delay-tuning range versus control voltage.

3.3 Results

The FFE, squarer, and tunable delay circuits are all designed and fabricated in a 0.18 µm CMOS technology. Figure 3.15 shows the microphotograph of the FFE chip, which measures 1.05 × 0.60 mm^2 including the pads (the active area only occupies 0.85 × 0.30 mm^2).

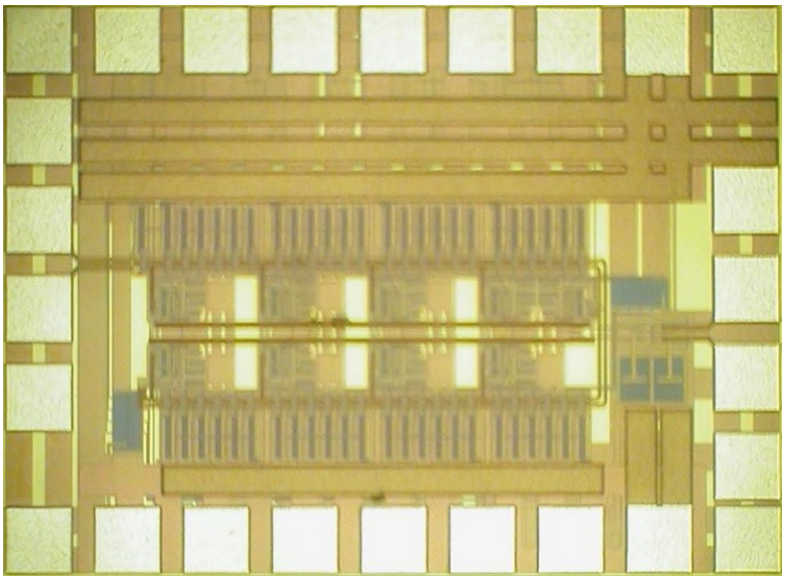

Figure 3.15. Microphotograph of FFE.

The die photo of the squarer is shown in Figure 3.16, which has an area of 0.98 × 0.78 mm^2, where much of the chip area is occupied by the inductors used in the output buffer stage. Lastly, the die photo of the tunable delay circuit is shown in Figure 3.17.

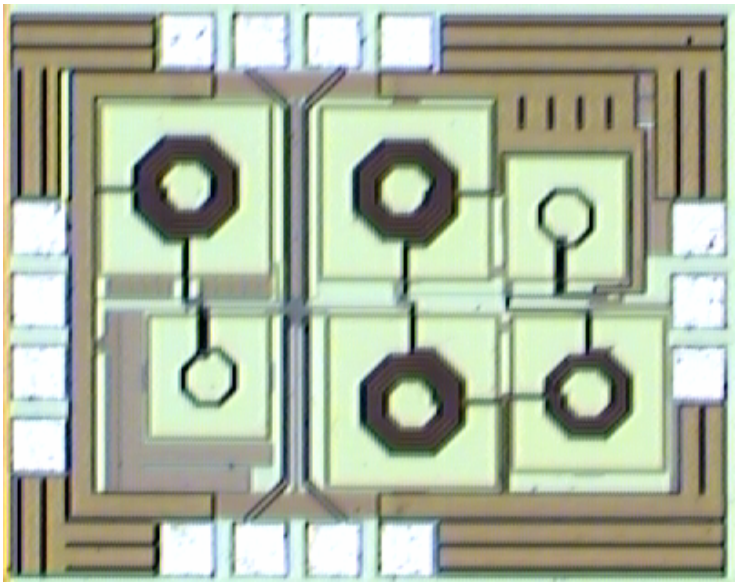

Figure 3.16. Microphotograph of the squarer.

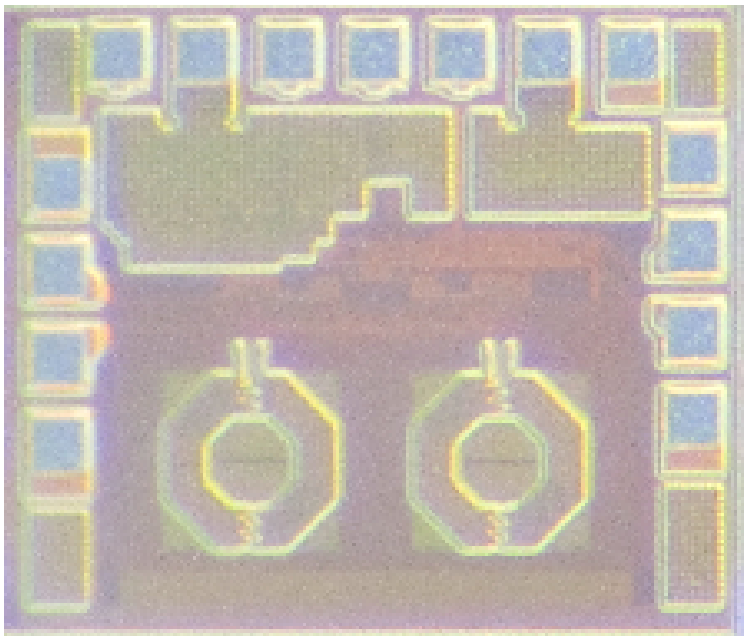

Figure 3.17. Microphotograph of the tunable delay circuit.

The output transient response at each of the nine taps for a step input is shown in Figure 3.18, and the relative delay between the taps is 100 ps with ±5 ps variations as listed in Table 3.1. Figure 3.19 shows the measured phase response of the FFE at tap 1 through tap 9. The constant slope of the phase response for all nine taps indicates that the group delay is fairly uniform between each tap; as the group delay is proportional to the negative derivate of the phase. In Figure 3.20 (a) and (b), the measured and simulated frequency responses of the FFE at tap 1 and tap 9 are plotted, respectively. The FFE meets the required bandwidth of 2.8 GHz at both tap 1 and 9.

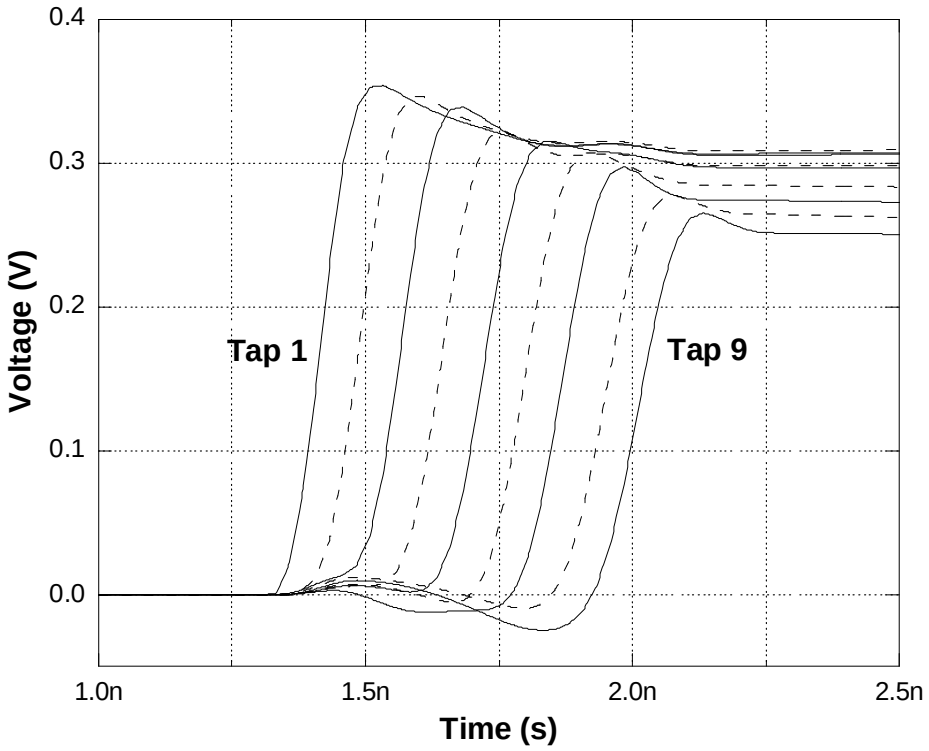

Figure 3.18. Output transient response at tap 1 through 9.

Table 3.1. Measured Tap-Spacing of the FFE

	Tap-Spacing
Tap 1 and 2	98 ps
Tap 2 and 3	99 ps
Tap 3 and 4	102 ps
Tap 4 and 5	102 ps
Tap 5 and 6	100 ps
Tap 6 and 7	98 ps
Tap 7 and 8	101 ps
Tap 8 and 9	95 ps

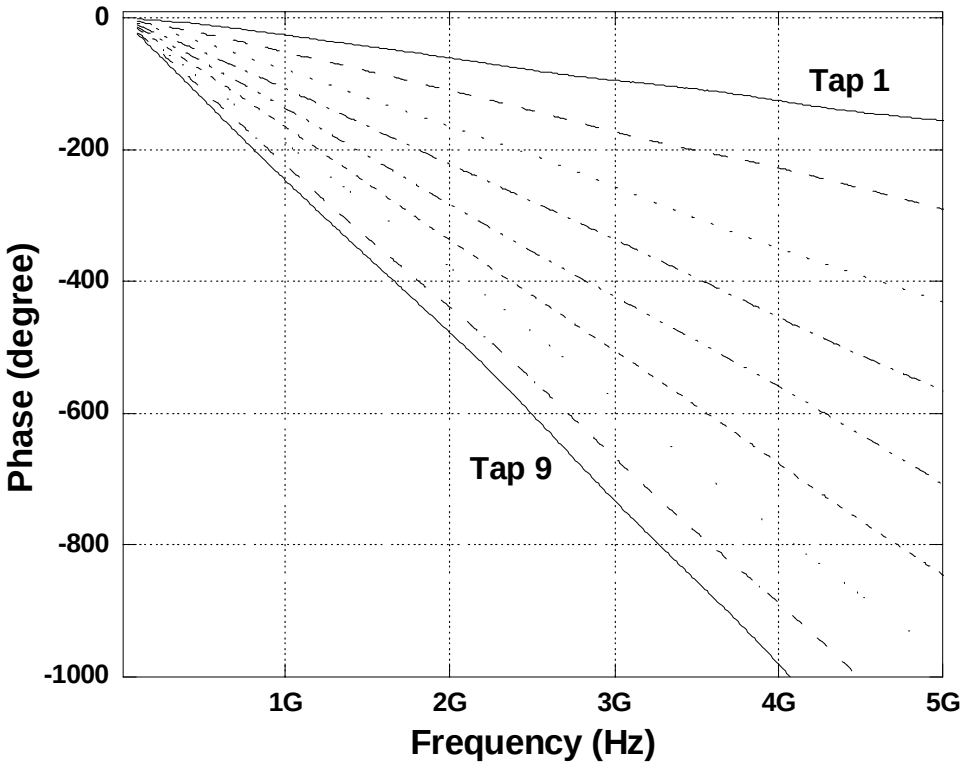

Figure 3. Measured phase response of the FFE at tap 1 through tap 9.

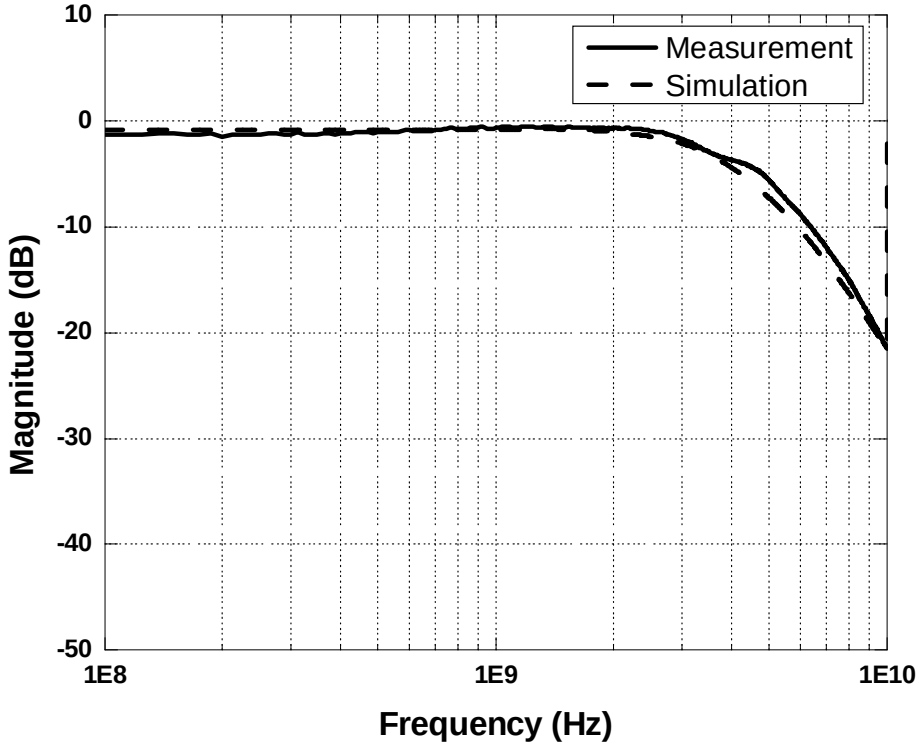

(a)

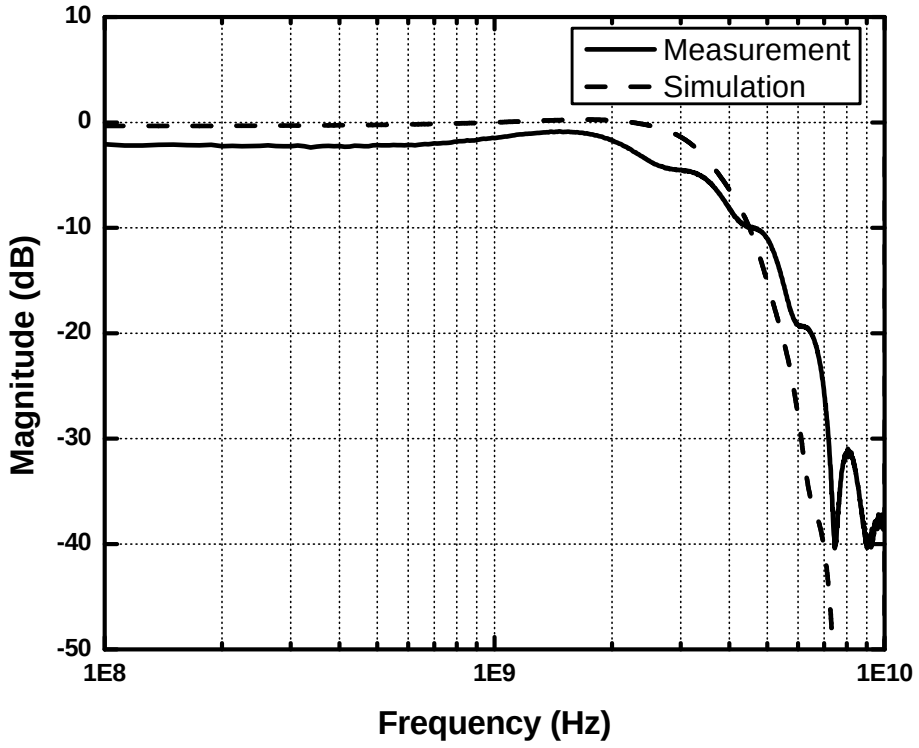

(b)

Figure 3.20. Simulated versus measured frequency response of the FFE at (a) tap 1 and (b) tap 9.

Lastly, the required OSNR to achieve a BER of 10^{-6} as a function of transmission distance is plotted in Figure 3.21 for three different cases; NRZ transmission, and optical duobinary transmission with and without FFEs. For a 3 dB OSNR penalty with respect to the back-to-back configuration requiring an OSNR of 4.3 dB, transmission distance of 80 km and 200 km are obtained for NRZ and optical duobinary formats, respectively. By employing FFEs with the duobinary scheme, optical link distance is further extended to 600 km.

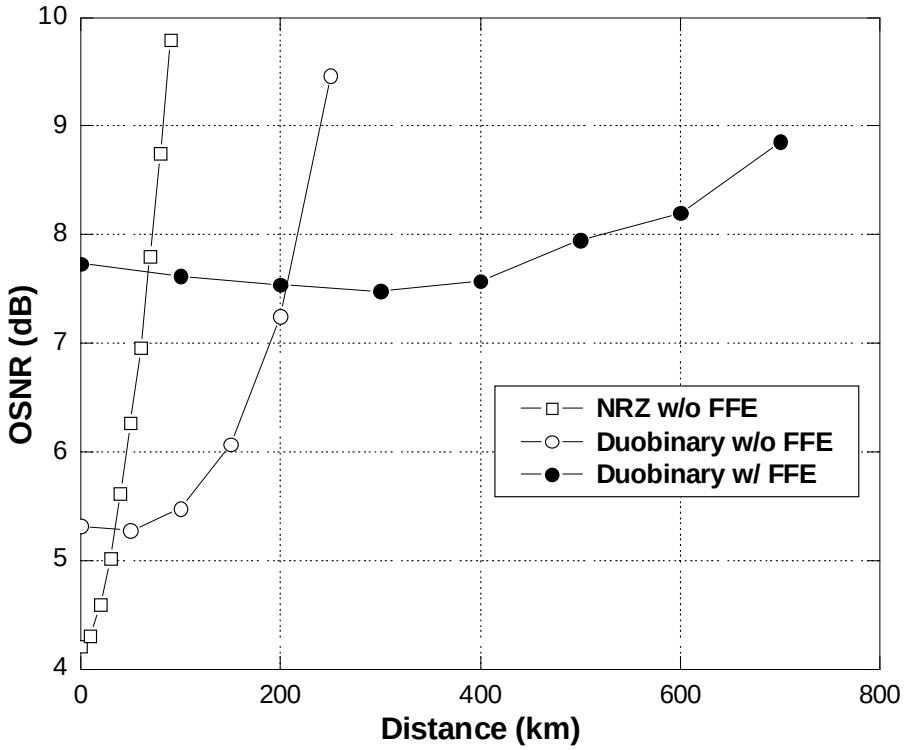

Figure 3.21. OSNR versus distance for NRZ and duobinary transmission with and without FFE.

3.4 Conclusions

A 10 Gb/s coherent detection system incorporating FFEs and an optical duobinary modulation format has been studied as a preliminary research. The FIR filter-based FFE has nine taps and utilizes capacitive-degenerated differential pairs for the delay block. The squarer is designed to be used for the phase-diversity technique in the coherent detection system. The FFE and squaring circuits are implemented in a 0.18 μm CMOS technology and measure 1.05 × 0.60 mm^2 and 0.98 × 0.78 mm^2, respectively. The coherent detection system, combined with optical duobinary coding and FFEs, demonstrated the capability to extend the transmission reach of long-haul optical systems over SMF to 600 km.

CHAPTER

4

Signal Integrity in Wireless Systems

4.1 Wireless Communication Systems

After addressing the signal integrity issues and proposing a viable enhancement technique for optical communication systems in the previous chapters, this chapter examines signal integrity in the RF wireless systems. In recent years, with the advancement of wireless technology and explosive growth in number of mobile users, the importance of maintaining high level of signal integrity at the RF front-end is greater than ever before; and only the radio devices with high receiver sensitivity can achieve good performance in today's heavily-crowded wireless environment. Moreover, most of the modern wireless communication systems require a full-duplex operation which enables them to transmit and receive data as a two-way communication. Therefore, as a target

application of this research, a direct conversion front-end architecture in a full-duplex communication system is studied. In a full-duplex system, a receiver is subject to interference from the transmitter leakage signal, and this impairment degrades the receiver sensitivity and needs to be compensated for. The proposed research, therefore, is aimed at developing an active cancellation circuit to reject the transmitter leakage.

4.2 Transmitter Leakage

In a full-duplex communication system, both transmission and reception of data are performed simultaneously. Two simplest methods of achieving "two-way communication" are time-division duplexing (TDD) and frequency-division duplexing (FDD) as shown in Figure 4.1 [25]. In TDD, both uplink and downlink signals are transmitted in the same

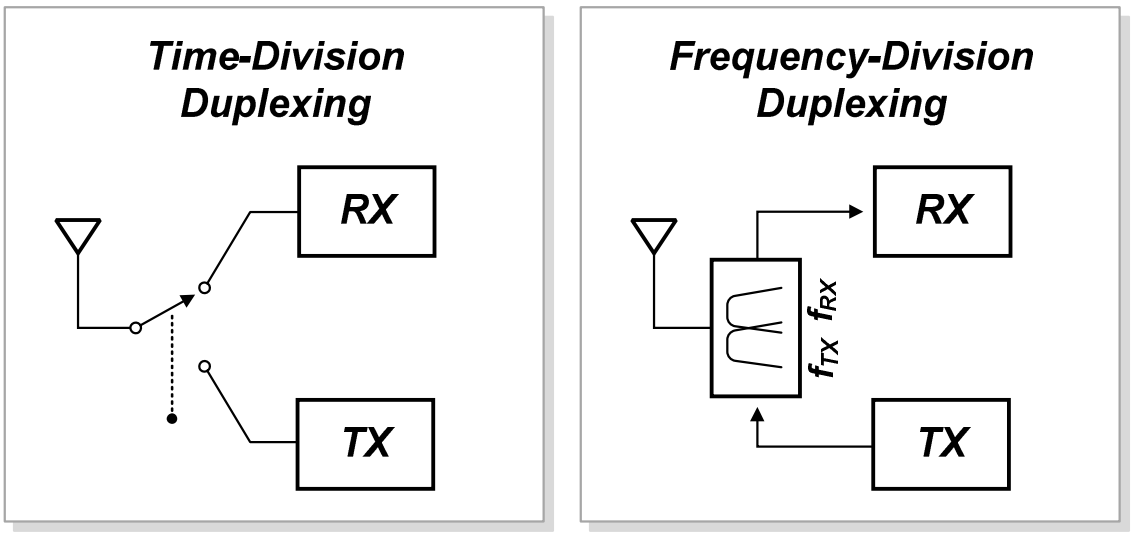

Figure 4.1. Generation of XMD due to the TX leakage.

frequency band but at different times; an RF switch is employed after the antenna to switch between transmit and receive paths. In FDD systems, a three-port “duplexer” composed of two band-pass filters (i.e., see Figure 4.2 (a)) is incorporated after the antenna to allow simultaneous transmission of uplink and downlink signals that are allocated in different frequency bands.

One of the dominant sources of interference in a full-duplex wireless system is the leakage signal generated from the transmitter (TX) due to the insufficient isolation between the receiver (RX) and TX. The leakage problem has more severe effect in FDD applications because the antenna duplexing filter incorporated between the TX and RX paths only provide finite isolation from 50 to 60 dB as shown in Figure 4.2 (b). For example, in a wideband code division multiple access (WCDMA) system, the maximum TX power of +26 dBm can result in a TX leakage of -29 dBm at the RX input with 55 dB isolation provided by the duplexer. Although in a different frequency band, the TX leakage signal can be as much as 85 dB stronger than -114 dBm of the minimum detectable signal (MDS) for the receiver. This strong TX leakage power is further amplified by the LNA and can generate interference in the RX band through different distortion mechanisms. In TDD systems, the TX and RX paths operate in different time slots; therefore, sufficient isolation is provided between the two ends.

Although there are various cellular standards based on FDD operation, this study concentrates on WCDMA based wireless systems because of their worldwide usage for voice and data communication. Several frequency bands have been assigned to WCDMA systems, and this work focuses on “Band I” which is widely employed in Europe, Asia,

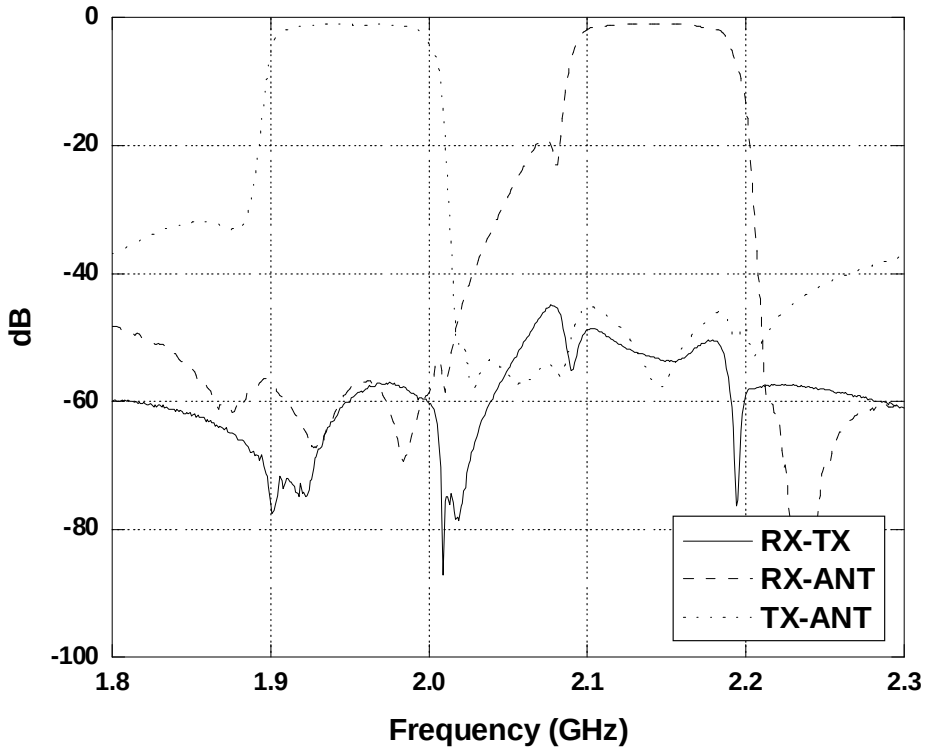

(a)

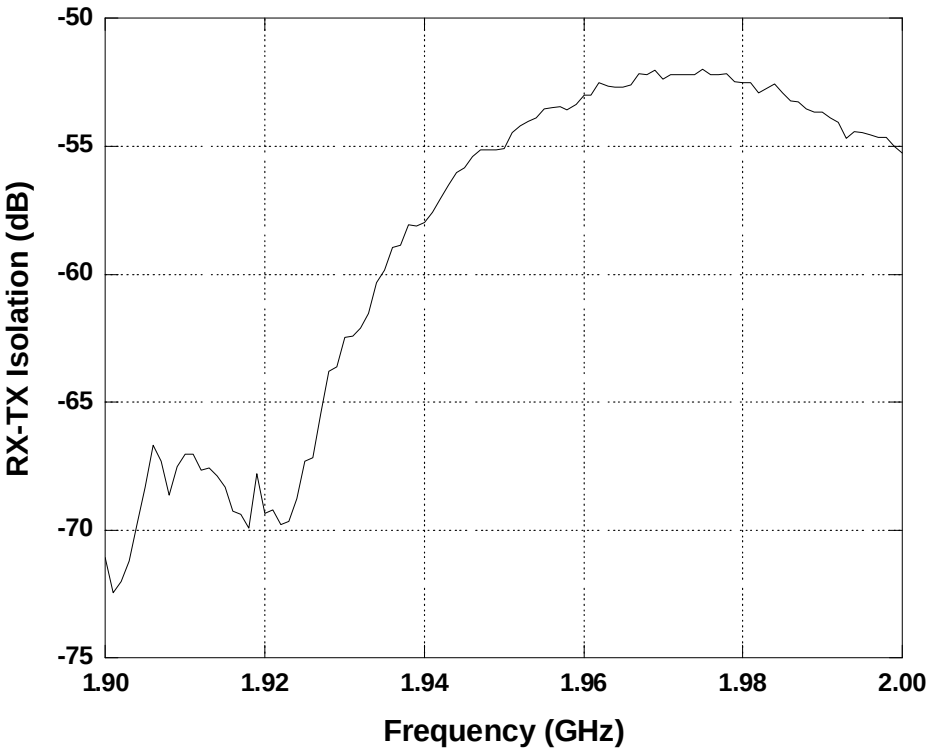

(b)

Figure 4.2. (a) Frequency response of a typical duplexer and (b) RX-TX isolation.

Africa, and parts of America. Table 4.1 lists some of the WCDMA specifications for Band I operation [26].

Table 4.2. WCDMA Band I Specifications

Parameter	Specification
TX Frequency Band	1920 – 1980 MHz
RX Frequency Band	2110 – 2170 MHz
Maximum TX Power	+24 dBm
Channel Spacing	5 MHz
Chip Rate	3.84 Mcps
Reference Sensitivity Level	-117 dBm / 3.84 MHz

4.2.1 Second-Order Intermodulation Distortion

The TX leakage signal can degrade the RX sensitivity in two ways: (1) it can increase the second-order intermodulation distortion (IMD_2) after the down-conversion process, and (2) it can generate cross-modulation distortion (XMD) in the presence of a strong jammer.

When the mobile device is located at the edge of a cellular boundary, the received signal from the base station is very weak, while the transmitted signal from the power amplifier (PA) is at the maximum allowed power level. In this case, the TX leakage signal can result in significant interference in the receiver chain. With direct conversion receiver (DCR) or homodyne architectures gaining more widespread usage due to their simplicity and lower cost over the heterodyne counterparts, more attention needs to be paid at the interference problems from the TX leakage; because in a DCR, the RF signal

is down-converted straight to baseband, and the modulated TX leakage signal creates interference falling in baseband due to the second-order distortion in the down-converter. This type of distortion is IMD_2 and its conceptual illustration is presented in Figure 4.3.

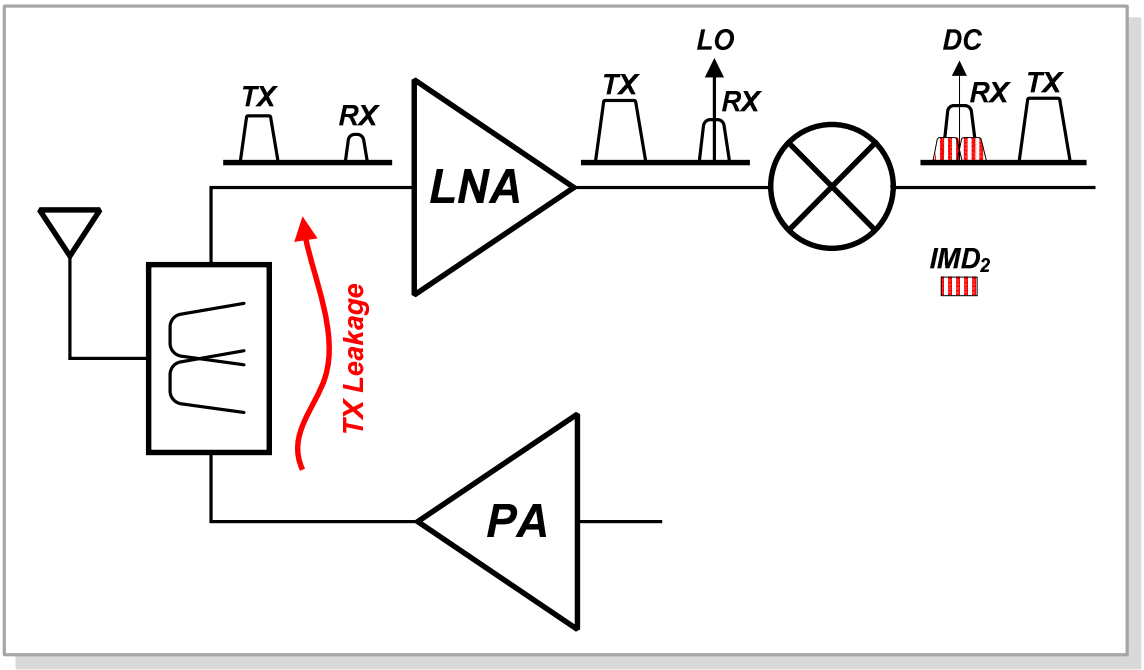

Figure 4.3. Generation of IMD_2 due to TX leakage.

In WCDMA system, the user bit rate is defined as 12.2 kpbs and spread chip rate is 3.84 Mcbs for the BER of 0.001. The processing gain, G_P, in this case is computed as

$$G_P = 10 \log_{10} \left(\frac{3.84 \text{ MHz}}{12.2 \text{ kbps}} \right), \tag{4.1}$$

which equals 25 dB. The ratio of bit energy of the dedicated physical channel (DPCH) to the total noise, E_b/N_t, for the defined BER is around 7 dB, including a practical

implementation margin of 2 dB. Moreover, as listed in Table 4.1, the sensitivity level is defined as –117 dBm. Thus, the processing gain of 25 dB increases the received signal from –117 dBm to –92 dBm; and since the received signal power should be greater than the noise floor by an amount equal to E_b/N_t = 7 dB, the noise floor is calculated to be –99 dBm. In WCDMA specifications, the maximum TX power should not exceed +24 dBm; therefore, the output power of PA, P_{PA}, will reach up +26 dBm since the duplexer loss is around 2 dB. With a 55 dB isolation from the duplexer, the TX leakage power at the LNA input would be –29 dBm. From these numbers, the second-order intercept point, IIP_2, can be computed as

$$IIP_2 = 2 \cdot P_{PA} - IMD_2, \tag{4.2}$$

where IMD_2 is the LNA input referred IMD_2 power due to the down-converter distortion. This IMD_2 level should be 9 dB below the noise floor so that the noise floor is not increased by more than 0.5 dB. Therefore, the IMD_2 level is set as –99 dBm – 9 dB = –108 dBm, and the IIP_2 requirement for the TX leakage signal is computed as 2·(–29 dBm) – (–108 dBm) = +50 dBm. This down-converter IIP_2 requirement is extremely challenging to meet as the LNA has fairly high gain (i.e. usually greater than 15 dB) at the TX frequency. Therefore, a method to suppress the TX leakage is required in order to mitigate the IMD_2 problem.

4.2.2 Cross-Modulation Distortion

Another problem caused by TX leakage is the generation of XMD in the presence of a strong continuous wave (CW) blocker. When a strong single-tone jammer, or an undesired signal with large amplitude, is present in the vicinity of the RX band, the leaked TX modulation will cross-modulate with the interference tone due to nonlinearities in the LNA. Although both the TX leakage and jammer are not in the RX band, the spectrum of the cross-modulation products partially fall into the RX band and desensitize the receiver chain if the cross-modulation product is large enough. This RX-band distortion mechanism is called XMD, and it increases the noise level and degrades the RX sensitivity as shown in Figure 4.4 [27].

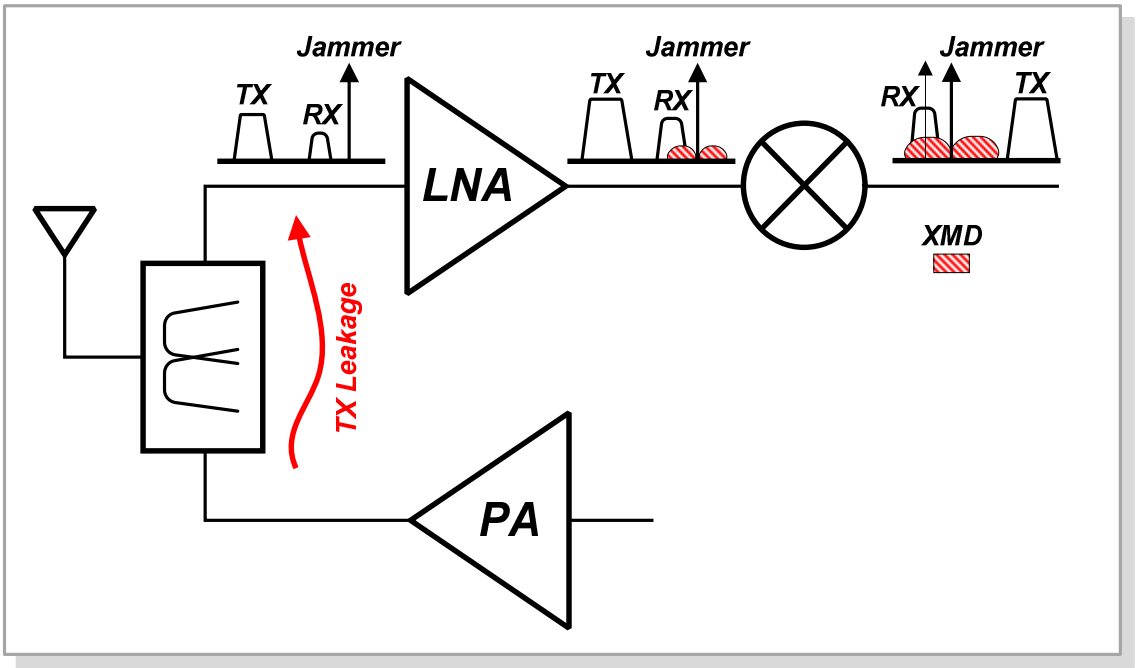

Figure 4.4. Generation of XMD due to TX leakage.

To further analyze the XMD, the single-tone jammer and the TX leakage can be approximately expressed as

$$x_{J+TXL}(t) = A_J \cos \omega_J t + A_{TXL} \cdot m_A(t) \cos \omega_{TX} t\,, \tag{4.3}$$

where A_J is the amplitude of single-tone jammer, ω_J is the angular frequency of the jammer, A_{TXL} is the average level of the TX leakage signal, ω_{TX} is the TX angular frequency, and $m_A(t)$ is the amplitude modulation of the TX signal which has a fundamental frequency equal to the WCDMA chip rate of 3.84 MHz [27]. The jammer and TX leakage, $x_{J+TXL}(t)$, is amplified by the LNA with a nonlinearity; thus, at the output of the LNA, the terms associated with the jammer frequency are generated as

$$y_J(t) = \left[a_1 A_J + \frac{3}{2} a_3 A_J A_{TXL}^2 m_A^2(t)\right] \cos \omega_J t\,, \tag{4.4}$$

where a_1 and a_3 are the 1st and 3rd order nonlinear coefficients, respectively. In (4.4), $a_1 A_J$ is the amplified jammer signal and $\frac{3}{2} a_3 A_J A_{TXL}^2 m_A^2(t)$ is the XMD term induced by the third-order distortion caused by the LNA nonlinearity. Since the XMD term is the product of the first order of the jammer signal, A_J, and the second order of the TX leakage signal, A_{TXL}^2, the spectrum of the XMD has double the bandwidth of the desired RX signal as shown in Figure 4.5.

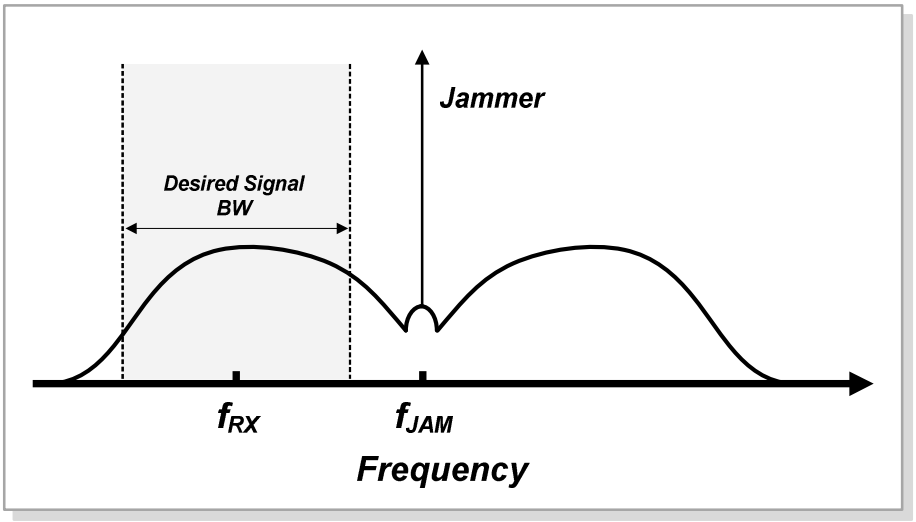

Figure 4.5. Spectrum of XMD falling in the RX band.

4.3 Transmitter Leakage Rejection Methods

The most commonly used method for suppressing the two distortion mechanisms in a full-duplex system is to insert an external surface acoustic wave (SAW) filter in RX path between the LNA and the mixer as shown in Figure 4.6. SAW filters are constructed on a piezoelectric substrate. The inter-digitized transducers (IDTs) are used at the input and the output of the SAW filter to convert acoustic waves to electrical waves and vice versa by exploiting the piezoelectric effect of the substrate. Moreover, the absorbers are placed at two ends of the substrate to mitigate interference from the reflecting waves [28]. The basic structure of the SAW filter is illustrated in Figure 4.7.

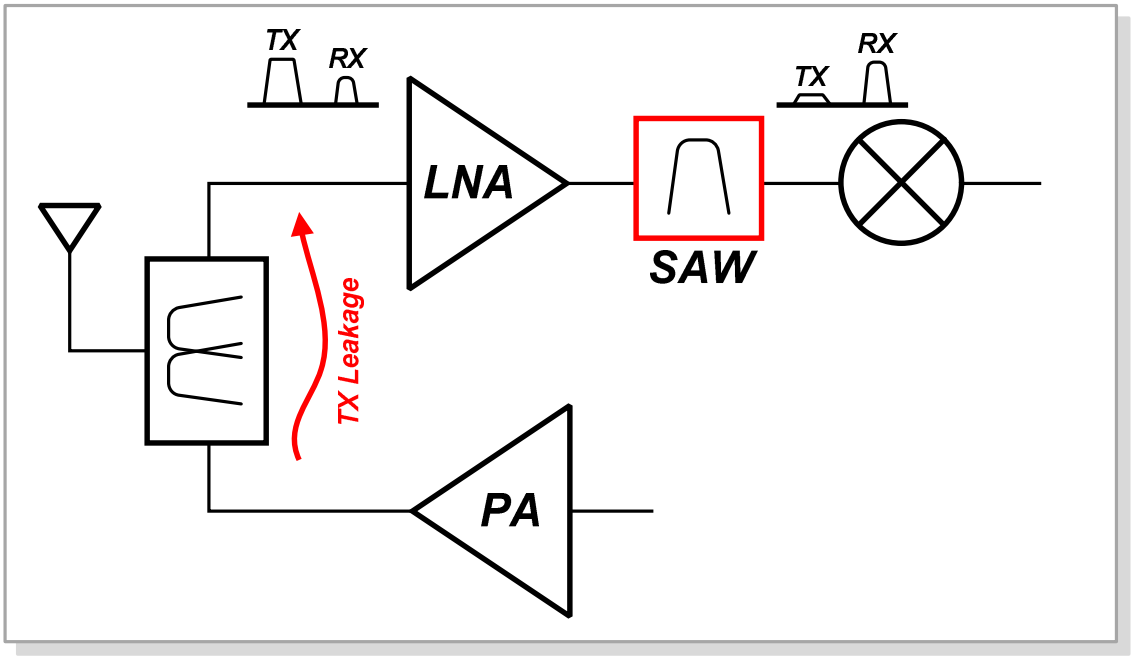

Figure 4.6. Placement of SAW filter in the RX path to suppress TX leakage.

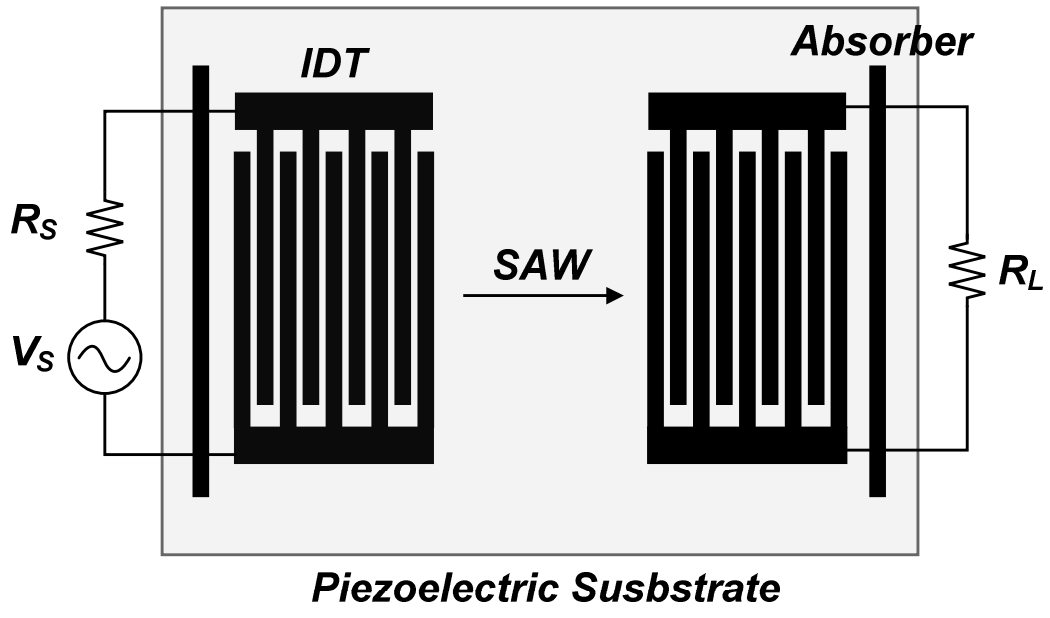

Figure 4.7. Surface acoustic wave filter.

RF filters for WCDMA using SAW technology have an insertion loss of around 3 dB and can provide additional 25 dB of isolation at TX frequency. Unfortunately, as these filters are constructed on a piezoelectric substrate, they cannot be integrated with the rest of the receiver on a silicon substrate; so they have to be packaged separately. Moreover, because SAW filters are off-chip components, additional matching components are needed for the integration between the filters and receiver. Use of SAW filters, therefore, not only increases the size of the transceiver but also drives up the overall cost considerably. Hence, an alternate TX leakage rejection method that can be easily integrated with the rest of the RF circuitries is a desirable solution for signal integrity enhancement in RF systems.

Several TX leakage suppression techniques using the active circuitries to avoid the use of a SAW filter have been studied. One of the techniques was presented by Darabi in late 2007, and this technique attempts to filter out the blocker near the RX frequency band instead of the actual TX leakage signal [29]. Thus, as an attempt to reject the blocker, both of the RX signal and blocker are down-converted to or near direct-current (DC), then the RX signal is filtered out using a high-pass filter (HPF), and the blocker alone is up-converted back to RF and subtracted at the LNA output. This blocker suppression process is illustrated in Figure 4.8. Both of the down-conversion and up-conversion mixers use the RX LO for frequency translation. The down-conversion is employed in this method because a sharp filtering of the closely located signals can be performed more easily at DC then at RF. This method demonstrated around 20 dB of blocker suppression, which is comparable to the rejection obtained from a SAW filter. There is, however, a downside from this blocker filtering method; due to the noise from

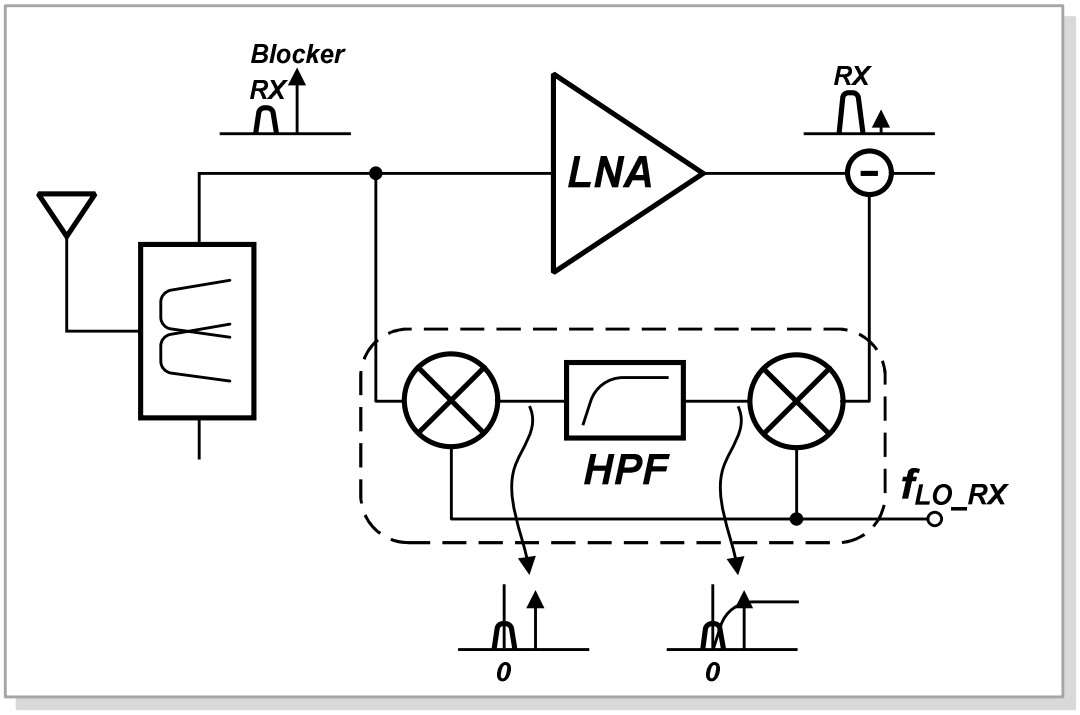

Figure 4.8. Blocker suppression method using down-converters for filtering at DC.

the up-conversion mixer and sampling of the RF signal at the LNA input, the NF of the LNA is significantly increased. The measured NF of the LNA is degraded by 2.9 dB, increasing from 3.9 dB before filtering to 6.8 dB after filtering.

Another TX leakage suppression that is based on utilizing the auxiliary path to filter out the TX leakage signal after down-conversion was proposed by Ayazian et. al [30] as shown in Figure 4.9. In [30], a prototype system is implemented using discrete components which include a broadband LNA, phase shifter, RF VGA, passive IQ demodulator and modulator, HPFs and LPFs, and broadband amplifier. This prototype is tested at a lower frequency band of 870 to 890 MHz and achieves 23.5 dB of cancellation.

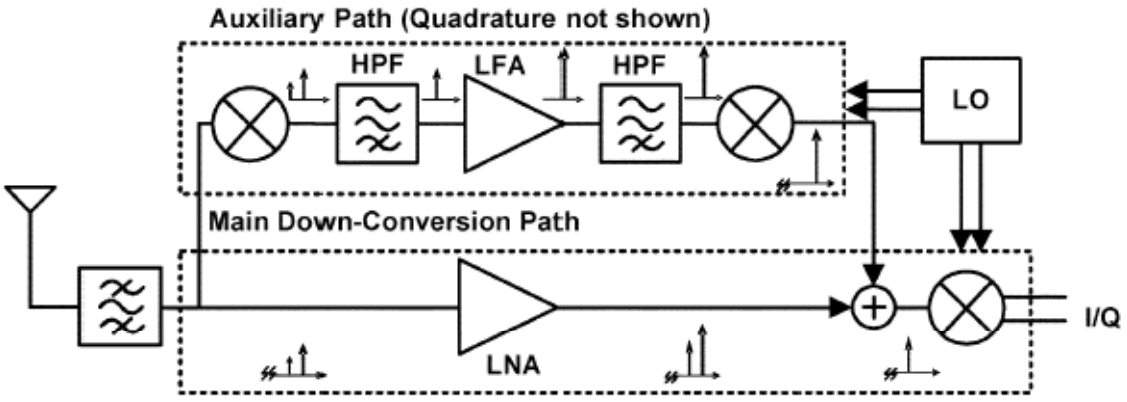

Figure 4.9. TX leakage suppression based on utilizing an auxiliary path [30].

Safarian et. al [31] proposed a blocker filtering technique this is very similar to the work of Darabi explained earlier. As shown in Figure 4.10, the blocker filtering technique in [31] generates the replica signal from the output of the LNA in a feedback fashion unlike the feed-forward scheme implemented in [29]. This feedback cancellation technique is designed and fabricated in 0.18 μm CMOS technology and targeted for WCDMA applications. The gain of the LNA degrades by 0.4 dB and the NF increases by 0.3 dB when the blocker filtering is enabled.

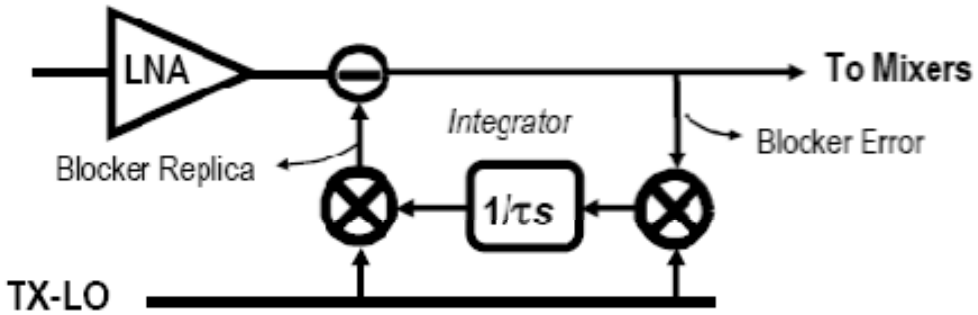

Figure 4.10. Feedback blocker filtering technique [31].

CHAPTER

5

Transmitter Leakage Canceller

5.1 Circuit Implementation

In this chapter, a TX leakage canceller (TXLC) circuit that is simple and has low NF contribution is proposed. A simplified block diagram of the proposed TXLC integrated with a LNA is shown in Figure 5.1. The TXLC is a feed-forward canceller, in which the TX reference signal is sampled using a coupler and is injected at the output of the LNA to suppress the leakage signal through the duplexer. To achieve the required rejection of the TX leakage signal, the TXLC needs to adjust the amplitude and phase of the reference signal in such a way that the reference and leakage signals have matching amplitude and 180° phase difference as illustrated in Figure 5.2. The amplitude and phase alignment functions can be achieved using an in-phase and quadrature-phase (IQ) generator and a

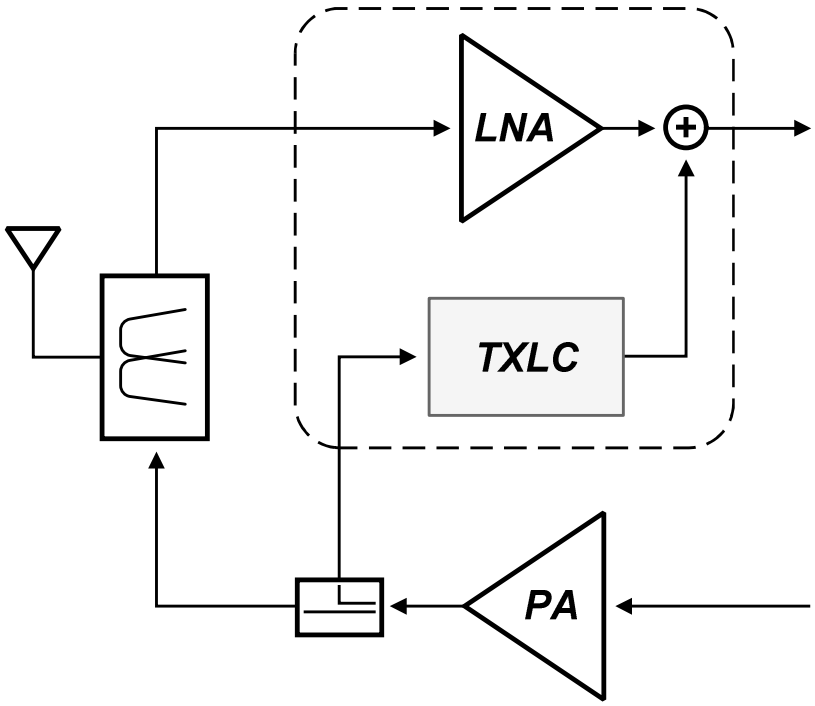

Figure 5.1. TXLC integrated with LNA.

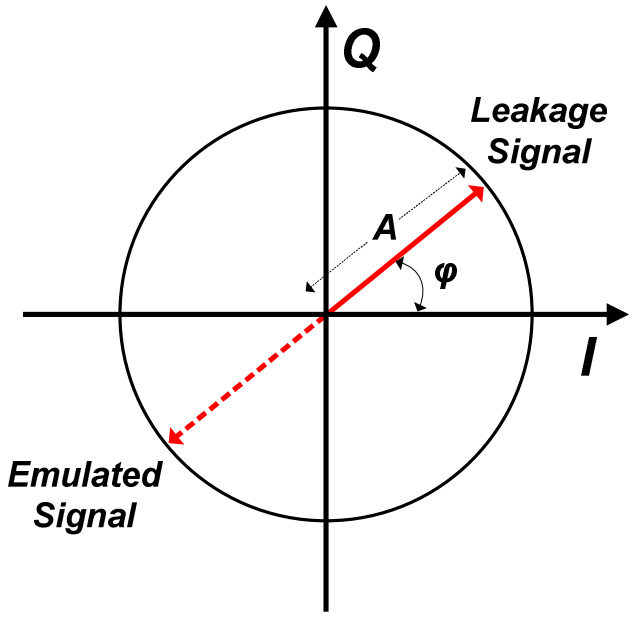

Figure 5.2. Amplitude and phase adjustment of the TX emulated signal.

pair of VGAs as shown in Figure 5.3. For a sinusoidal input (e.g., $X(t) = sin(2\pi ft)$), the transfer function of the TXLC is expressed as:

$$Y(t) = A_1 sin(2\pi ft) + A_2 cos(2\pi ft), \tag{5.1}$$

where f is the frequency of the input signal and A_1 and A_2 are the gains of VGA_1 and VGA_2, respectively. By appropriately varying A_1 and A_2 between -1 to 1, an amplitude adjustment and a full 360° phase tuning of the output signal can be performed. For gain control from -1 to 1 in the IQ paths of the TXLC, the same VGAs used in the FFE (e.g., see Figure 3.9) for applying tap coefficients are employed. The open-drain output nodes of the two VGAs are connected together to perform the summation of the IQ components in current mode.

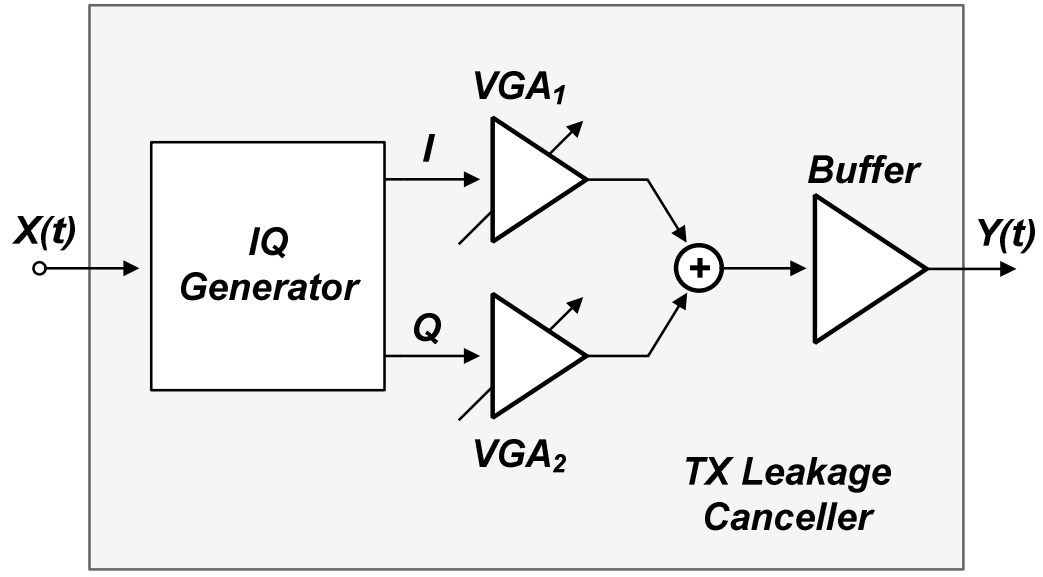

Figure 5.3. Implementation of TXLC.

For quadrature generation, a single-stage poly-phase filter (PPF), shown in Figure 5.4, is employed. The differential output voltage of a PPF at I and Q nodes are

$$V_{OUT\_I} = \frac{Z_L}{R + Z_L + sRCZ_L}(1 - sRC) \cdot V_{IN} \tag{5.2}$$

and

$$V_{OUT\_Q} = \frac{sRCZ_L}{R + Z_L + sRCZ_L}(1 + sRC) \cdot V_{IN}, \tag{5.3}$$

respectively [32]. In (5.2) and (5.3), Z_L is the load impedance of the output nodes and V_{IN} is the differential input voltage. From the two equations, the ratio between the I and Q output signals can be obtained as

$$\frac{V_{OUT\_I}}{V_{OUT\_Q}} = \frac{1 - sRC}{1 + sRC}. \tag{5.4}$$

According to (5.4), the output signals have the same amplitude for all R and C values and all frequencies, but the phase is exactly 90° only at a frequency equal to $1/RC$. Therefore,

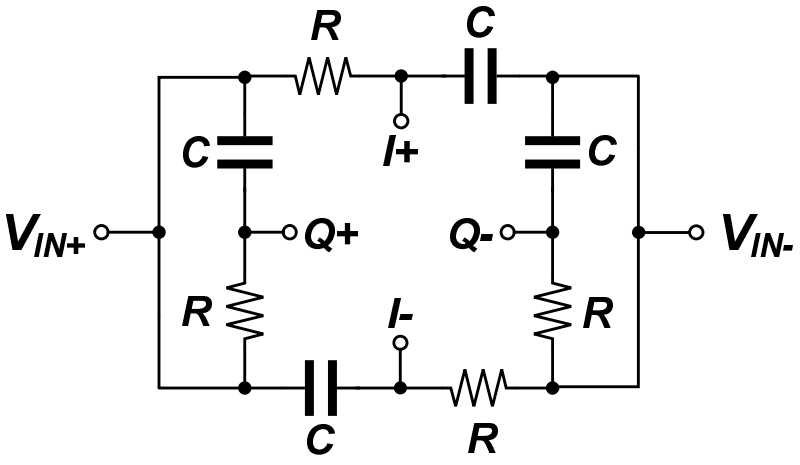

Figure 5.4. Schematic of single-stage PPF.

a PPF usually consists of two or more stages for precise generation of quadrature signals [33]. In this application, however, an exact 90° phase difference between the IQ paths is not necessary for the proper operation of the TXLC because the phase control over the entire 360° is still achieved even with a slight quadrature phase mismatch; therefore, a PPF with only one stage proved to be sufficient.

The TXLC also includes a buffer to inject the cancellation signal at the LNA output as shown in Figure 5.5. To be more specific, the injection is made at the low impedance source nodes of the common-gate devices, M_3 and M_4, of the LNA. The buffer is implemented with a simple open-drain differential pair to perform the injection and cancellation in the current domain. The LNA circuit is also shown in Figure 5.5. An inductively degenerated common-source topology is chosen for its low noise figure (NF) characteristic [34]. Furthermore, a cascode structure is employed to increase the isolation between the input and output ports and to provide a low impedance node for cancellation injection. The LNA input matching is provided by the off-chip gate inductors, L_{G1} and L_{G2}, along with the on-chip degeneration inductors, L_{S1} and L_{S2}. A symmetric inductor and load capacitors at the LNA output nodes are tuned to provide the maximum voltage gain at 2.14 GHz. Each output nodes are followed by an output buffer for 50Ω matching with measurement equipments. The layout of the proposed TXLC integrated with the LNA is shown in Figure 5.6.

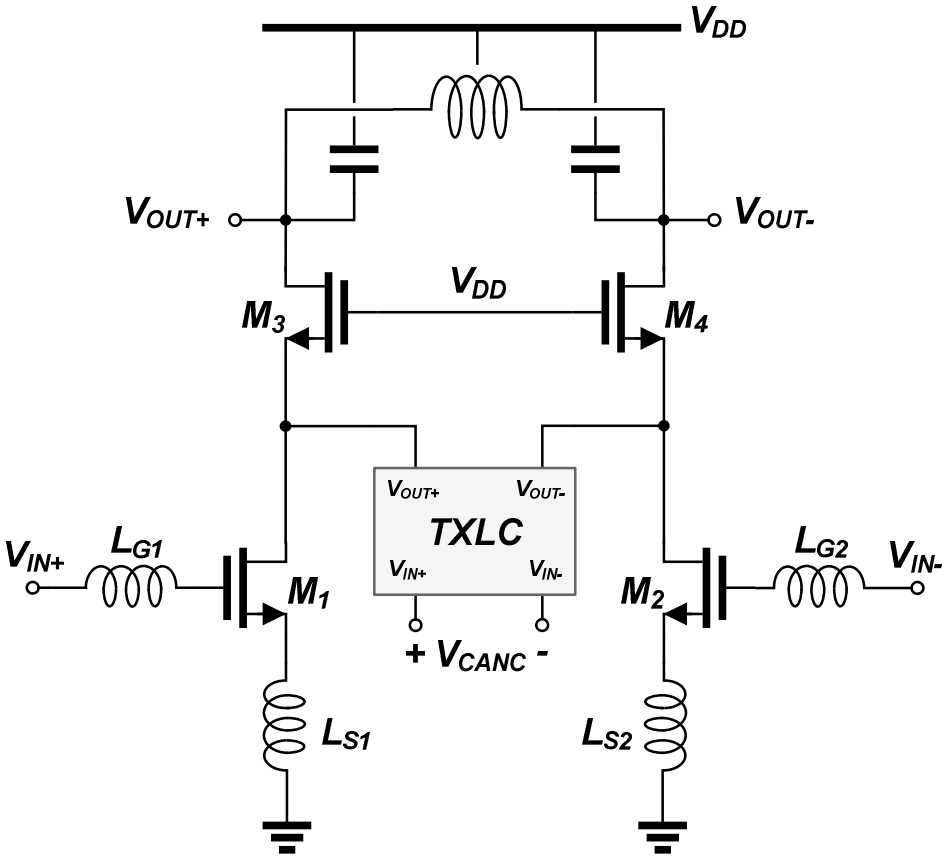

Figure 5.5. Schematic of LNA and the injection point of TXLC.

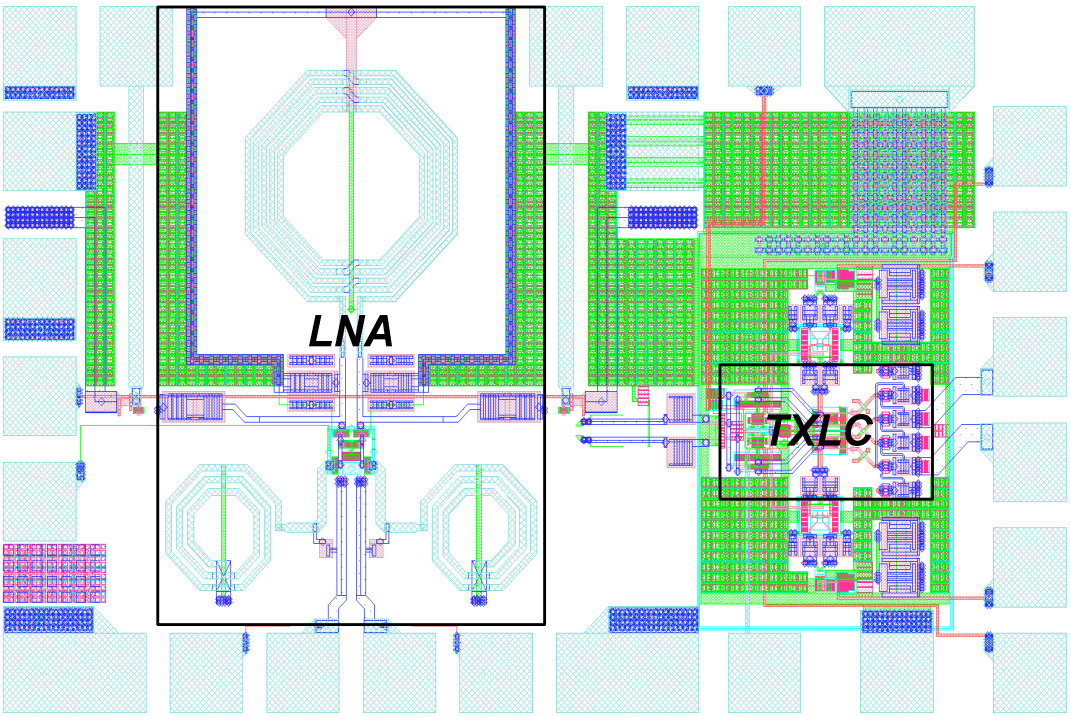

Figure 5.6. Layout of the proposed TXLC integrated with LNA.

5.2 Simulation Results

In this section, various simulation results of the TXLC are presented and summarized. As shown in Figure 5.7, the TXLC can be tuned to create a notch response at the LNA output. The notch responses can be obtained anywhere in the WCDMA TX frequency band (e.g., 1.92 to 1.98 GHz). It is evident that the resultant notches are very narrow-band in nature; however, within the 5 MHz WCDMA channel, the TXLC is able to provide average leakage rejection of around 20 dB, an amount that is sufficient to reduce XMD and IMD_2 in the RX path. Figure 5.8 presents the simulated transient response at

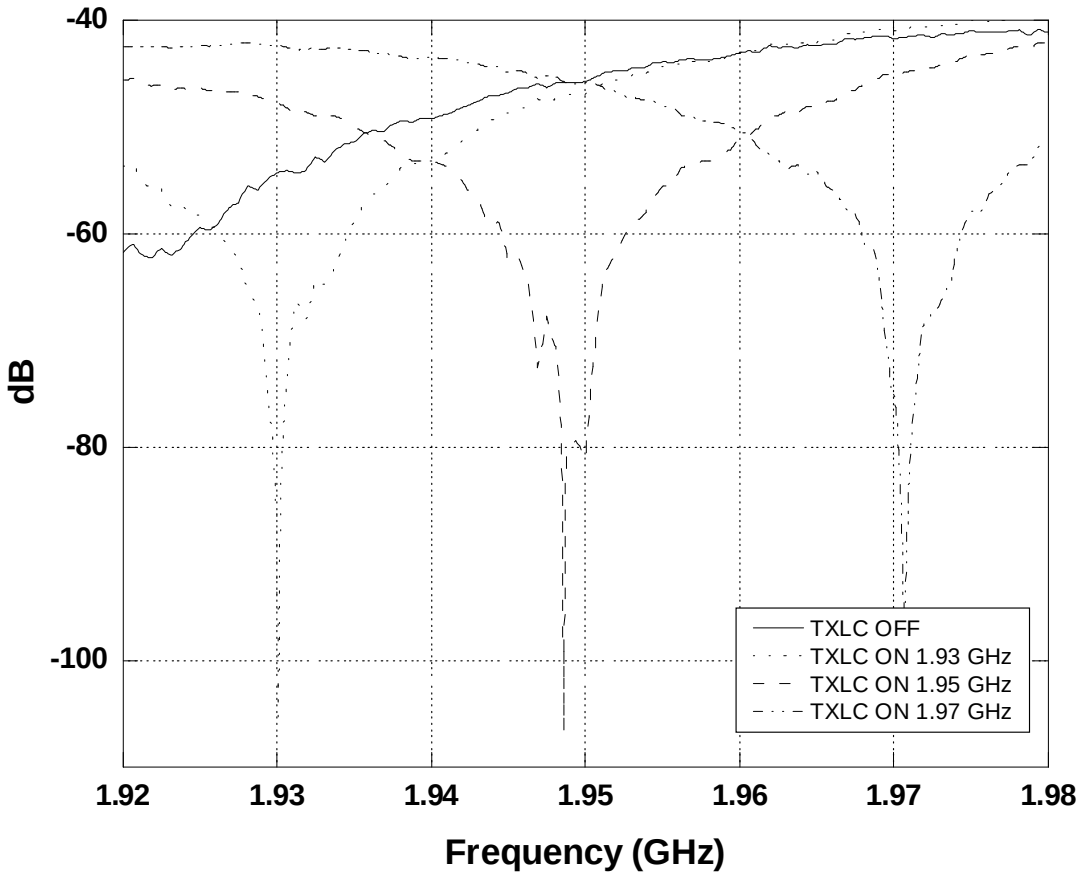

Figure 5.7. Simulated frequency response at LNA output for three different TXLC settings, creating notch at different TX frequencies.

the LNA output with the TXLC periodically turned on and off. The output waveform is obtained with 1.95 GHz RF carrier and 3.85 Mcps WCDMA uplink signal used as the TX leakage signal. The TX leakage rejection of around 20 dB can be observed from the LNA transient waveform.

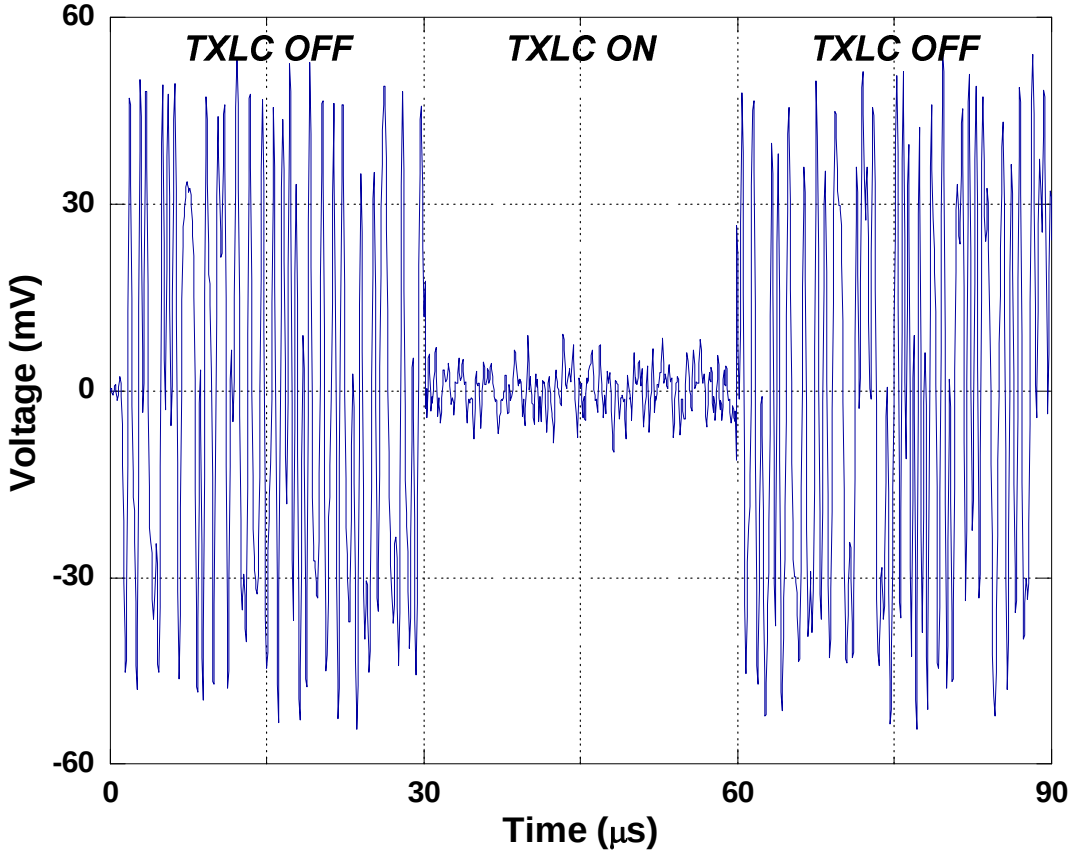

Figure 5.8. Simulated transient response at LNA output with 1.95-GHz RF carrier and 3.85-Mcps WCDMA uplink signal.

Lastly, the simulated LNA input return loss and gain are presented in Figure 5.9 (a) and (b), respectively. The LNA input return loss remains less than -20 dB over the entire WCDMA RX frequency band (e.g., 2.11 to 2.17 GHz), and the pass-band gain is around 26.5 dB; and these two values are not affected by the TXLC. The simulated LNA NF for TXLC off and on is presented in Figure 5.10; NF only degrades by around 0.3 dB, increasing from 0.93 dB to 1.21 dB, when the TXLC is enabled.

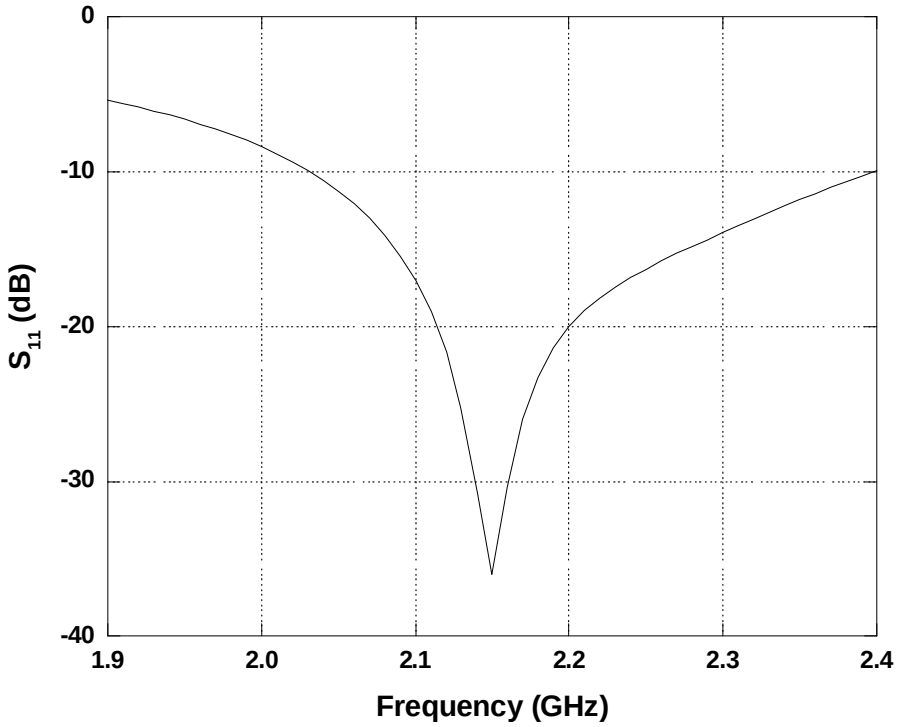

(a)

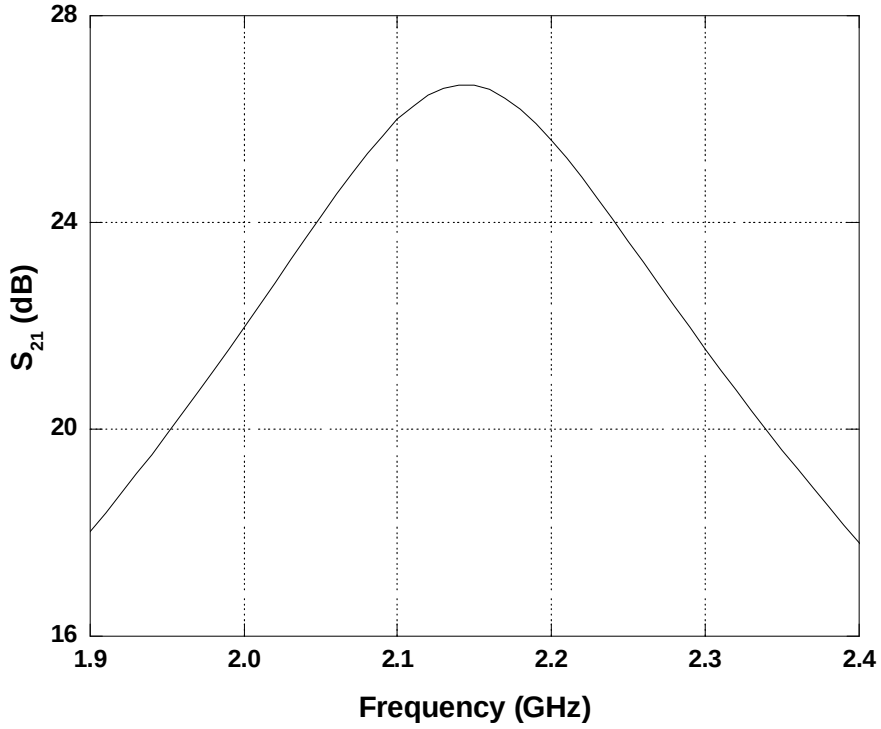

(b)

Figure 5.9. Simulation result of LNA (a) S_{11} and (b) S_{21}.

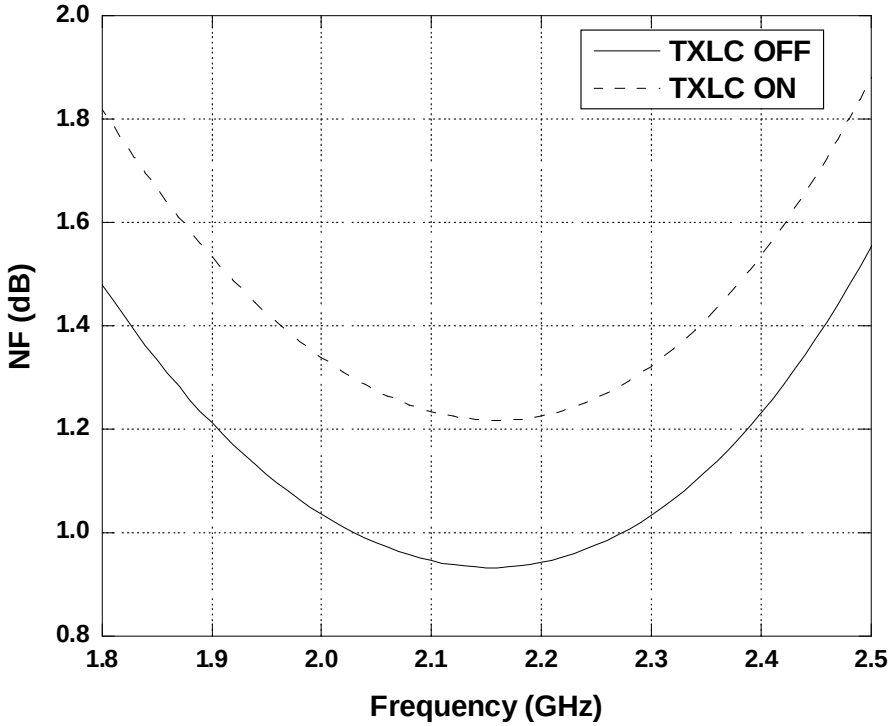

Figure 5.10. Simulated NF of LNA with TXLC off and on.

5.3 Measurement Results

To test the feasibility of TXLC integrated with LNA, the circuit is fabricated in a 0.18 μm CMOS technology. Shown in Figure 5.11 is a die photo of the TXLC, which measures 1.00 × 0.67 mm^2 including the bonding pads. The common-source LNA is on the left side, and the TXLC block is on the right side. The fabricated IC was mounted on a printed circuit board (PCB) as shown in Figure 5.12 for measurement purpose. A modified version of the TXLC that consists only of an IQ generator and two VGAs (e.g., without the summation node at the outputs of two VGAs) was also fabricated in a 0.18 μm CMOS technology to verify the performance of the IQ generator and VGAs. For an

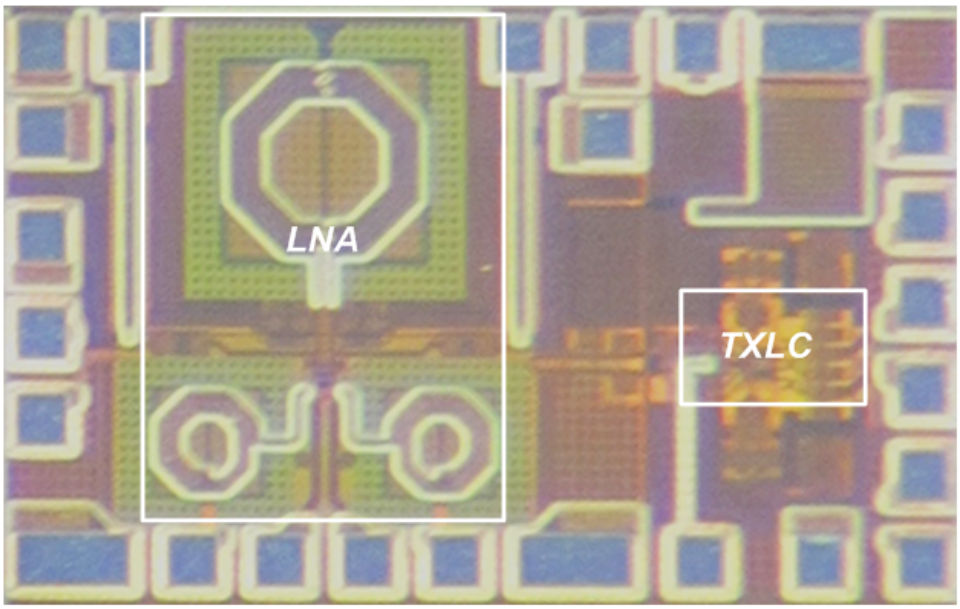

Figure 5.11. Microphotograph of the proposed TXLC integrated with LNA.

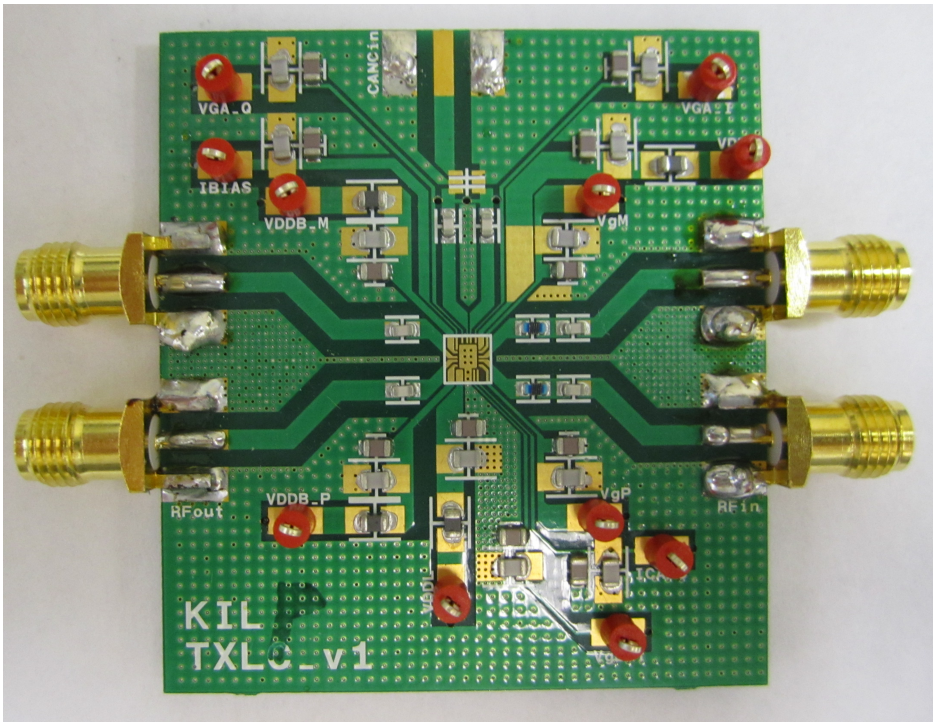

Figure 5.12. TXLC IC mounted on a PCB for measurement.

input sinusoidal signal with 2 GHz frequency, the outputs at the I-node and Q-node are measured using an oscilloscope. Figure 5.13 is a screen capture of the oscilloscope which shows the IQ amplitude imbalance of around 3% (i.e., 61.2 mV and 63.6 mV peak-to-peak voltage swings) and phase of around 90.2°. Gain measurement of the two VGAs was also conducted using a spectrum analyzer at 2 GHz; both of the VGAs demonstrated similar variable gain range from 0 to -30 dB for control voltage from 0 to 1 V as shown in Figure 5.14.

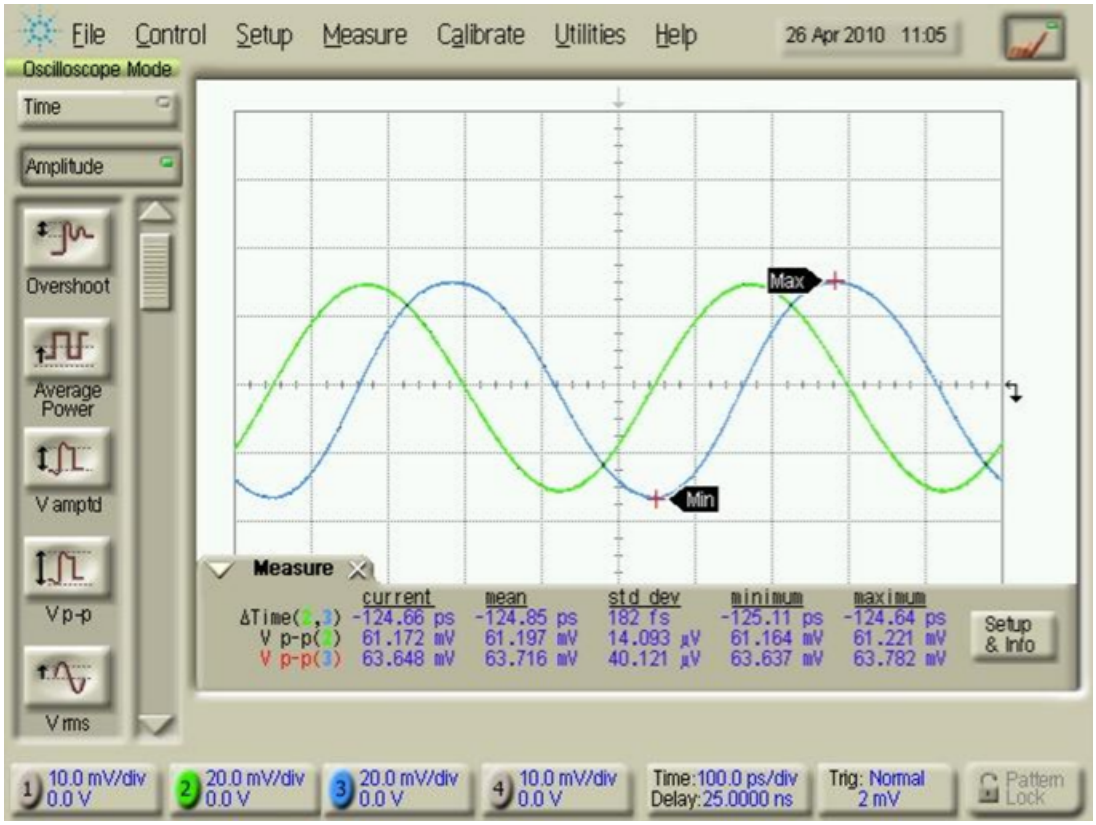

Figure 5.13. Oscilloscope measurement of I and Q outputs of TXLC circuit.

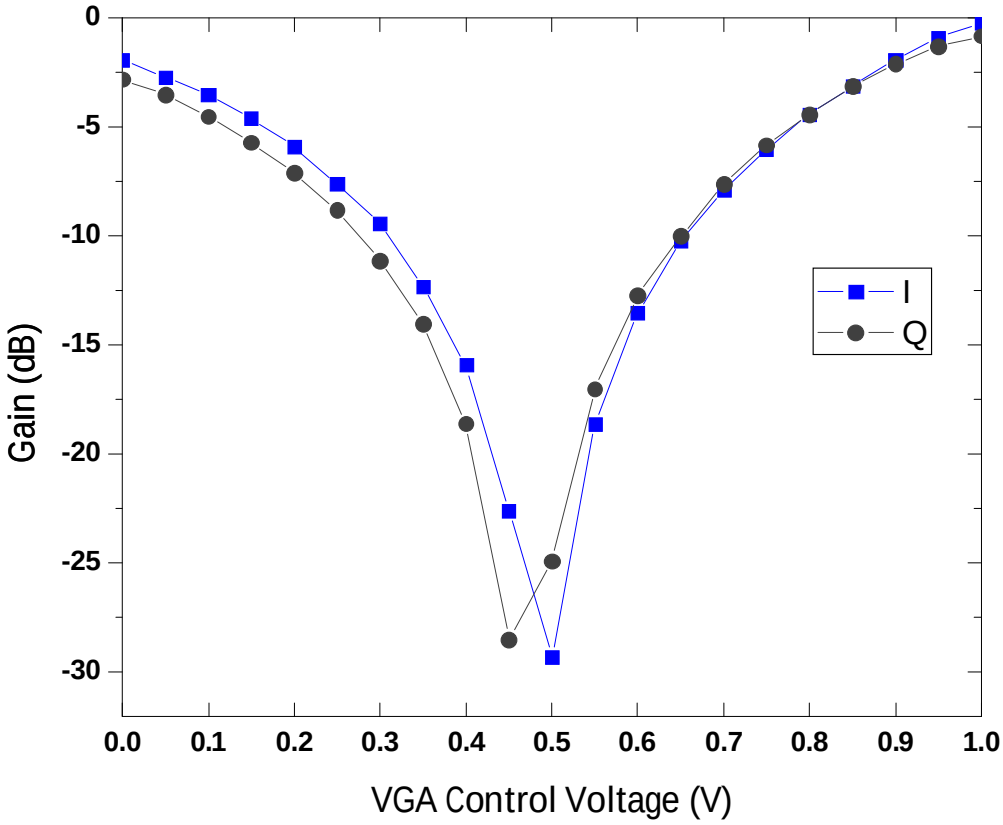

Figure 5.14. Gain versus control voltage of VGAs in I and Q paths.

Next, the performance of the WCDMA LNA is measured using the TXLC+LNA chip mounted on a PCB with all the necessary surface mount devices (SMDs) which include bypass capacitors, DC-blocking capacitors, and input-matching inductors for the LNA. The input return loss and gain of the LNA are measured using a vector network analyzer (VNA), and their plots are presented in Figure 5.15 and Figure 5.16, respectively. The measured input return loss of the LNA is less than -10 dB throughout all WCDMA RX frequency band (i.e., 2.11 GHz to 2.17 GHz). The pass-band gain is around 25.4 dB which is around 1 dB less than that from the simulation result. The measured IIP3 of -7.2 dBm is shown in Figure 5.17.

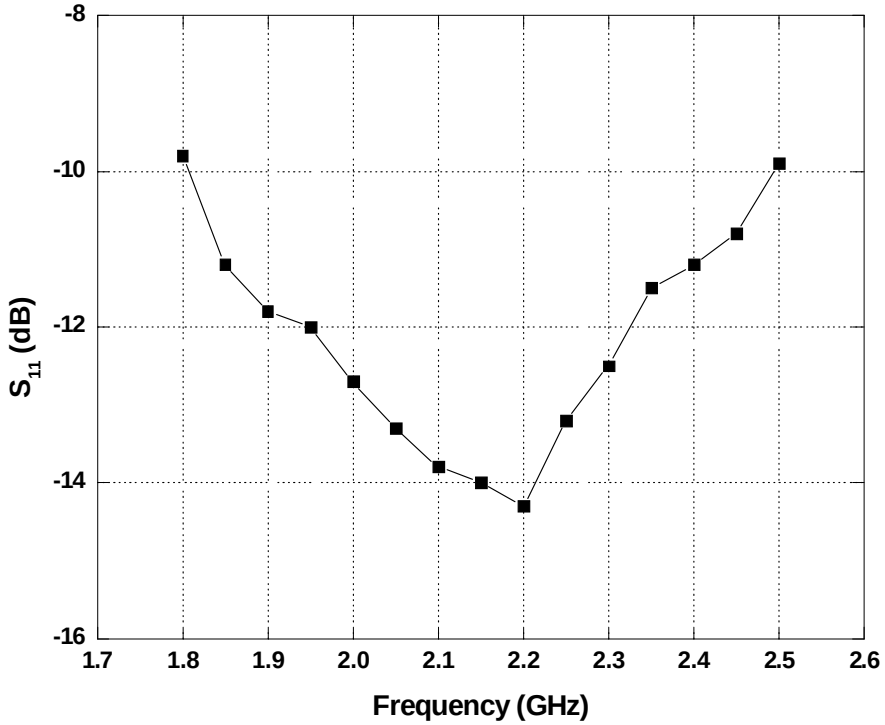

Figure 5.15. Measured input return loss of LNA.

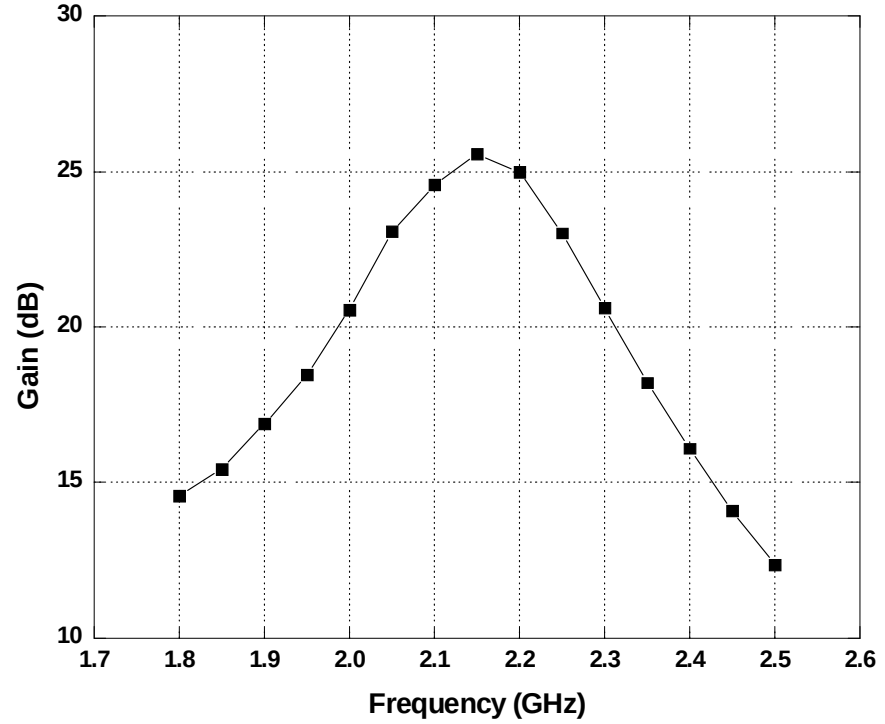

Figure 5.16. Measured gain of LNA.

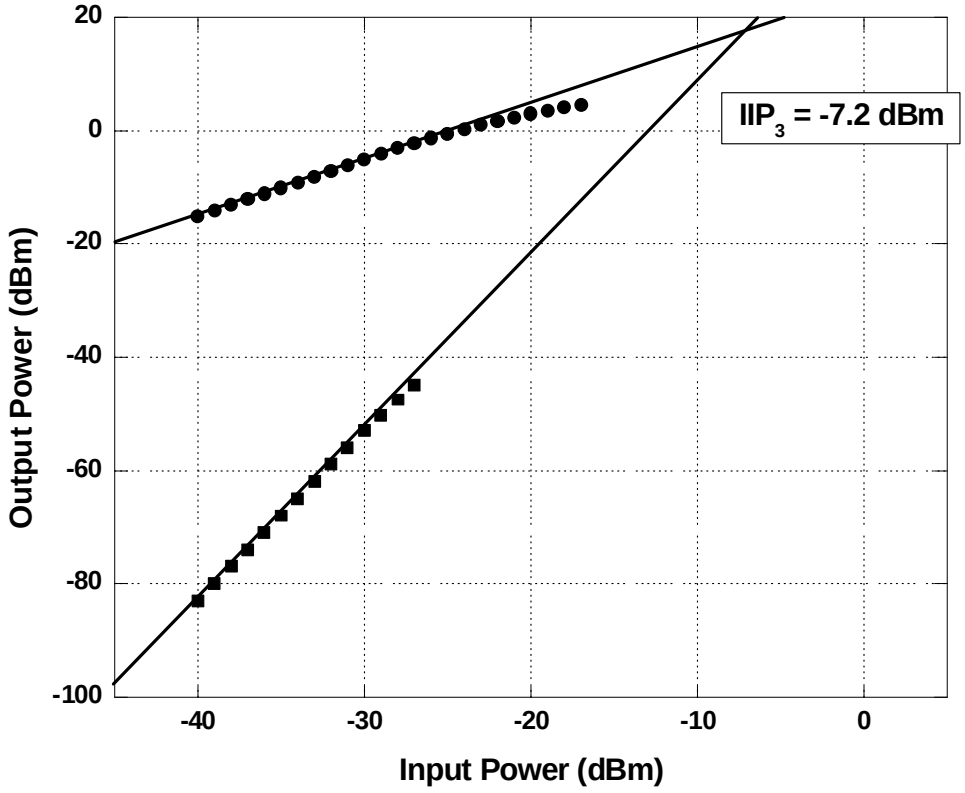

Figure 5.17. Measured IIP3 of LNA.

As shown in Figure 5. 18, the NF of the LNA is also measured with TXLC disabled and enabled. As expected, the minimum NF increases from 2.4 dB to 2.84 dB after TXLC is turned on. This increase in LNA minimum NF by 0.44 dB is slightly greater than 0.27 dB increase obtained from simulation.

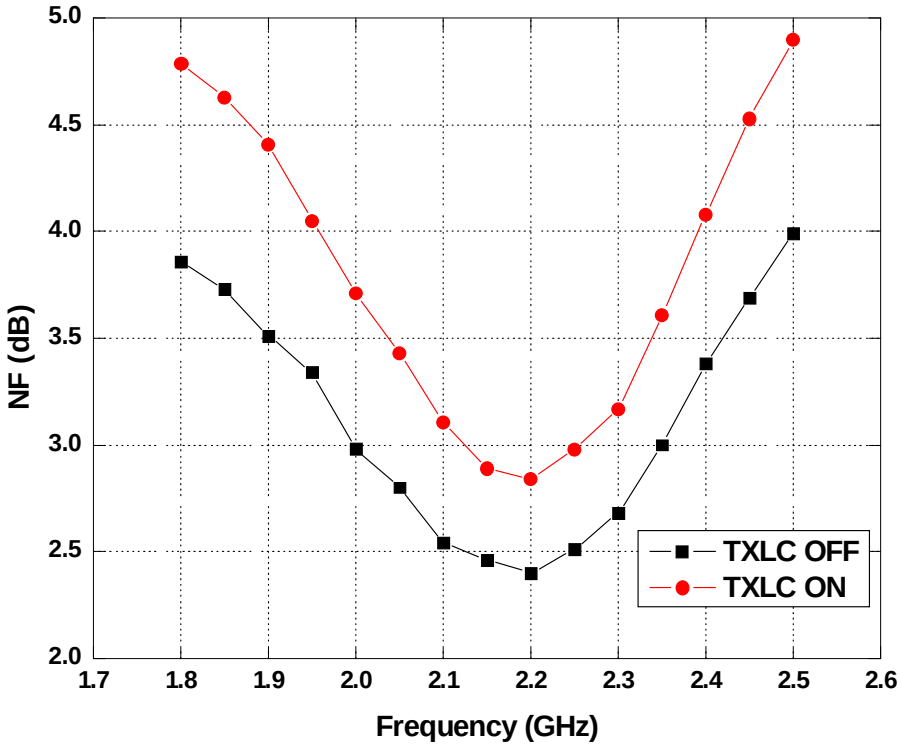

Figure 5.18. Measured NF of LNA with TXLC off and on.

After measuring the LNA performance, the TXLC leakage rejection was measured using the setup shown in Figure 5.19. At the input and output of the LNA, external phase-balanced baluns are employed. A SAW duplexer was also mounted on a PCB as shown in the measurement setup figure, and the duplexer is placed between the LNA input balun and 30 dB coupler. A vector signal generator is used for generation of WCDMA signal needed for the measurement. The output is monitored using a spectrum analyzer.

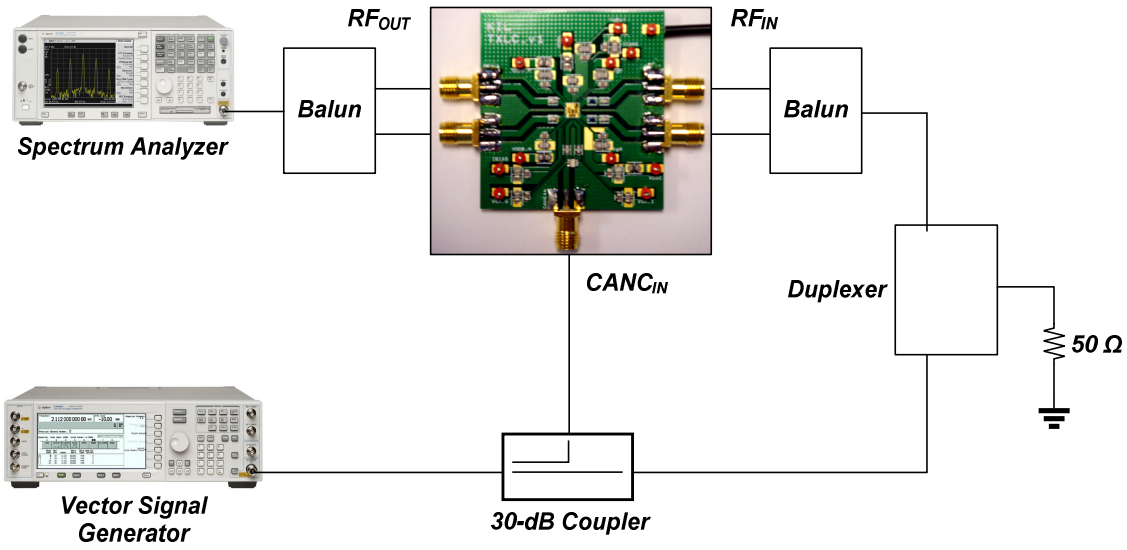

Figure 5.19. Measurement setup for testing TXLC leakage rejection performance.

First, the WCDMA envelope with TXLC turned off and on is measured as shown in Figure 5.20 (a) and (b), respectively. Channel frequency is centered at 1.95 GHz, and the average TX leakage power in the RX chain drops from -40.06 dBm to -70.82 dBm when TXLC is enabled. Next, the leakage WCDMA signal in the 5 MHz channel bandwidth for TXLC turned off and on is measured as presented in Figure 5.21 (a) and (b), respectively. In the channel bandwidth, 24.88 dB of leakage suppression is achieved by enabling TXLC (i.e., -24.10 dBm / 5 MHz to -48.98 dBm / 5 MHz). Figure 5.22 is a screen capture of WCDMA leakage spectrum on the spectrum analyzer, and the figure clearly shows the suppression of the leakage WCDMA spectrum when TXLC is turned on. Throughout the entire WCDMA TX frequency band (i.e. 1.92 GHz to 1.98 GHz), a minimum rejection of 22.5 dB is obtained from TXLC as shown in Figure 5.23.

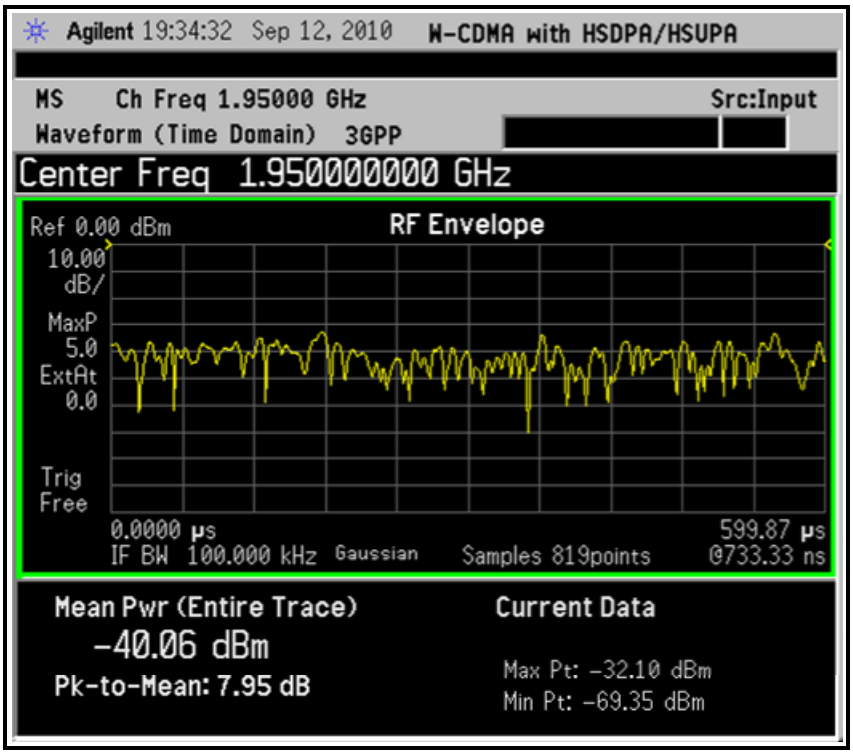

(a)

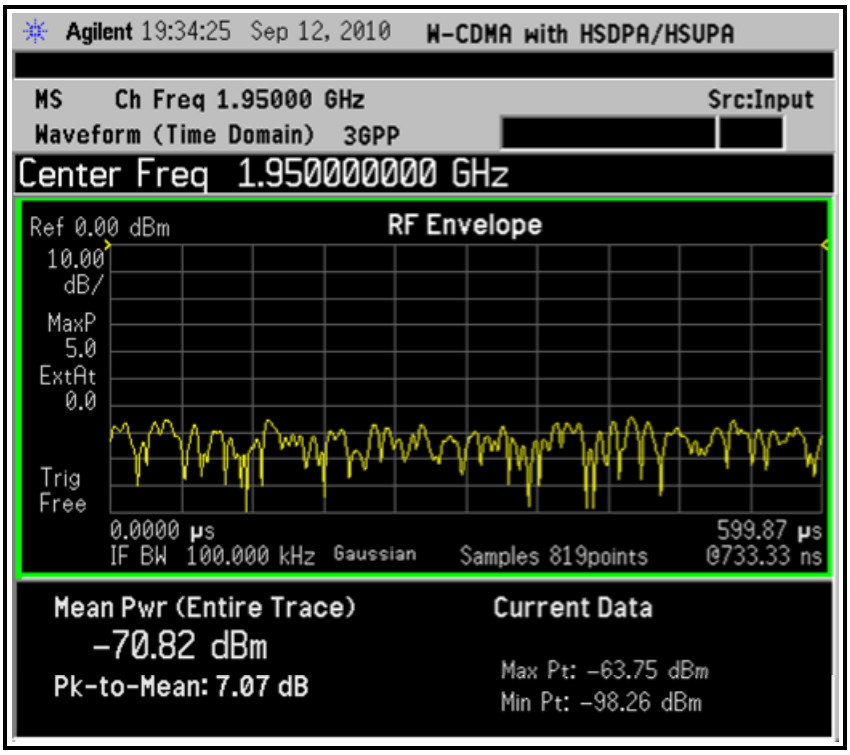

(b)

Figure 5.20. Measured WCDMA envelope with TXLC turned (a) off and (b) on.

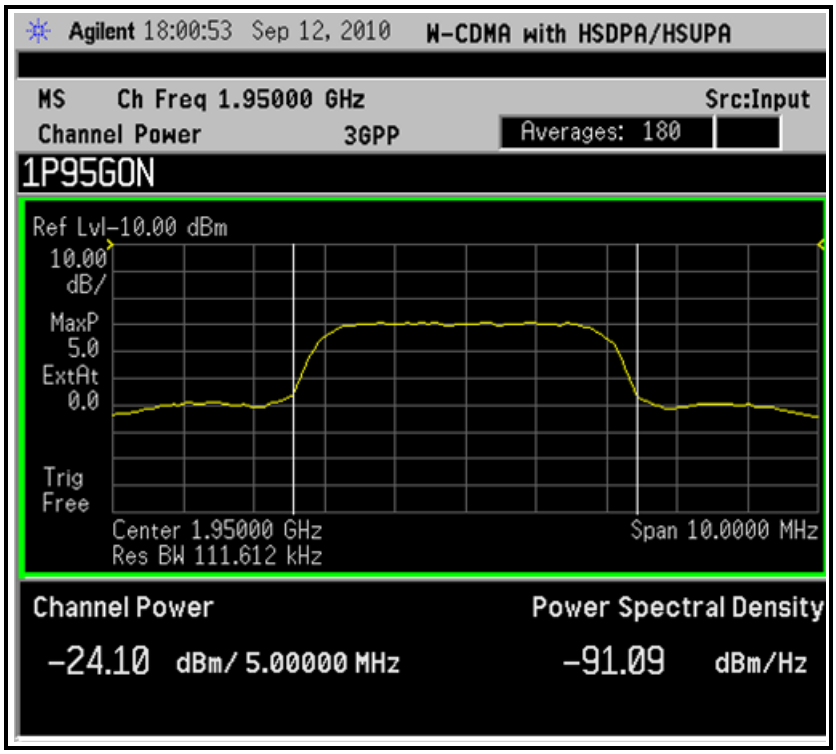

(a)

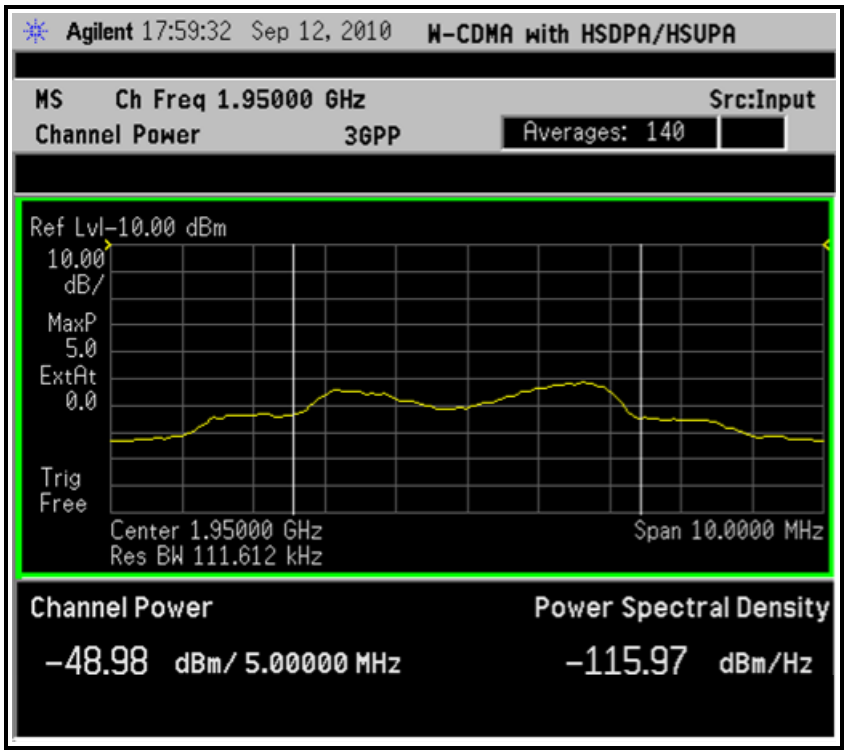

(b)

Figure 5.21. Measured WCDMA channel power with TXLC turned (a) off and (b) on.

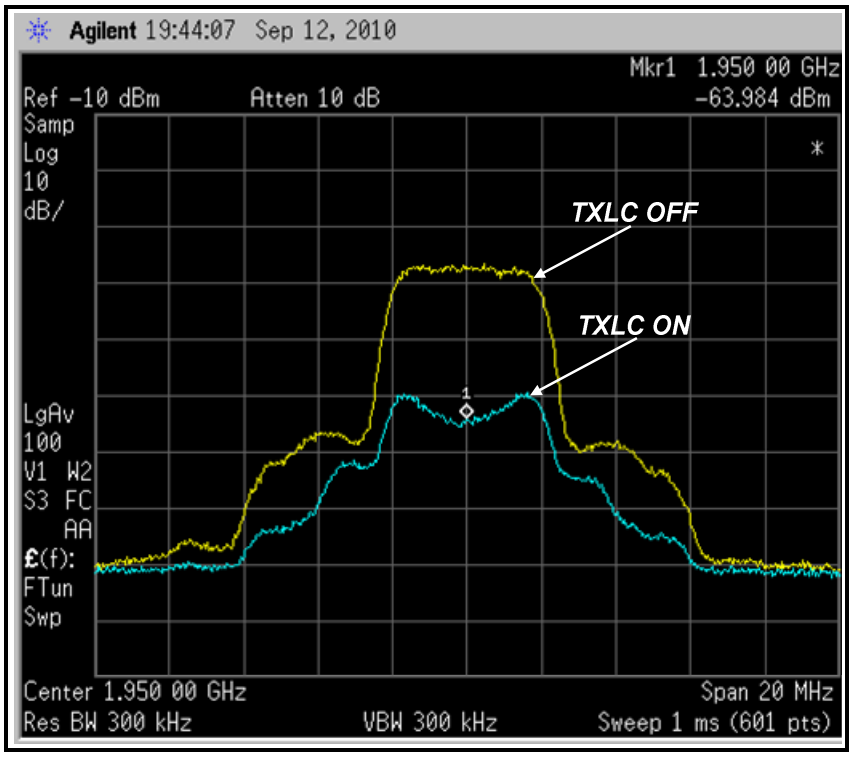

Figure 5.22. Measured WCDMA spectrum leakage at LNA output.

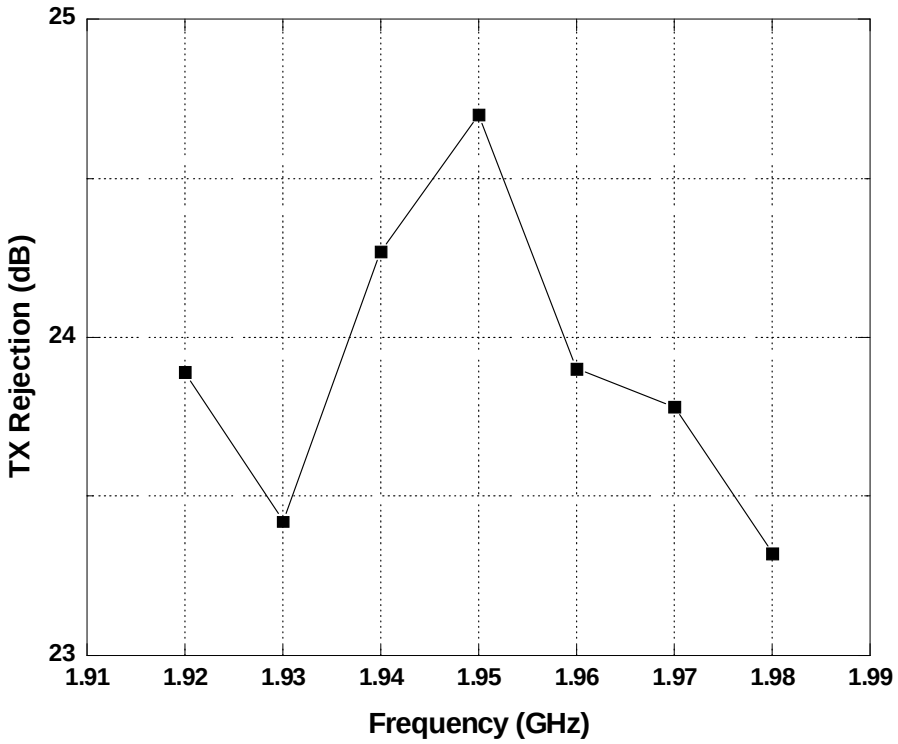

Figure 5.23. Measured TX leakage rejection ratio for different TX center frequency.

A summary of the measured performance of the LNA with TXLC is shown in Table 5.1. The proposed leakage canceller achieves a minimum rejection of 23.3 dB while consuming 19.6 mA from a 1.8 V supply when TXLC is enabled. In Table 5.2, the measured result of this work is compared with previously-reported works. The minimum NF of this design when the canceller is enabled is the lowest, and TXLC does not degrade the gain of the LNA unlike the other designs.

Table 5.1. Summary of Measured LNA/TXLC Performance

	TXLC Off	TXLC On
Gain	25.4 dB	25.4 dB
S_{11}	< -10 dB	< -10 dB
NF	2.4 dB	2.84 dB
TX Leakage Rejection	-	23.3 dB
Current	9.1 mA	19.6 mA
Technology	180 nm CMOS	
Chip Size	0.67 mm^2	

Table 5.2. Performance Comparison

	Gain Reduction	NF (Canceller ON)	Current Consumption Increase	Technology	Cancellation
Ayazian [30]	n/a	n/a	n/a	Discrete Components	23.5 dB
Safarian [31]	0.3 dB	4.1 dB	11 mA	180 nm CMOS	22.8 dB
Darabi [29]	2.5 dB	6.8 dB	21 mA	65 nm CMOS	21.0 dB
This Work	0 dB	2.84 dB	10.5 mA	180 nm CMOS	23.3 dB

CHAPTER

6

Conclusions

6.1 Summary

This work has examined signal integrity degradation factors and developed circuits that can enhance signal integrity for both optical and wireless communication systems. This thesis began with a study of different optical dispersion mechanisms that degrade signal integrity in optical networks. An optical coherent system employing FFEs is proposed to compensate for the performance-limiting effects of fiber dispersion and, therefore, to extend the transmission distance of the long-haul optical networks. The equalization circuit is designed and implemented in a 0.18 μm CMOS technology, and the measurement of the FFE demonstrated the capability to extend the transmission reach of long-haul optical systems over SMF to 600 km.

This dissertation then examines the signal integrity problems faced by the wireless communication systems. Specifically, a full-duplex wireless system experiencing interference from its own transmitter leakage signal is investigated. A transmitter leakage cancellation circuit that is simple in implementation and has low NF contribution is proposed and designed in a 0.18 μm CMOS technology in this work. The proposed cancellation circuit is integrated with a low-noise amplifier for WCDMA applications and demonstrates over 20 dB of transmitter leakage signal suppression.

6.2 Future Work

This work has studied signal integrity issues in both optical and wireless systems. One of the important results of this work in the optical domain is that a 9-tap FFE for 10 Gbps throughput was implemented in a 0.18 μm CMOS technology. For future works, FFEs targeted for data rates of 40 Gbps or higher can be studied and implemented using smaller process nodes. Moreover, integration of fully-closed adaptation loop that compares the input and the output and controls the tap coefficients of the FFE can also be included. Finally, the implementation of a fully integrated optical coherent system front-end with FFEs can be a good future work.

In the transmitter leakage cancellation work, the addition of an adaptation loop can also be considered as a future work; a power detector can sample the transmitter leakage signal at the output of LNA and feed it back to the control voltage of the TXLC. Furthermore, a full integration of a power amplifier, LNA, and transmitter leakage cancellation circuit can be an interesting topic for future study as well. Lastly, a special

attention can also be paid at reducing the power consumption of the TXLC. By studying different power saving techniques and successfully applying them to the TXLC can make the cancellation circuit more attractive and feasible.

REFERENCES

[1] G. P. Agrawal, *Fiber-Optic Communication Systems*. New York, NY: John Wiley and Sons, 2002.

[2] 802.3-2005 IEEE Standard for Information Technology - Telecommunications and Information Exchange between Systems - Local and Metropolitan Area Networks.

[3] B. Razavi, *Design of Integrated Circuits for Optical Communications*. New York, NY: McGraw-Hill, 2003.

[4] M. Onishi, *et al.*, "Dispersion compensation fiber with a high figure of merit of 250 ps/nm/dB," *Electron. Lett.*, vol. 30, no. 2, pp. 161-163, Jan. 1994.

[5] F. Ouellette, *et al.*, "All-fiber devices for chromatic dispersion compensation based on chirped distributed resonant coupling," *J. Lightwave Technol.*, vol. 12, pp. 1728-1738, Oct. 1994.

[6] D. A. Watley, *et al.*, "Compensation of polarization-mode dispersion exceeding one bit period using single high-birefringence fiber," *Electron. Lett.*, vol. 35, pp. 1094-1095, 1999.

[7] K. M. Patel and S. E. Ralph, "Multimode fiber link equalization by mode filtering via a multisegment photodetector," *IEEE 2003 International Microwave Symposium.*

[8] L. Raddatz, *et al.*, "Increasing the bandwidth-distance product of multimode fibre using offset launch," *Electon. Lett.*, vol. 33, 1997.

[9] K. Yonenaga and S. Kuwano, “Dispersion-tolerant optical transmission system using duobinary transmitter and binary receiver,” *J. Lightwave Technol.*, vol. 15, pp. 1530-1537, Aug. 1997.

[10] E. Forestieri and G. Prati, "Narrow filtered DPSK implements order-1 CAPS optical line coding," *IEEE Photonics Tech. Lett.*, vol. 16, pp. 662- 664, Feb. 2004.

[11] J. H. Winters, “Equalization in coherent lightwave systems using a fractionally spaced equalizer,” *J. Lightwave Technol.*, vol. 8, pp. 1487-1491, Oct. 1990.

[12] J. R. Barry, E. Lee, D. G., Messerschmitt, *Digital Communication.* Norwell, Massachusetts: Kluwer Academic Publishers Group, 2004.

[13] S. Chandramouli, *et al.*, “10-Gb/s optical fiber transmission using a fully analog electronic dispersion compensator (EDC) with unclocked decision-feedback equalization,” *2007 IEEE Trans. Microwave Theory Tech.*, vol. 55, no. 12, pp. 2740-2746, Dec. 2007.

[14] Y. Yamamoto and T. Kimura, “Coherent optical fiber transmission systems,” *IEEE J. Quantum Electron.*, vol. 17, pp. 919-935, Jun. 1981.

[15] T. Ono, *et al.*, “Demonstration of high-dispersion tolerance of 20-Gbit/s optical duobinary signal generated by a low-pass filtering method,” in *Proc. OFC’97,* Dallas, TX, Feb. 1997, paper ThH1.

[16] D. Penninckx, *et al.*, “The phase-shaped binary transmission (PSBT): A new technique to transmit far beyond the chromatic dispersion limit,” in *22nd Eur. Conf. Optical Communication – ECOC’96*, Oslo, Norway, 1996, paper TuD.2.3.

[17] J. H. Winters, *et al.*, “Reducing the effects of transmission impairments in digital fiber optic systems,” *IEEE Commun. Mag.*,vol. 31, pp. 68-76, June 1993.

[18] M. Seimetz, “Phase diversity receivers for homodyne detection of optical DQPSK signals,” *J. Lightwave Technol.*, vol. 24, pp. 3384-3391, Sep. 2006.

[19] T. G. Hodgkinson, *et al.*, “In-phase and quadrature detection using 90° optical hybrid receiver: experiments and design considerations,” *IEE Proc. Optoelectronics*, vol. 135, pp. 260-267, Jun. 1988.

[20] K.H. Lee, *et al.*, "A 10 Gb/s coherent detection system with feed-forward equalizers for optical duobinary transmission," in *Microwave Integrated Circuits Conference, 2009. EuMIC 2009. IEEE European*, 2009, pp.286-289.

[21] M. Maeng, *et al.*, “0.18-um CMOS equalization techniques for 10-Gb/s fiber optical communication link,” *2005 IEEE Trans. Microwave Theory Tech.*, vol. 53, no. 11, pp. 3509-3519, Nov. 2005.

[22] K.H. Lee, *et al.*, "Performance analysis of feed-forward equalizers based on passive and active delay cells for multi-Gb/s optical fiber links," in *Microwave Conference, 2008. APMC 2008. IEEE Asia-Pacific*, 2008, pp. 1-4.

[23] H. Song and C. Kim, “An MOS four-quadrant analog multiplier using simple two-input squaring circuits with source followers,” *IEEE J. Solid-State Circuits,* vol. 34, no. 5, pp. 592-598, May 1999.

[24] F. Bien, *et al.*, "A 10-Gb/sec Reconfigurable CMOS equalizer employing a transition detector based output monitoring technique for band-limited serial links," *IEEE Trans. Microwave Theory Techn.*, vol. 54, no. 12, pp. 4538-4547, Dec. 2006.

[25] B. Razavi, *RF Microelectronics*. Upper Saddle River, NJ: Prentice-Hall, 1998.

[26] *Universal Mobile Telecommunications System (UMTS) User Equipment (UE) Conformance Specification*, 3GPP Std. ETSI TS 134, October 2008.

[27] V. Aparin and L. E. Larson, "Analysis and reduction of cross-modulation distortion in CDMA receivers," *IEEE Trans. Microwave Theory Techn.*, vol. 51, no. 5, pp. 1591-1602, May 2003.

[28] Epcos SAW Components: Data Sheet 7835. [Online]. Available: http://www.epcos.com/inf/40/ds/mc/B7835.pdf

[29] H. Darabi, "A blocker filtering technique for SAW-less wireless receivers," *IEEE J. Solid-State Circuits,* vol. 42, no. 12, pp. 2766-2773, Dec. 2007.

[30] S. Ayazian and R. Gharpurey, "Feedforward interference cancellation in radio receiver front-ends," *IEEE Trans. Circuits Systems II,* vol. 54, no. 10, pp. 902-906, Oct. 2007.

[31] A. Safarian, *et al.*, "Integrated Blocker Filtering RF Front Ends," *Proc. IEEE Radio Frequency Integrated Circuits Symposium* 2007, pp. 13-16.

[32] J. Kaukovuori, *et al*., "Analysis and design of passive polyphase filters," *IEEE Trans. on Circuits and Systems I*, vol. 55, no. 10, pp. 3023-3037, Nov. 2008.

[33] S. Galal, *et al.*, "RC Sequence Asymmetric Polyphase Networks for RF Integrated Transceivers," *IEEE Trans. Circuits Systems II*, vol. 47, no. 1, pp. 18-27, Jan. 2000.

[34] D. K. Shaeffer and T. H. Lee, "A 1.5-V, 1.5-GHz CMOS low noise amplifier," *IEEE J. Solid-State Circuits*, vol. 32, no. 5, pp. 745-759, May 1997.

PUBLICATIONS

[1] **K.H. Lee**, D. Bhatta, H. Kim, E. Gebara, and J. Laskar, "A 10 Gb/s coherent detection system with feed-forward equalizers for optical duobinary transmission," in *Microwave Integrated Circuits Conference, 2009. EuMIC 2009. IEEE European*, 2009, pp.286-289.

[2] **K.H. Lee**, D. Bhatta, H. Kim, E. Gebara, and J. Laskar, "Performance analysis of feed-forward equalizers based on passive and active delay cells for multi-Gb/s optical fiber links," in *Microwave Conference, 2008. APMC 2008. IEEE Asia-Pacific*, 2008, pp. 1-4.

[3] **K.H. Lee**, D. Bhatta, E. Gebara, and J. Laskar, "A self-calibrating wideband CMOS IQ generator," in *Electronics Letters*, submitted.

[4] D. Bhatta, **K.H. Lee**, H. Kim, E. Gebara, and J. Laskar, "A 10Gb/s two dimensional scanning eye opening monitor in 0.18-um CMOS process," in *Microwave Symposium, 2009. IMS 2009. IEEE International, 2009*, pp. 1141-1144.

[5] H. Kim, D. Bhatta, **K.H. Lee**, C. Scholz, E. Gebara, and J. Laskar, "Performance analysis of balanced and unbalanced feed-forward equalizer structures for multi-gigabit applications in 0.18-um CMOS process," in *Microwave Integrated Circuits Conference, 2008. EuMIC 2008. IEEE European*, 2008, pp. 143-146.

[6] H. Kim, J. de Ginestous, F. Bien, **K.H. Lee**, S. Chandramouli, Y. Hur, C. Scholz, E. Gebara, and J. Laskar, "An electronic dispersion compensator (EDC) with an analog eye-opening monitor (EOM) for 1.25-Gb/s Gigabit Passive Optical Network (GPON) upstream links," in *Microwave Theory and Techniques, IEEE Transactions on*, vol. 55, pp. 2942-2950, 2007.

[7] J.J. Kim, J. Choi, **K.H. Lee**, F. Bien, K. Lim, and C.-H. Lee, “Wideband CMOS voltage-controlled oscillator using tunable inductors,” in *Electronics Letters*, vol. 46, no. 20, pp. 1391-1393, 2010.